

This file has been cleaned of potential threats.

To view the reconstructed contents, please SCROLL DOWN to next page.

مجلة المنوفية لبحوث الهندسة الإلكترونية

كلية الهندسة الإلكترونية - جامعة المنوفية



1&2-24

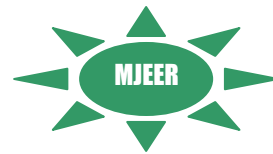
كلية الهندسة الإلكترونية - جامعة المنوفية
Faculty of Electronic Engineering - Minufiya University

المجلد الرابع والعشرون - العدد الأول والثاني يناير - يوليو 2015

Minufiya Journal of Electronic Engineering Research

Faculty of Electronic Engineering - Minufiya University

- **A Simulation Based Geometrical Analysis of MEMS Capacitive Pressure Sensors for High Absolute Pressure Measurement** 01
Ahmed Gafa*, Galal Atlam, and Imbaby I. Mahmoud
- **High Density Noise Removal in Endangered Silent-Films Using Non-linear Filters: A Comparative Study** 19
Hassan M. ElKamchouchi, Ahmed E. Khalil and Samy H. Darwish
- **Statistical Analysis of Alzheimer 's disease Images** 43
Mohamed M. Dessouky, Mohamed Elrashidy1, Taha E. Taha, and Hatem Abdelkader
- **Advanced Relay Station for LTE-A Downlink Physical Layer** 67
Mohamed G. El-Mashed and S. El-Rabaie
- **Memristor Overview up to 2015** 79
Sherif F. Nafea, Ahmed A.S. Dessouki and S. El-Rabaie
- **An Electrical Model for Atom's Emission and Future Electronics** 107
Ali A. Elabd, El-Sayed M. El-Rabaie, Abdel-Aziz T. Shalaby



24 – 1&2

كلية الهندسة الإلكترونية – جامعة المنوفية
Faculty of Electronic Engineering-Minufiya University

Vol. 24 - No. 1&2

January-July 2015

ISSN 1687-1189

رقم الإيداع: 52/2/2002

INFORMATION FOR AUTHORS

The Minufiya Journal of Electronic Engineering Research (MJEER) publishes only research papers. The journal does not publish essay or technical reporting types of paper. Prospective authors are encouraged to examine the journal itself for details of layout. Detailed instructions, which should be fully adhered at time of publication, are available upon request from the editor office. However submitted papers shall not be sent to referees before full adherence to the following requirements:

1. The submitted paper should not have been submitted earlier or at the same time to any other journal in Egypt or abroad.
2. Papers should be submitted in English in both of the following two form:
 - an original and three copies in A4 size
 - stored on a (CD) using WINWORD, Times New Roman, size 13
3. The margins in all pages except the first page are 3.5 cm from the top and the bottom, and 2.5 cm from the left and right. The first page should have margins 5 cm from the top. Text should be justified to the left and the right margins.
4. Only the abstract, the acknowledgments, the list of references, and the list of symbols are to be single line spaced. Other sections are to be 1.5 line spaced.
5. Paper title is to be typed centered in bold capital letters. Author(s) Name(s) should be typed in plain capital letters, centered, and placed 3 single spaces under the paper title. Footnote, size 10, giving the author(s) title(s) and affiliation(s) should be provided.
6. English abstract, maximum 200 words, should be provided immediately before the "Introduction" with the word ABSTRACT as heading flush left.
7. Figures and tables are to be totally integrated within the text. Captions should be located under the figure and on top of the table and clearly spaced within the main text. Lettering should be large enough to be readable after 80% reduction.
8. Reference should be cited in the text between square brackets and listed at the end of the paper with the word REFERENCES as heading flush left.
9. Headings are to be bold, flush left, with Arabic numerals. Major headings are all capital, subheading are initial capital, and only the first letter of each third level headings is capital.
10. Arabic summary within 10 lines is to be provided at the end of the paper preceded by Arabic translation of the paper title and abstract. For non-Arabic speaking authors a free of charge translation of the paper title and abstract can be provided by the editors.
11. For prospective authors a nonrefundable down payment of:
 - a) 225.0 LE for the regular paper of 8 pages and 10.0 LE for each extra page if they are faculty staff members,
 - b) 275.0 LE for the regular paper of 8 pages and 15.0 LE for each extra page if they are staff members in the university of Minufiya
 - c) 300.0 LE for the regular paper of 8 pages, and 20.0 LE for each extra page if they are members of other institution.
 - d) 100.0 USD for the regular paper of 8 pages, and 5.0 USD for each extra page if they are members of foreign institutions.

This amount is to be paid upon submission of the paper. In case of acceptance, the remaining fees should be settled with the treasurer before enrollment of the paper in the next possible issue. Publication fees cover cost of one copy of the journal, and 5 reprint.

Annual subscriptions : personal, 50.0 LE in Egypt and 50.0 USD abroad, institutional : 300.0 LE in Egypt and 300.0 USD abroad.

N.B. the ideas expressed in the papers are strictly those of the authors. The editors do not hold themselves responsible for the views expressed by the author

Minufiya Journal of Electronic Engineering Research (MJEER)

**Faculty of Electronic Engineering,
Minufiya University, Menouf, 32952, Egypt.**

Editorial Board:

Editor-in-Chief:

Prof. Dr. Mohamed A. El-Bardiny

Co-Editor:

Prof. Dr. Mohamed F. El-Kordy

Managing Editor:

Prof. Dr. El-Sayed M. El-Rabiee

Executive Editor:

Assoc. Prof. Gamal Mahrous ATTIYA

Scientific Advisory Committee:

Prof. Dr. Kamal H. Awad-Allah

Prof. Dr. Taha El-Sayed Taha

Prof. Dr. Magdy M. Kamel

Ass. Prof. Ayman El-Sayed

Ass. Prof. Ahmed E. Bahnasy

Ass. Prof. Mohamed El-Barawany

Ass. Prof. Fathy E. Abd Elsamea

Ass. Prof. Mohamed Hamdy

Administrative Secretary:

Mr. Yasser M. Hegazy

Mrs. Heba A. Mohammed

Mrs. Sabah M. Anbar

A Simulation Based Geometrical Analysis of MEMS Capacitive Pressure Sensors for High Absolute Pressure Measurement

Ahmed Gafar*, Galal Atlam*, and Imbaby I. Mahmoud**

* Faculty of Elect., Eng., Minufiya University, EGYPT.

** Atomic Energy Authority, EGYPT.

(Received: 01-April-2015 – Accepted: 03-May-2015)

Abstract

This paper presents the performance characteristics evaluation of MEMS capacitive pressure sensor. This type of absolute pressure measuring sensor is used for pulse rate measurement. Polysilicon material provides a higher sensitivity when chosen as diaphragm material. Two MEMS capacitive pressure sensors with varying geometries are analyzed in Matlab simulation software. The geometries are very common having parallel plates with spring loaded. In first stage the shape of the parallel plates is circular and in second case of the parallel plate is square. During modeling of these two different shaped sensors, the area of parallel plates in both cases is considered as equal. Once the geometries are formed, the electromechanical analyses have been performed. It is observed that these types of pressure sensors can withstand a wide range of absolute pressure from kilo Pascals to several order of mega Pascals. In this work, Matlab environment is employed to model this sensor and accurate model is devised to study its performance. Simulation results are obtained and compared with published work of FEM (Finite Element Method) based Multiphysics simulation platform and full argument is obtained. The proposed model allows handling different parameters affecting the performance of this sensor.

1. Introduction

The microfabricated pressure sensor is one of MEMS devices used in a wide range of applications. In MEMS technology, piezoresistive pressure sensors are very common. However, in the past years capacitive pressure sensors have received attention due to several advantages in comparison to piezoresistive pressure sensors. The main disadvantage of the piezoresistive pressure sensor is the inherent temperature dependence of piezoresistive coefficients [1]. Moreover, capacitive pressure sensor has lower power consumption than piezoresistive pressure sensor [2]. But piezoresistive pressure sensor most widely used than capacitive pressure sensor because of two reasons; capacitive structure is more complicated to fabricate and the capacitive sensing principle is sensitive to parasitic capacitances. The structure of the capacitive pressure sensor is more complicated, because it involves formation of a cavity that separates the two sensing electrodes from each other. Formation of such a cavity is done in two different ways. For first case multiple film depositions and etch of a buried sacrificial layer [3–6] or in second case bonding after the cavity has been etched into one of the wafer. Wafer bonding is done by fusion bonding of two silicon wafers or anodic bonding of a silicon wafer and a glass wafer [7–9]. Capacitive pressure sensors are required in applications including bio-medical systems, environmental monitoring and industrial process control. Capacitive pressure sensors provide low noise, high sensitivity, have low temperature sensitivity and are preferred in many emerging high performance applications and can withstand a lot of vibration. Micromachined capacitive pressure sensors have typically used an elastic diaphragm with springs and a sealed cavity in between the diaphragm and the substrate below. There is a pair of parallel plate which forms capacitor. Lower plate is fixed and upper plate acts as movable plate which is attach with spring and four boundaries are fixed. Pressure is applied on upper plate; it deforms which changes the distance between two plates due to this capacitance changes. The change of capacitance is used for measuring pressure [10, 11]. The design parameters of MEMS based diaphragm type capacitive pressure sensors using Matlab software is explored. Two different shaped diaphragms with the same area for sensing high absolute pressure are designed.

Mechanical, electromechanical as well as material studies are performed. The analyzed results are in the form of 2-D plots. The outcome of these designed sensors are discussed and compared against their efficiencies.

2. Methods and materials

A. Mathematical modeling:

The maximum stress for circular diaphragm is given by [12]:

$$\sigma_{max} = \frac{3\gamma W}{8\pi h^2} \quad (1)$$

The maximum deflection of the circular plate occurs at the centre position of the plate is given by [13]:

$$W_{max} = \frac{3w(m^2 - 1)a^2}{16\pi E m^2 h^3} \quad (2)$$

The maximum stress at the middle of each edge for square diaphragm is given by [12]:

$$\sigma_{max} = \frac{0.309Pa^2}{h^2} \quad (3)$$

The maximum deflection for square diaphragm is given by [14]:

$$W_{max} = \frac{0.0138Pa^4}{Eh^3} \quad (4)$$

Where:

W : is the total force acting on the plate,

h : is the diaphragm thickness,
 a : is the radius of the diaphragm,
 P : is the pressure difference across the diaphragm,
 E : is the Young's modulus of the diaphragm material,
 γ : is the Poisson's ratio of the diaphragm material,
 m : is the reciprocal of the Poisson's ratio

Eq. 1, Eq.2, Eq. 3 and Eq. 4 are describing for performing the analytical analysis of the proposed MEMS based capacitive pressure sensor. The capacitance between two parallel electric conductive plates is given by [15- 16]:

$$C = \epsilon_0 \epsilon_r \frac{A}{d} \quad (5)$$

Where:

C : is capacitance,
 ϵ_0 : is dielectric constant of vacuum,
 ϵ_r : is the dielectric constant of material,
 A : is area of electrode plate,
 d : is the gap between two electrode plate.

The relationship between the capacitance change and the applied pressure for circular and square diaphragms is defined as sensitivity and is given by [17-21]:

$$S = \frac{\Delta C}{P} = \frac{3(1-\gamma^2)R^4 \epsilon_0 \epsilon_r A_{sense}}{16Eh^3g^2} \quad (6)$$

Where:

S : is the sensitivity,
 ΔC : is the change in capacitance,
 P : is the pressure difference across the diaphragm,
 R " is the radius of the diaphragm,

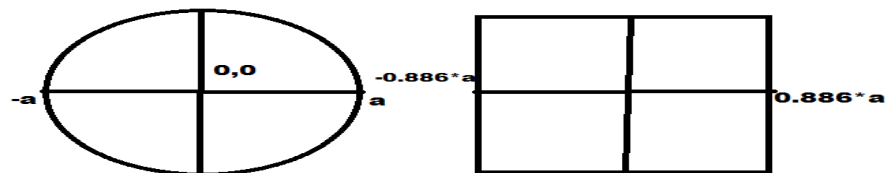
- h : is the thickness of the diaphragm
- E : is the Young's modulus of the diaphragm material,
- γ : is the Poission's ratio of the diaphragm material,
- A_{sense} " is the area of the moving plate
- g : is the sensing gap between the moving plate and the fixed plate

B. Matlab modeling

Matlab software is used to predict mechanical response to a load, such as force or moment applied to a part of the constructed model. This part is to be simulated is broken down into small discrete element – this procedure is called meshing. Each element has a no. of nodes and its corners at which it interacts with neighboring element. Thus the system Partial Differential Equation (PDEs) is assumed to be linear element within the nodes and is solved in matlab modeling.

C. Sensor layout

For design purpose, the two different geometries (circular and square) of the diaphragm are designed in such a way that their area between the plates is made similar. Both cases there are two plates. Lower one is fixed and upper one is movable. Pressure is applied on upper plate. Distance between two plates changes when pressure is applied and due to these capacitance changes. The dimensions of both the square and circular shaped capacitive pressure sensor is provided below as shown in Fig. 1



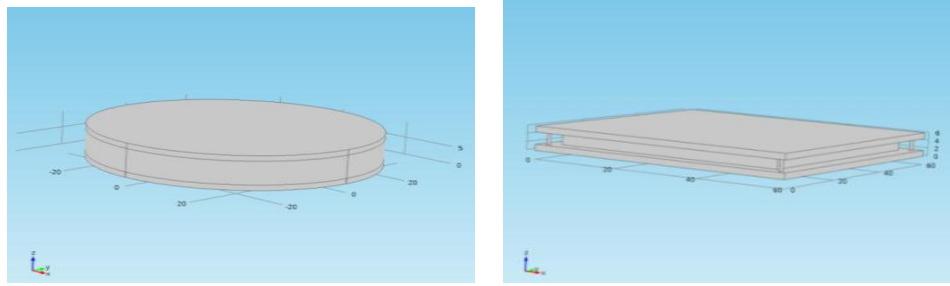


Fig. 1: Cross-section and 3D view of the sensor geometries

Table 1: Parameters used in MEMS capacitive pressure sensor

Side length of square diaphragm [μm]	60
Radius of circular diaphragm [μm]	33.84
Thickness of diaphragm [μm]	1.5
Separation gap between the plates [μm]	3.0

3. Material Analysis

The physical properties of Polysilicon are recorded in table 2. These properties are used in performing the analysis of the two designed MEMS based capacitive pressure sensor model in Matlab software.

Table 2: Properties of Polysilicon material

Young's modulus [pa]	160×10^9
Poisson's ratio	0.22
Density [kg/m^3]	2320
Thermal expansion coefficient [K^{-1}]	2.6×10^{-6}
Thermal conductivity [$W/m \cdot K$]	34
Relative permittivity	4.5

4. Results and discussion

A wide range of mechanical, electromechanical and polysilicon material studies of the proposed two geometrical structures have been performed in the Matlab Software. In this paper, effect of various parameters for designing sensor is analyzed and discussed below.

A. Design sensor layout

Two types of geometrics are designed. Sensor layouts are given on Fig.2 and Fig.3. Deflection is maximum at center of the diaphragm and minimum at side of the diaphragm.

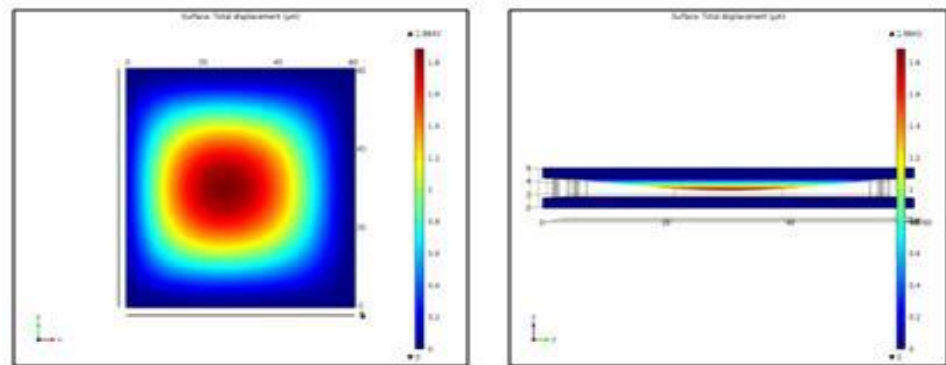


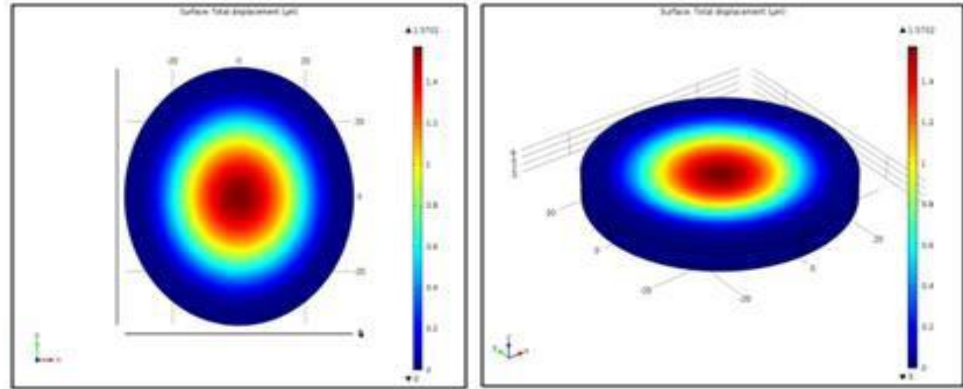
Fig.2: Square sensor layout (a) top view (b) side view

Applied pressure vs. deflection is measured and change in capacitance is measured. In Fig. 2(a, b) and 3(a, b) red colure shows maximum deflection at center of the diaphragm and blue colure shows minimum deflection at side of the diaphragm.

B. Effect of Distance between two Diaphragms

Distance between two diaphragms is very important parameter for designing diaphragm type capacitive pressure sensor. If the distance

between two plates increases, the capacitance decreases. In Fig.4, the change in capacitance due to varying distance between two diaphragms is plotted. These studies we have done only with square shaped diaphragm as the area of two geometrical shapes diaphragms is considered as equal.



(a) (b)

Fig.3: Circular sensor layout (a) top view (b) side view

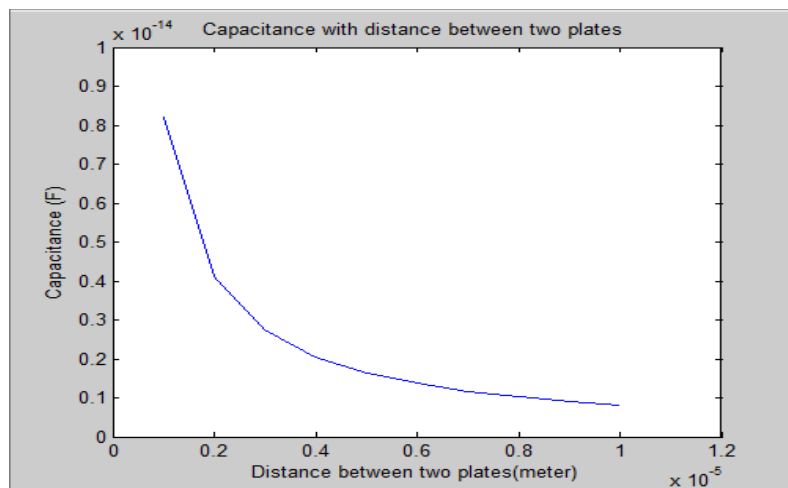


Fig. 4: Plot of capacitance with the variation of the distance between the plates

C. Effect of thickness of diaphragm on sensor performance

1- Deflection

Thickness is very important parameter for diaphragm deflection. If diaphragm thickness is increased, deflection decreases. Diaphragm deflection is inversely proportional to diaphragm thickness as shown in Fig.5 (a) circular diaphragm and Fig.5 (b) square diaphragm, which show how the deflection for different diaphragm thickness varying with applied pressure. For different diaphragm thickness, deflection in circular shaped diaphragm is higher than in square shaped diaphragm. FEM and MATLAB results [12] showed that the deflection increased with applied pressure as theoretically predicted in Eq. (2) and Eq. (4) as shown in Fig. 5(a).

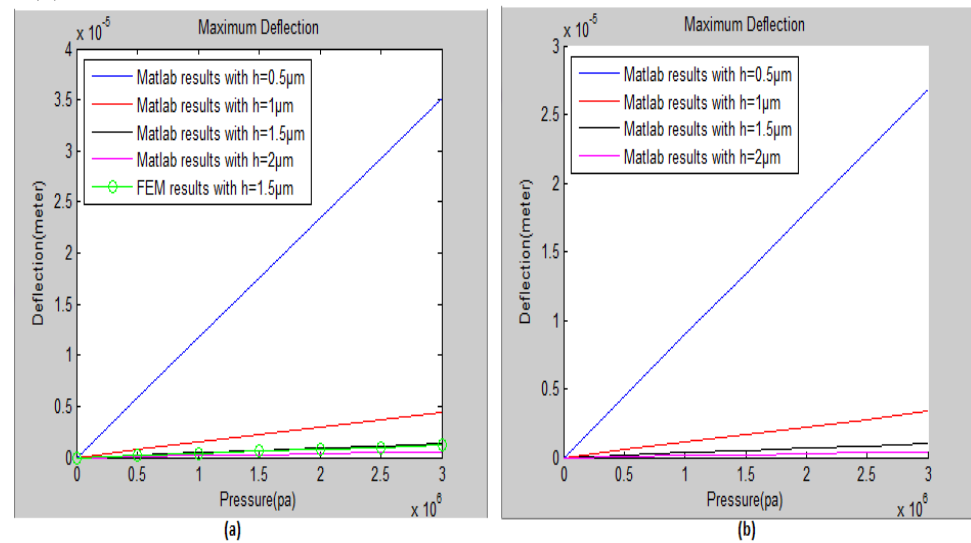


Fig.5: Plot of the deflection with diaphragm thickness, with the range of applied pressure from (0-3) MPa (a) For circular shaped diaphragm, (b) For square shaped diaphragm.

2- Stress

If diaphragm thickness is increased, stress decreases. Diaphragm stress is inversely proportional to diaphragm thickness as shown in Fig.6 (a)

circular diaphragm and Fig.6 (b) square diaphragm, which show how the stress for different diaphragm thickness varying with applied pressure. If diaphragm thickness increases then pressure withstand capability also increases. For different diaphragm thickness, stress in square shaped diaphragm is much higher than in circular shaped diaphragm.

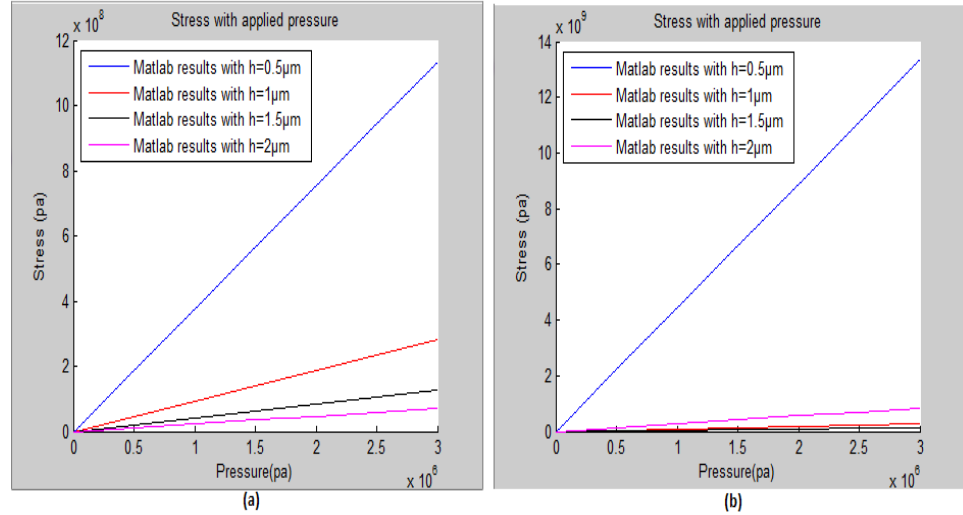


Fig.6: Plot of the stress through different diaphragm thickness with the range of applied pressure from (0-3) MPa (a) For circular shaped diaphragm, (b) For square shaped diaphragm.

3- Change in capacitance

Change in capacitance is measured with respect to applied pressure is shown in Fig.7 (a) circular diaphragm and Fig.7 (b) square diaphragm; it is observed that applied pressure vs. change in capacitance is maximum for thin diaphragm. As a result, low thickness diaphragm is more sensitive than high thickness diaphragm. For different diaphragm thickness, change in capacitance in circular shaped diaphragm is much higher than in square shaped diaphragm. FEM and MATLAB results [12] showed that the change in capacitance increased with applied pressure as shown in Fig. 7(a and b).

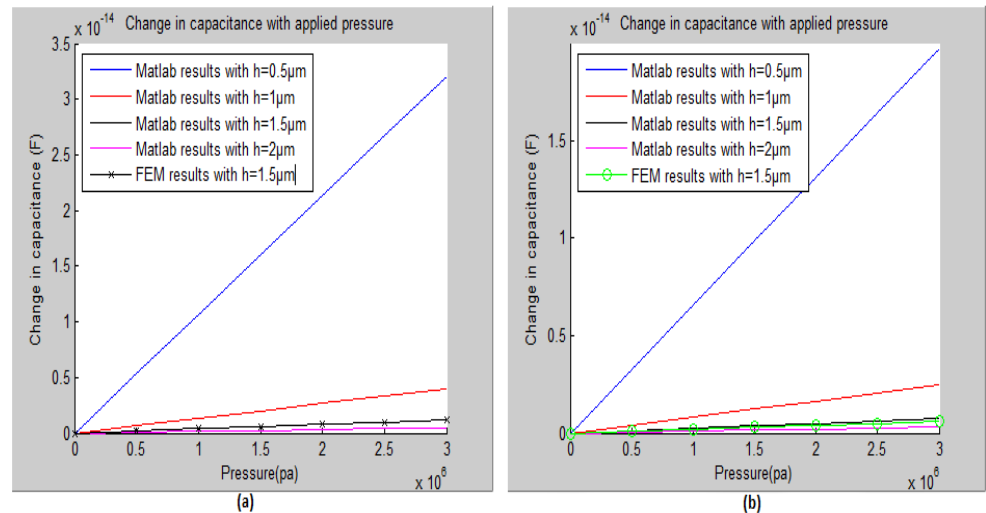


Fig.7: Plot of change in capacitance through different diaphragm thickness with the range of applied pressure from (0-3) MPa (a) For circular shaped diaphragm, (b) For square shaped diaphragm.

4- Sensitivity

If diaphragm thickness is increased, sensitivity decreases. Diaphragm sensitivity is inversely proportional to diaphragm thickness as shown in Fig.8 (a) circular diaphragm and Fig.8 (b) square diaphragm, which show how the sensitivity for different diaphragm thickness varying with applied pressure. If diaphragm thickness increases then pressure withstand capability also increases. For different diaphragm thickness, sensitivity in circular shaped diaphragm is much higher than in square shaped diaphragm.

D- Effect of applied pressure on sensor performance

1- Deflection

If applied pressure is increased, deflection increases as shown in Fig.9 (a) circular diaphragm and Fig.9 (b) square diaphragm, which show how the

deflection for different applied pressure varying with diaphragm thickness. For different applied pressure, deflection in circular shaped diaphragm is higher than in square shaped diaphragm.

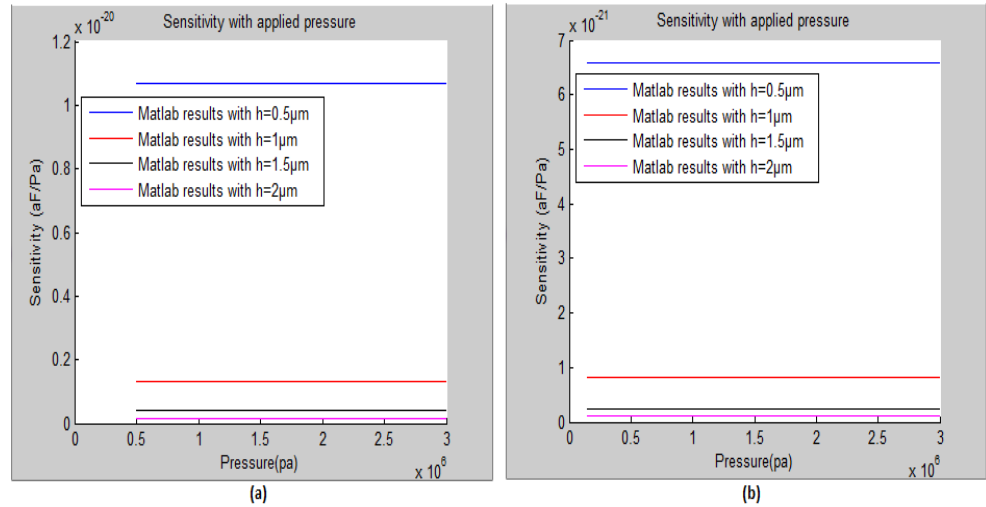


Fig.8: Plot of sensitivity through different diaphragm thickness with the range of applied pressure from (0-3) MPa (a) For circular shaped diaphragm, (b) For square shaped diaphragm.

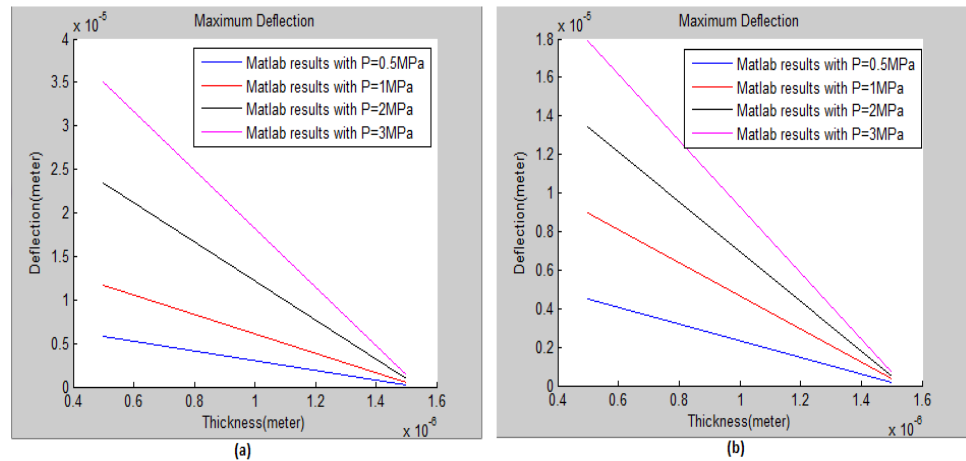


Fig.9: Plot of the deflection through different applied pressure with the range of diaphragm thickness (a) For circular shaped diaphragm, (b) For square shaped diaphragm.

2- Stress

If applied pressure is increased, stress increases as shown in Fig.10 (a) circular diaphragm and Fig.10 (b) square diaphragm, which show how the stress for different applied pressure varying with diaphragm thickness. For different applied pressure, stress in square shaped diaphragm is much higher than in circular shaped diaphragm.

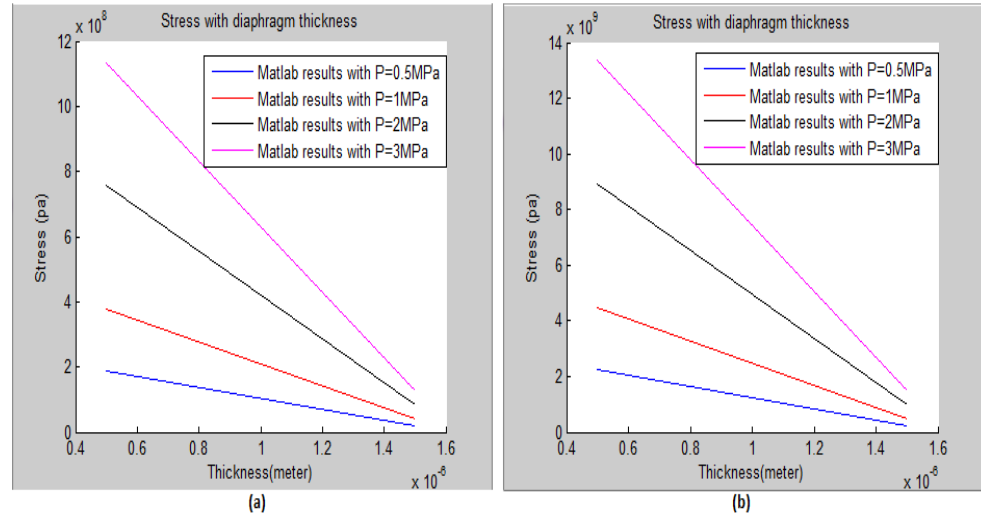


Fig.10: Plot of the stress through different applied pressure with the range of diaphragm thickness (a) For circular shaped diaphragm, (b) For square shaped diaphragm.

3- Change in capacitance

Change in capacitance is measured with respect to diaphragm thickness is shown in Fig.11 (a) circular diaphragm and Fig.11 (b) square diaphragm; it is observed that diaphragm thickness vs. change in capacitance is maximum for thin diaphragm. For different applied pressure, change in capacitance in circular shaped diaphragm is much higher than in square shaped diaphragm.

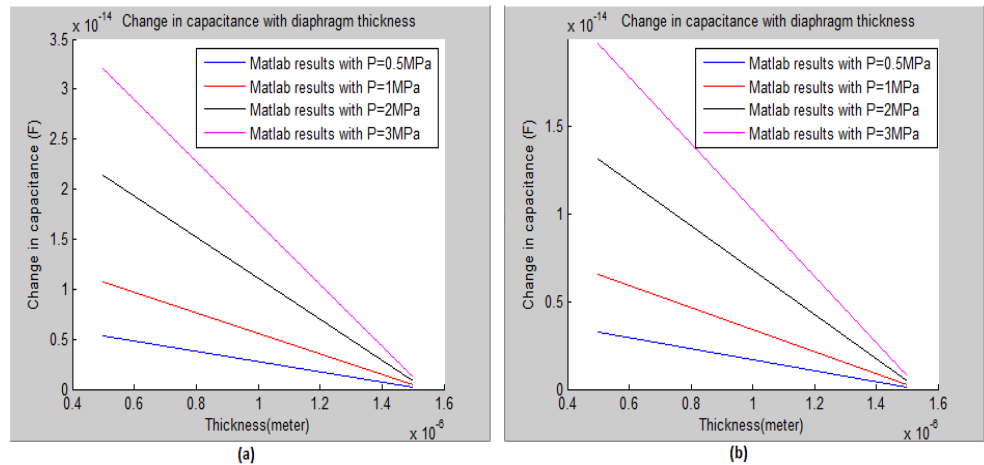


Fig.11: Plot of the change in capacitance through different diaphragm thickness with the range of applied pressure (a) For circular shaped diaphragm, (b) For square shaped diaphragm.

4- Sensitivity

If applied pressure is increased, sensitivity decreases. Diaphragm sensitivity is inversely proportional to applied pressure as shown in Fig.12 (a) circular diaphragm and Fig.12 (b) square diaphragm, which show how the sensitivity for different applied pressure varying with diaphragm thickness. For different applied pressure, sensitivity in circular shaped diaphragm is much higher than in square shaped diaphragm.

Table 3: Results obtained for both circular and square diaphragms at pressure 3 MPa

Performance of sensor	Circular diaphragm				Square diaphragm			
	h=0.5 μm	h=1 μm	h=1.5 μm	h=2 μm	h=0.5 μm	h=1 μm	h=1.5 μm	h=2 μm
Deflection (μm)	35	4.3	1.3	0.54	26	3.3	0.99	0.41
Stress (MPa)	1130	283	125.97	70.85	13300	3330	1483.2	834.3
Sensitivity (aF/Pa)	10.68 $\times 10^{-21}$	1.335 $\times 10^{-21}$	0.39 $\times 10^{-21}$	0.1669 $\times 10^{-21}$	6.578 $\times 10^{-21}$	0.822 $\times 10^{-21}$	0.243 $\times 10^{-21}$	0.102 $\times 10^{-21}$

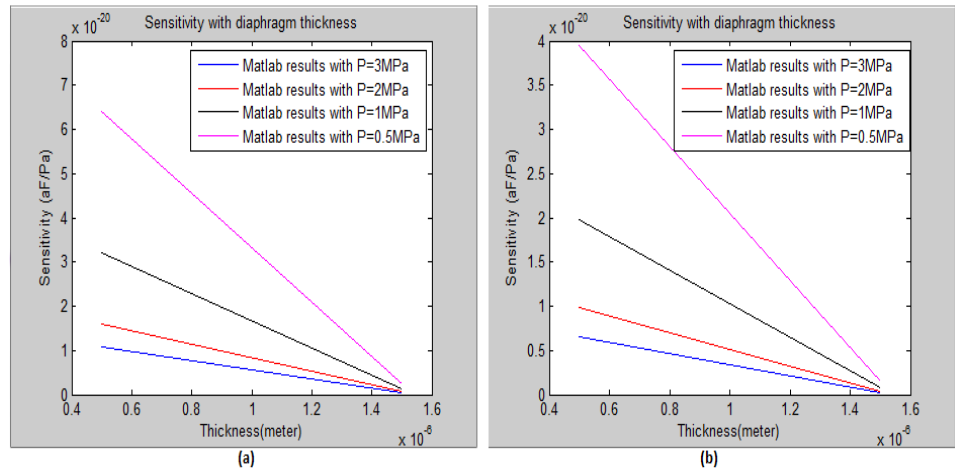


Fig.12: Plot of the sensitivity through different applied pressure with the range of diaphragm thickness (a) For circular shaped diaphragm, (b) For square shaped diaphragm

Table 4: Results obtained for both circular and square diaphragms at diaphragm thickness 0.5µm

Performance of sensor	Circular diaphragm				Square diaphragm			
	P=0.5 MPa	P=1 MPa	P=2 MPa	P=3 MPa	P=0.5 MPa	P=1 MPa	P=2 MPa	P=3 MPa
Deflection (µm)	5.8	11	23	35	4.4	8.9	13	17
Stress (MPa)	188	377	755	1130	2220	4440	8890	13300
Sensitivity (aF/Pa)	64 x10 ⁻²¹	32 x10 ⁻²¹	16 x10 ⁻²¹	10.6 x10 ⁻²¹	39 x10 ⁻²¹	19 x10 ⁻²¹	9.8 x10 ⁻²¹	6.5 x10 ⁻²¹

5. Conclusions

In this paper, two different models of MEMS based capacitive pressure sensor are analyzed. One having circular shaped whereas other having square shaped diaphragm. The results obtained evaluating the performance of MEMS capacitive

pressure sensor for both circular and square diaphragms in deflection, stress and sensitivity as shown in tables 3 and 4.

Detailed simulation based analyses on the mechanical, electromechanical as well as polysilicon material was performed. From the results obtained, it is shown that the circular diaphragm has the lowest stress on its edges when applying the same pressure as on a square diaphragm, but the largest centre deflection can be seen in circular diaphragm and sensitivity of circular diaphragm is greater than sensitivity of square diaphragm. Besides, Matlab modeling was performed to simulate the mechanical characteristics of the diaphragm and the comparison to FEM (Finite Element Method) based Multiphysics simulation platform is presented. As analyzed from the mechanical analysis that designed model can withstand a high absolute pressure range extends to several of mega Pascals. This design technology allows for simple and inexpensive batch fabrication and integration of this type of sensors with dedicated signal detection circuits. Thus, the practical implementation of these designed sensors will cater wide range of applications over a varied field (biomedical, robotics etc).

References

- [1] Y. Kanda, A graphical representation of the piezoresistance coefficients in silicon, IEEE Transactions on Electron Devices ED-29 (1982) 64–70
- [2] J.-S. Park, Y.B. Gianchandani, A servo-controlled capacitive pressure sensor using a capped-cylinder structure microfabricated by a three-mask process, Journal of Microelectromechanical Systems 12 (2003) 209–220.
- [3] K. Kasten, J. Amelung, W. Mokwa, CMOS-compatible capacitive high temperature pressure sensors, Sensors and Actuators 85 (2000) 147–152.
- [4] C.Kolle, W. Scherr, D. Hammerschmidt, G. Pichler, M. Motz, B. Schaffer, B. Forster, U. Ausserlechner, Ultra low-power monolithically integrated capacitive pressure sensor for tire pressure monitoring, in: Proceedings of IEEE Sensors, Vienna, Austria, 24–27 October 2004, 2004, pp. 244–247.
- [5] M. Habibi, E. Lueder, T. Kallfass, D. Horst, A surface micromachined capacitive absolute pressure sensor array on a glass substrate, Sensors and Actuators A 46–47 (1995) 125–128.
- [6] U. Paschen, M. Leineweber, J. Amelung, M. Schmidt, G. Zimmer, A novel tactile sensor system for heavy-load applications based on an integrated capacitive pressure sensor, Sensors and Actuators A 68 (1998) 294–298.

- [7] W.H.Ko,Q.Wang, Touchmode capacitive pressure sensor, *Sensors and Actuators* 75 (1999) 242–251.
- [8] P. Dimitropoulos, C. Kachris, D. Karampatzakis, G. Stamoulis, A new SOI monolithic capacitive sensor for absolute and differential pressure measurements, *Sensors and Actuators A* 123–124 (2005) 36–43.
- [9] S.T. Moe, K. Schjølberg-Henriksen, D.T.Wand, E. Lund, J. Nysæther, L. Furuberg,M. Visser, T. Fallet, R.W. Bernstein, Capacitive differential pressure sensors for harsh environments, *Sensors and Actuators A* 83 (2000) 30–33.
- [10] R. Puers, Capacitive sensors: when and how to use them, *Sensors and Actuators A* 37–38 (1993) 93–105.
- [11] A.V. Chavan, K.D. Wise, Batch-processed vacuum-sealed capacitive pressure sensors, *J. of Microelectromechanical Syst.* 4 (10),580–588, 2001.
- [12] P. S. Roy, M. Chattopadhyay, "A Simulation Based Geometrical Analysis of MEMS Capacitive Pressure Sensors for High Absolute Pressure Measurement", ISSN 2250-2459, IESA 2014.
- [13] D. M. M Zeena," Design and Implementation of Piezo Resistive MEMS Pressure Sensor for Spiro Meter Application", *International Journal of Innovative Research in Science, Engineering and Technology*, Volume 3, Special Issue 3, March 2014.
- [14] A.A. Barlian , W.-T. Park, J.R. Mallon, A.J.Rastegar, and B.L. Pruitt, "Review: Semiconductor Piezoresistance for Microsystems," *Proc. IEEE*, vol.97, no.3, pp.513-552,2009.
- [15] Chang ,S.-P., and Allen ,M.G.,2004,"Capacitive Pressure Sensors with Stainless Steel Diaphragm and Substrate ." *J.Micromechan.Microeng.*, 14(4),pp.612-618.
- [16] Sathyanarayanan,S.,Vimala Juliet, A.,2007, " Design of Wireless Pressure Sensor for Monitoring Intraocular Pressure" *Proceedings of 2nd ISSS national conference on MEMS, Microsensors, Smart materials, Structures and Systems*, C36,pp.28-29.
- [17] Y. Zhang, S. Massoud-Ansari, G. Meng, W. Kim, and N. Najafi, "A Ultra-Sensitive, High-Vacuum Absolute Capacitive Pressure Sensor," *Technical Digest of the 14th IEEE Int. Conf. on Micro Electro Mechanical Systems (MEMS 2001)*, pp. 166-169, Interlaken, Switzerland, Jan. 21-25, 2001.
- [18] Y. Zhang and K. D. Wise, "A Barometric Pressure Sensor with Multiple Elements," *Digest IEEE Transducers '95 Stockholm, Sweden*, June 1995.
- [19] Y. Zhang and K. D. Wise, " An Ultra-Sensitive Capacitive Pressure Sensor with a Bossed Dielectric Diaphragms," *Technical Digest of IEEE Solid-state Sensors and Actuators workshop, Hilton Head Island*, June of 1994.

- [20] C. Hierold, B. Clasbrummel. "Low power integrated pressure sensor system for medical applications," Sensors and Actuators (Part A) Physical, no. 73, 1999, pp. 68-67
- [21] Bishnu P. Gogoi and David J. Monk, "Method of manufacturing a semiconductor component having a fixed electrode between two flexible diaphragms," U.S. Patent #6,426,239 B1, issued July 30, 2002.

ملخص البحث

في هذه الورقة البحثية نقدم تقييم للنظم الميكانيكية والكهربية الدقيقة الخاصة بأجهزة استشعار الضغط حيث يستخدم هذا النوع من استشعارات الضغط في قياس معدل النبض. تم تحليل الاداء لنوعين من اجهزة استشعار الضغط بأشكال هندسية مختلفة وذلك باستخدام برنامج المحاكاة الماتلاب حيث ان احد هذين النوعين يأخذ شكل دائري في حين الاخر يأخذ شكل مربع 0 تم تقييم اداء النظم الميكانيكية والكهربية الدقيقة الخاصة بأجهزة استشعار الضغط من خلال المقارنة بين الانحراف والضغط والحساسية لكلا النوعين من النتائج التي تم الحصول عليها، فإنه تبين أن الشكل الدائري لديه أدنى ضغط على أطرافه عند تطبيق نفس الضغط على الشكل المربع، ولكن يمكن ان ينظر الى اقصى انحراف وذلك من خلال الشكل الدائري عنه في الشكل المربع كما يتضح ان حساسية الشكل الدائري اعلى من حساسية الشكل المربع وتم عرض تلك النتائج على برنامج المحاكاة الماتلاب وتأكد من مطابقتها مع النتائج الموضحة على برنامج (FEM). ولهذا يتضح من التحليل الميكانيكي ان هذا النموذج المصمم يمكن ان يتحمل اقصى مدى من الضغط المطلق يصل الى (several of mega Pascals). هذا التصميم التكنولوجي يسمح بتصنيع ودمج هذه الانواع من اجهزة استشعار الضغط مع الدوائر المخصصة في كشف الاشارة وذلك ببساطة وقلّة في التكاليف وهكذا، فإن التنفيذ العملي لهذه المجسات مصممة لتلبية مجموعة واسعة من التطبيقات في مجالات متنوعة مثل (الطب الحيوي، الروبوتات... الخ).

High Density Noise Removal in Endangered Silent-Films Using Non-linear Filters: A Comparative Study

Hassan M. ElKamchouchi*, Ahmed E. Khalil* and Samy H. Darwish**

* Faculty of Engineering, Alexandria University, Alexandria, Egypt.

** Faculty of Engineering, Pharos University in Alexandria, PUA Alexandria, Egypt

(Received: 07-July-2015 – Accepted: 04- September-2015)

Abstract

The loss and distortion of the feature films at films silent-era constitutes an alarming in cultural recording for most nation's. So the first directive of congress library was to support archival research projects that would restore the American movies produced during the 19th and 20th centuries. Noise removal is an important task in video restoration where the "original" video is discernible. Therefore this work contemplates to introduce an overview of some algorithms that can be used to restore the corrupted video that presented in AVI container format. These algorithms are untrimmed decision based median filter (UDBMF), decision based median filter (DBMF), weighted median filter (WMF), and standard median filter (SMF). A comparable analysis among all filters was done at different levels of noise based on some calculated parameters as mean square error (MSE), mean absolute error (MAE), image enhancement factor (IEF), peak signal to noise ratio (PSNR), and correlation ratio (CORR). Simulation results indicate that DBMF and UDBMF have superior performance compared to other nonlinear filters for noise level up to ninety percent. Also the necessary details in video were preserved.

1. Introduction

An image is an array or a matrix of square pixels (picture elements) arranged in columns and rows. Image may be captured in optical devices such as telescopes, lenses, mirrors, cameras, microscopes, etc., and natural

objects and phenomena, such as the human eye or the water surfaces. The word image is also used in the broader sense of any two-dimensional figure. In wider sense; images can also be rendering manually, such as by painting, drawing, carving, rendered automatically by computer graphics technology, printing, or developed by a combination of methods [1].

Digital images and digital video are, respectively, pictures and movies that have been converted into a computer- readable format. Usually, image means a still picture that does not change with time, whereas a video evolves with time and generally contains moving and/or changing objects. Digital images or video are usually obtained by converting continuous signals into digital format. Likewise, digital visual signals are viewed by using diverse display media, included digital printers, computer monitors, and digital projection devices [2].

Video frames are often corrupted by impulse noise. In general, the impulse noise in video frames is present due to bit errors in transmission or introduced during the signal acquisition stage. Based on the noise values, the impulse noise is classified into two types; salt and pepper noise (fixed valued noise) and random valued noise. Salt and Pepper noise can corrupt the frame where the corrupted pixel takes either maximum or minimum gray level. Random valued impulse noise, in which noise is dispersed uniformly. It may take any value in the dynamic range of [0,255]. In this paper a deal with the removal of salt and pepper noise from corrupted video images [3].

Linear filters were the primary tools that used with signal and image denoising but it tend to blur edges, do not remove impulsive noise effectively, and do not perform well in the presence of signal dependent noise [4]. To overcome these shortcomings, nonlinear filters have replaced linear filters in many image processing applications since they can operate effectively in various noisy conditions and potentially preserve the structural information of the image, so various types of nonlinear filters are used [5].

To satisfy the objective of this work the paper has been structured as follows; section II describes restoration process, section III contains sources of noise in video images and its types. Section IV discusses the means of image de-noising, while filtering techniques are given in section V. Section VI briefly illustrates the suggested methodology. Simulation

and the discussions of results are presented in section VII. Conclusions are drawn in section VIII. Section IX gives a scope of the future work. Finally, the references that used for completion of this work were incorporated.

2. RESTORATION PROCESS

Image Restoration is an attempt to reconstruct or recover a video frame that has been degraded by using a priori knowledge of the degraded phenomenon. Thus, restoration techniques are oriented toward modeling the degradation and applying the inverse process in order to restore the original image [6]. The idea of image restoration is to balance for or unwrap a defect which corrupts an image. Degradation comes in many forms such as motion blur, noise, and camera misfocus. In cases where the image is corrupted by noise, the best hope is to compensate for the degradation it caused [7].

The objective of image restoration procedures is to suppress degradation of the image with the help of the knowledge about its nature. The image degradation could be attributed to the defects present in the optical lenses, relative motion between the object and the camera, wrong focus, turbulence in the atmosphere, scanning quality etc. The goal of image restoration is to reconstruct the original image from its degraded form. The image restoration techniques can be broadly classified into two groups as: (1) deterministic and (2) stochastic. Deterministic method suits in restoring images with a little noise and a known degradation function. The original image can be obtained by applying a transformation inverse to the degradation of the degraded image. Stochastic technique tries to find the best restoration according to a particular stochastic criterion [8].

The possible approach for noise removal is using filters such as low-pass filters or median filters. More sophisticated methods assume a model of how the local image structures look like, a model which distinguishes them from the noise; that's by first analyzing the image data in terms of the local image structures, such as lines or edges, and then controlling the filtering based on local information from the analysis step [6].

Restoring an original image, when given the degraded image, with or without knowledge of the degradation function degree and type of noise

present is an ill posed problem [9]. Fig.1. Shows block diagram for the degradation/ restoration process. The objective of restoration is to find the estimated $F(x,y)$ that closely approximates the original input image $f(x,y)$ [10].

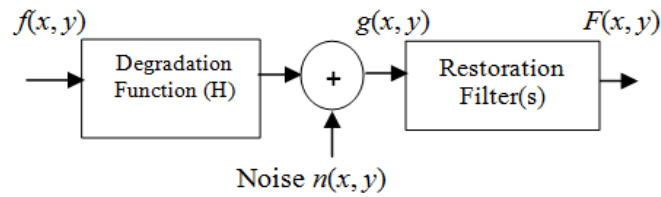


Fig.1. Model of the image degradation/restoration process

Where, $f(x,y)$ is a given input image, H is a degradation function, $n(x,y)$ is the additive noise, $g(x,y)$ is the degraded image, and $F(x,y)$ is the restored image.

3. SOURCES of NOISE in IMAGES and ITS TYPES

Noise is a disturbance that affects a signal; it may distort the information carried by the signal. Presence of noise is manifested by undesirable information, which is not at all related to the image under study, but in turn disturbs the information present in the image. The noise is translated into values, which are getting added or subtracted to the values on the levels of image pixels. Image noise can be originated due to camera quality, acquisition condition, illumination level, calibration. Image noise can also be occurred due to the electronic noise in the sensors in the digital cameras, and it can be a function of the scene environment [11].

Image noise can be classified as Impulse noise (Salt-and-pepper noise), Amplifier noise (Gaussian noise), Shot noise, Quantization noise (uniform noise), Film grain, non-isotropic noise, Multiplicative noise (Speckle noise) and Periodic noise [12].

A. Various Sources Of Noise

In signal processing or computing it can be considered data without meaning; that is, data not being used to transmit a signal, but is simply produced as an unwanted by-product of other activities. In Information

Theory, however, noise is still considered to be information. In a broader sense, film grain or even advertisements in web pages can be considered as noise [4].

Reference [12] introduces noise in the image at the time of image acquisition or transmission. Different factors may be responsible for introducing noise in the image. The number of pixels corrupted in the image will define the quantification of the noise. The principal sources of noise in the digital image are:

- The imaging sensor may be affected by environmental conditions during image acquisition.
- Insufficient light levels and sensor temperature may introduce noise in the image.
- Interference in the transmission channel may also corrupt the image.
- If dust particles are present on the scanner screen, they can also introduce noise in the image.

B. Types Of Noises

Noise is to be any degradation in the image signal caused by external disturbance [13]. If an image is being sent electronically from one place to another via satellite or wireless transmission or through networked cables, the expecting errors may be occurred in the image signal. These errors will appear on the image output in different ways depending on the type of disturbance in the signal [14]. The type of noise and errors in the image can be expected as:

1. Amplifier Noise (Gaussian noise): The standard model of amplifier noise is additive, Gaussian, dependent at each pixel and dependent of the signal intensity, caused primarily by Johnson–Nyquist noise (thermal noise), including that which comes from the reset noise of capacitors ("kTC noise"). It is an idealized form of white noise, which is caused by random fluctuations in the signal [14]. Amplifier noise is a major part of the noise of an image sensor, that is, of the constant noise level in dark areas of the image. In Gaussian noise, each pixel in the image will be changed from its original value by a (usually) small amount. A histogram, the amount of distortion of a pixel value against

the frequency with which it occurs, shows a normal distribution of noise. While other distributions are possible, the Gaussian (normal) distribution is usually a good model, due to the central limit theorem that says that the sum of different noises tends to approach a Gaussian distribution [15].

2. Impulse Noise: Impulse noise is a short duration noise that affects the contents of digital images. Impulse noise is normally produced due to electromagnetic interference, errors and scratches on recording disks, malfunctioning of pixel elements in the camera sensors, faulty memory location and erroneous synchronization in digital recording and communication equipment [16]. Impulse noise distorts image pixels where replacing the original value either by fixed value or random value. Two types of impulse noise are fixed value impulse noise and random-valued impulse noise. Fixed value impulse noise e.g. Salt and pepper noise in which the gray value takes a value of either 255 or 0, Random-valued impulse noise, in which noise is dispersed uniformly. It may take any value in the dynamic range of [0,255]. It is therefore apparent that the original pixel and the random-valued impulse noise have the same range of values. Random valued impulse noise is difficult to remove [17].

In salt and pepper noise model, there are only two possible values 'a' and 'b'. The probability of getting each of them is less than 0.1 (else, the noise would greatly dominate the image). For 8 bit/pixel image, the intensity value for pepper noise typically found nearer to 0 and for salt noise it is near to 255. Salt and pepper noise is a generalized form of noise typically seen in images [2]. In image criteria the noise itself represents as randomly occurring white and black pixels. An effective noise reduction algorithm for this type of noise involves the usage of a median filter, morphological filter [18].

3. Multiplicative Noise (Speckle noise): This kind of noise is also called as the speckled noise. This noise gives a 'magnified' view of the original image. For *example*, when this noise is applied to high pixel intensities or bright area in an image, a higher random variation will be observed. On the other hand, when this noise is applied to a darker region in the image, the random variation observed is not that much as compared to that observed in the brighter areas. Thus, this type of noise is signal dependent and distorts the image in a big way [11].

Speckle noise is a granular noise. This noise generally degrades Synthetic Aperture Radar (SAR) images to large extent. This noise is generally caused due to random ups and downs in the signal coming back from an object that is smaller than a single image-processing element. It is also caused by consistent processing of backscattered signals from number of distributed targets. This noise also increases the mean gray level of affecting image. This noise creates a lot of difficulty in interpreting the image [19].

4. **Poisson Noise (Shot Noise):** The dominant noise in the lighter parts of an image from an image sensor is typically that caused by statistical quantum fluctuations, that is, variation in the number of photons sensed at a given exposure level; this *noise* is known as photon shot noise. Shot noise has a root mean- square value proportional to the square root of the image intensity, and the noises at different pixels are independent of one another. Shot noise follows a Poisson distribution, which is usually not very different from Gaussian. In addition to photon shot noise, there can be *additional* shot noise from the dark leakage current in the image sensor; so this noise is known as "dark shot noise" or "dark-current shot noise"[15].
5. **Quantization Noise (Uniform Noise):** The Uniform noise caused by quantizing the pixels of image to a number of distinct levels is known as Quantization noise. It has approximately uniform distribution. In this type of noise, the levels of *the* gray values of the noise are uniformly distributed over a specified range. It can be used to create any type of noise distribution. This type of noise is mostly used to evaluate the performance of image restoration algorithms. This noise provides the most neutral or unbiased noise [20].
6. **Film Grain:** The grain of photographic film is a signal-dependent noise, related to shot noise. That is, if film grains are uniformly distributed (equal number per area), and if each grain has an equal and independent probability of developing to a dark silver grain after absorbing photons, then the number of such dark grains in an area will be random with a binomial distribution. In areas where the probability is low, this distribution will be close to the classic Poisson distribution of shot noise; nevertheless a simple Gaussian distribution is often used as an accurate model [15].

7. **Non-Isotropic Noise:** Some noise sources show up with a significant orientation in images. For example, image sensors are sometimes subjected to row noise or column noise. In film, scratches are an example of non-isotropic noise. While cannot completely do away with image noise, it can certainly reduce some of it. Corrective filters are yet other devices that help in reducing image noise. [15].

8. **Periodic Noise:** If the image signal is subjected to a periodic rather than a random *disturbance*, an image corrupted by periodic noise is obtained. The effect is of bars over the image [15].

4. IMAGE DE-NOISING

Image denoising is considered as an important step and is generally done prior to processing of an image. It shows the process of recovering a good estimate of the original image from a corrupted image without modifying the useful structure in the image such as edges, discontinuities and fine details [21].

Many algorithms have been implemented for denoising and each algorithm has its advantages and limitations. Having a good knowledge about the noise present in the image will be crucial in selecting a suitable denoising algorithm. The significance of the image denoising could be a weighty task for medical imaging, satellite image processing, and space exploring etc. A wide variety of noise types are present and good number of denoise filters have been developed to reduce noise from degraded images to enhance image quality by preserving edges. [8]. It has many applications in other domains like object recognition, digital entertainment, and remote sensing imaging etc. As the number of image sensors per unit area increases, camera devices capture the noise with the image more often [22].

In early times, as the signals handled, the analog, filters were used. Gradually digital filters were took place because of their flexibility, low cost, programmability, reliability, etc. The design-of digital filters involves three basic steps: (1) the specification of the desired properties of the system, (2) the approximation of these specifications using a causal discrete time system, and (3) the realization of the system using finite precision arithmetic [23].

FILTERING TECHNIQUES

Filtering in an image processing is a basis function that is used to achieve many tasks such as noise reduction, interpolation, and re-sampling. Filtering image data is a standard process used in almost all image processing systems. The choice of filter is determined by the nature of the task performed by filter and behavior and type of the data. Filters are used to remove noise from digital image while keeping the details of image preserved is a necessary part of image processing [24].

A traditional way to remove noise from image data is by using spatial filters. Spatial filters are a low pass filter. It can be further classified into nonlinear and linear filters. Linear filters, which consist of convolving the image with a constant matrix to obtain a linear combination of neighborhood values. They have been widely used for noise elimination in the presence of additive noise [25], Linear filters are used for generic tasks such as image/video contrast improvement, denoising, and sharpening, as well as for more object or feature specific tasks such as target matching and feature enhancement but it destroy lines and other fine image details [2]. Non-linear filters are used to remove the noise without any effort to explicitly identify it. These filters often remove noise to a reasonable extent but at the cost of blurring images and consequently makes the edges in image invisible [8].

A. Method Used

Some important turns seen the literature with the common frameworks used by these filters. The modifications of the basic frameworks with combination of one or two are used in different methods [5].

The standard median filter (SMF) is a simple nonlinear smoother that can suppress noise while retaining sharp sustained changes (edges) in signal values. The output of SM filter at a point is the median value of the input data inside the window centered at the point [5]. But the main drawback of this filter is that it is effective only for low noise densities. At high noise densities, SMF often exhibit blurring for large window size and insufficient noise suppression for small window size [3]. When the noise level is over 50%, the edge details of the original frame will not be preserved by SMF. However, most of the median filters operate uniformly and modifies both noise and noise-free pixels, and causes information

loss. Ideally, the filtering should be applied only to corrupted pixels not to uncorrupted ones [26].

One of the branches of median filter is weighted median filter (WMF). It was first introduced by Justusson in 1981, and further elaborated by Brownrigg. The operations involved in WMF are similar to those of SMF, except that WMF has weight associated with each of its filter element. These weights correspond to the number of sample duplications for the calculation of median value. However, the successfulness of weighted median filter in preserving image details is highly dependent on the weighting Coefficients and the nature of the input image itself. Unfortunately, in practical situations, it is difficult to find the suitable weighting coefficients for this filter, and this filter requires high computational time when the weights are large [5].

In decision based median filter (DBMF), the noisy and noise-free pixels in the image are detected by checking the pixel values against the maximum and minimum values which are in the dynamic range (0, 255). If the pixel being currently processed has a value within the minimum and maximum values in the currently processed window, then it is a noise-free pixel and no modification is made to that pixel. If the value doesn't within the range, then it is a noisy pixel and will be replaced by either the median pixel value or by the mean of the neighboring processed pixels (if the median itself is noisy) which ensure a smooth transition among the pixels [27].

In untrimmed decision based median filter (UDBMF), the selected 3 x 3 window elements are arranged in either increased or decreased order. This filter is called trimmed median filter because the pixel values 0's and 255's are removed from the selected window, then the median value of the remaining pixels is taken in consideration. This median value is used to replace the noisy pixel. The processing pixel is checked whether it is noisy or noise free. That is, if the processing pixel lies between maximum and minimum gray level values then it is noise free pixel, it is left unchanged. If the processing pixel takes the maximum or minimum gray level then it is noisy pixel which is processed by UDBMF [28, 29].

B. Performance Measures

To assess the performance of the proposed filters for removal of impulse noise and to evaluate their comparative performance, different standard

calculated parameters have been used [11, 20, 25–30]. These are defined as follows:

1) *Mean Squared Error (MSE)*: It is computed pixel-by- pixel by adding up the squared difference between the uncorrupted (original) image $s(i, j)$ and the restored image $r(i, j)$ and dividing by the total pixel count. It is defined as:

$$MSE = \frac{1}{m \times n} \sum_{i=1}^m \sum_{j=1}^n (s(i, j) - r(i, j))^2 \quad (1)$$

Where, $m \times n$ is image size; the minimum value of *MSE* reflects the better visual.

2) *Peak Signal to Noise Ratio (PSNR)*: is the ratio between the maximum pixel value of an image and the mean square error. It is measured in decibel (dB) and for gray scale image it is defined as:

$$PSNR(dB) = 10 \log_{10} \left[\frac{(255)^2}{MSE} \right] \quad (2)$$

The higher the value of the *PSNR* in the restored image, the better is its quality.

3) *Image Enhancement Factor (IEF)*: is a measure of Image quality, and is defined as:

$$IEF = \frac{\sum_i \sum_j [\psi(i, j) - s(i, j)]^2}{\sum_i \sum_j [r(i, j) - s(i, j)]^2} \quad (3)$$

Where $\psi(i, j)$ is the pixel value of the corrupted image, $r(i, j)$ and $s(i, j)$ are the pixel values of the restored and the original images respectively. The higher the value of *IEF* reflects the better visual, and restoration performance.

4) *Mean Absolute Error (MAE)*: is a quantity used to measure how close the restored image are to the original, and it is defined as:

$$MAE = \frac{1}{m \times n} \sum_{i=1}^m \sum_{j=1}^n |r(i, j) - s(i, j)| \quad (4)$$

Where, $r(i, j)$ and $s(i, j)$ are the pixel values of the restored and the original images respectively at the location (i, j) . The minimum value of MAE reflects the better visual.

5) *Correlation ratio (CORR)*: measures the degree to which two images vary together or oppositely and taking values from 0.0 to 1.0 and it is defined as:

$$CORR = \frac{\sum_i (x_i - x_m)(y_i - y_m)}{\sqrt{\sum_i (x_i - x_m)^2 (y_i - y_m)^2}} \quad (5)$$

Where x_i is the intensity of the i^{th} pixel in the original image, y_i is the intensity of the i^{th} pixel in the restored image, x_m is the mean intensity of the original image, and y_m is the mean intensity of the restored image. The value of *CORR*, which gets close to 1.0 reflects the better visual impression.

5. PROPOSED METHODOLOGY

A. Implementation for Video restoration Sequence:

The video sequence is first converted into frames and frames into images; impulsive noise (salt and pepper) was added at different levels of noise densities ranging from 5% up to 90% of salt and pepper to images. Specific filters were applied to the noisy images. After the filtering process was done the frames are converted back as a restored movie. Fig.2 shows the process flow.

- 1) *Video to Frames*: The video sequence (silent film) is converted into AVI format, and then frames are extracted from the Video.
- 2) *Frames to Images*: Frames are then converted into JPEG images for further processing.
- 3) *Noise Addition*: Add salt and pepper noise to images to become noisy images and then pass it through the Filtering process to remove the Impulse noise presented.
- 4) *Filtering*: The impulse noise from the noisy images is removed using the filters which are used.

- 5) *Frames to video*: After removal of impulse noise from all noisy images, the frames are converted back into video as a restored data at 15 f/s rate.

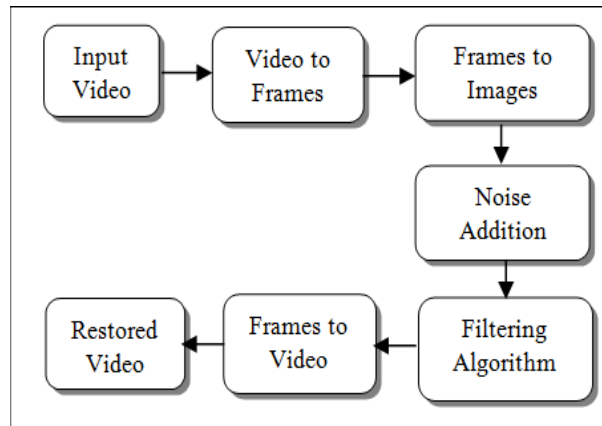


Fig.2. Block Diagram for restore processing of video Sequence.

B. The proposed algorithm

The proposed algorithm can be described in the following: read input video, then convert it to frames then, to images, an impulse noise were added with different levels of noise densities beginning with 5% up to 90% of salt and pepper. After having noisy image; different nonlinear filters were applied as SMF, WMF, DBMF and UDBMF, then a quantitative and qualitative parameters as MSE, MAE, IEF, PSNR, and CORR are calculated for each filter for comparison. Finally convert back the frames to video format in order to satisfy the discernible concept as a visual impression. Fig.3 illustrates the flow chart of the computerized program that used to satisfy the proposed restoration algorithm.

6. SIMULATION RESULTS & DISCUSSIONS

To validate the suggested methodology, a silent film in AVI format is used in the simulation at different levels of noise densities. The proposed algorithm has been implemented using five programs that designed under

MATLAB 7.10.0.499 (R2010a); as a language of technical computing. The performance of the proposed algorithm is evaluated with comparable study for various standard filters as: SMF, WMF, DBMF, and UDBMF. Figures (4-9) give the used noisy frames and the restored frames. The comparison was done in terms of MSE (1), PSNR (2), IEF (3), MAE (4), and CORR (5); where the results are illustrated in Fig.10.

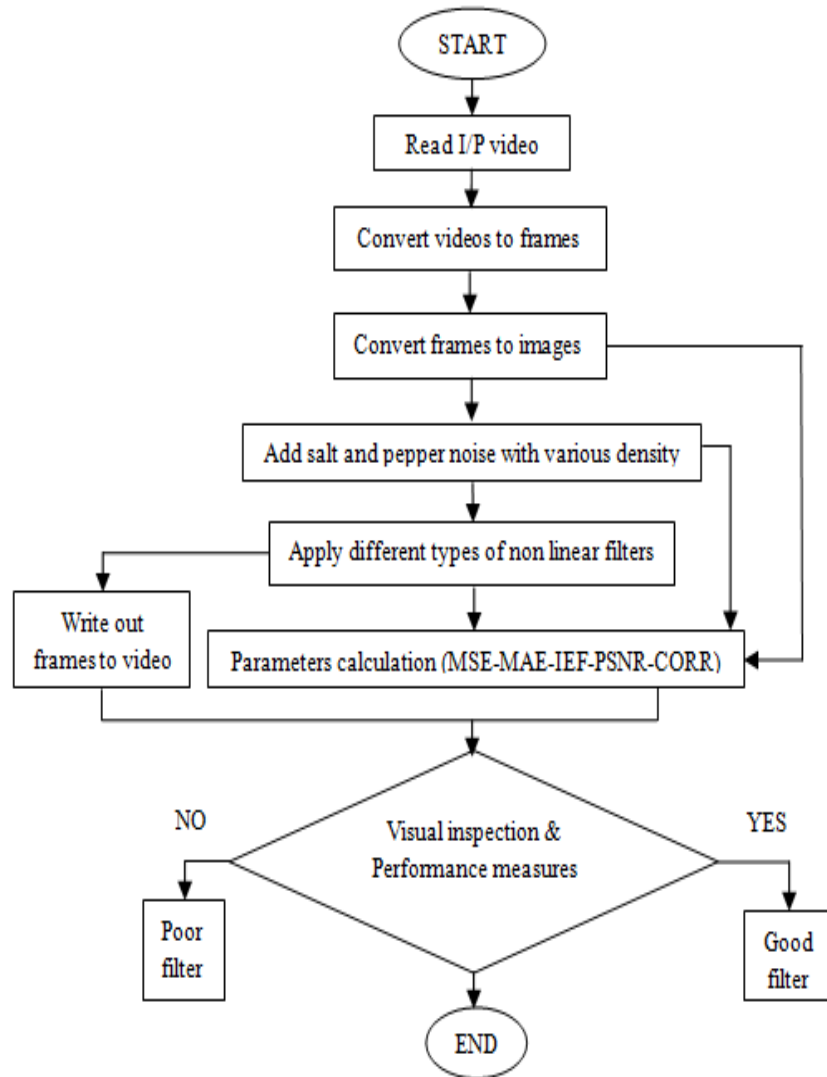


Fig.3. Flowchart of the proposed algorithm

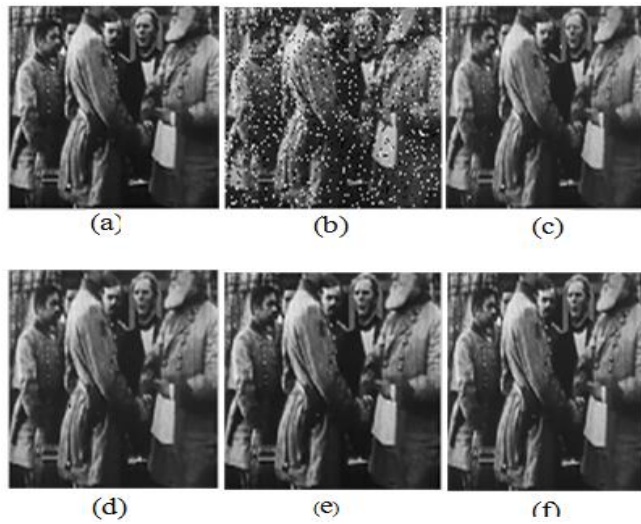


Fig.4. Results for 10% noise corrupted a selected first frame from silent film sequence. (a) Original frame, (b) Noisy frame, (c) WMF outputs, (d) SMF outputs, (e) DBMF outputs, and (f) shows the outputs of UDBMF.

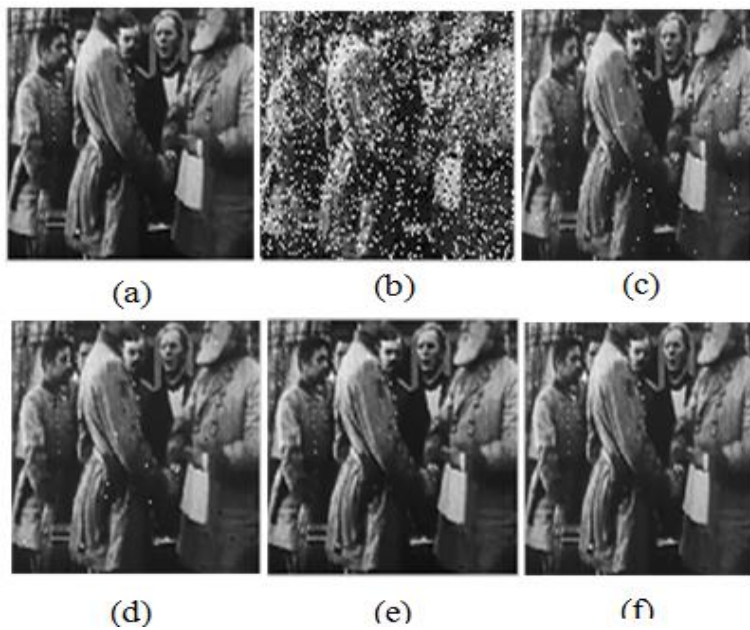


Fig.5. Results for 20% noise corrupted a selected first frame from silent film sequence. (a) Original frame, (b) Noisy frame, ((c) WMF outputs, (d) SMF outputs, (e) DBMF outputs, and (f) Shows the outputs of UDBMF.

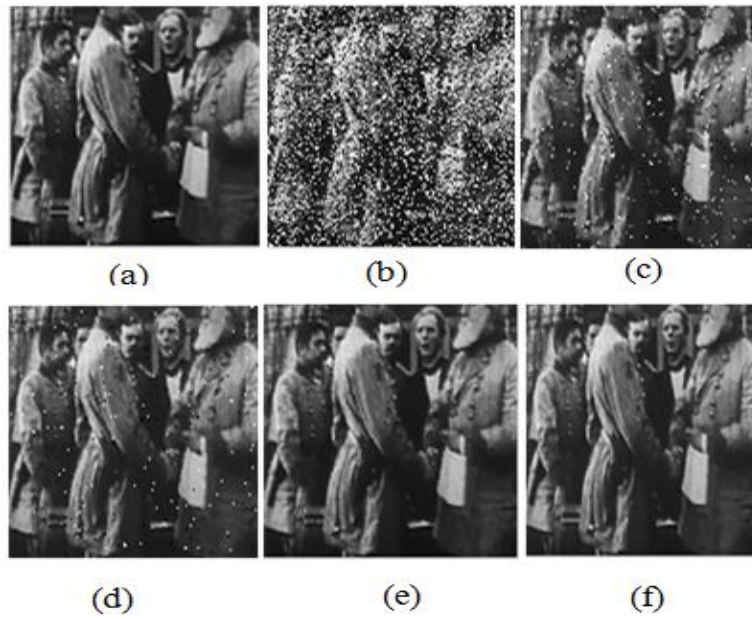


Fig.6. Results for 30% noise corrupted a selected first frame from silent film sequence. (a) Original frame, (b) Noisy frame, (c) WMF outputs, (d) SMF outputs, (e) DBMF outputs, and (f) Shows the outputs of UDBMF.

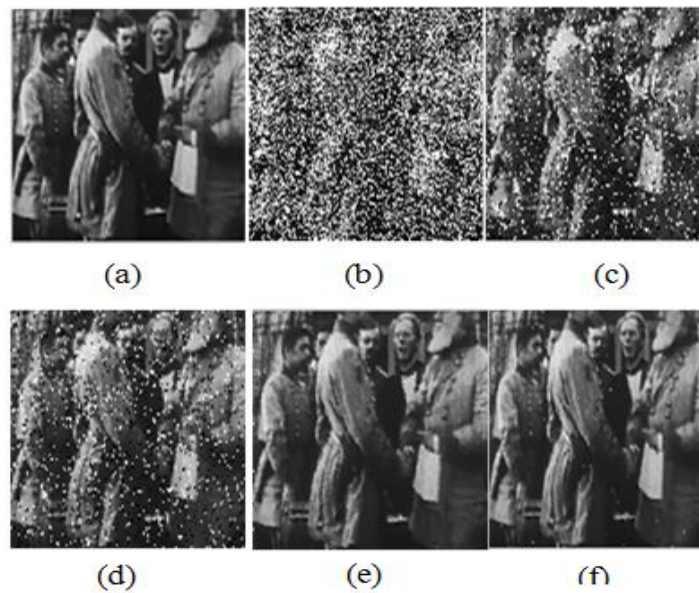


Fig.7. Results for 50% noise corrupted a selected first frame from silent film sequence. (a) Original frame, (b) Noisy frame, (c) WMF outputs, (d) SMF outputs, (e) DBMF outputs, and (f) shows the outputs of UDBMF.

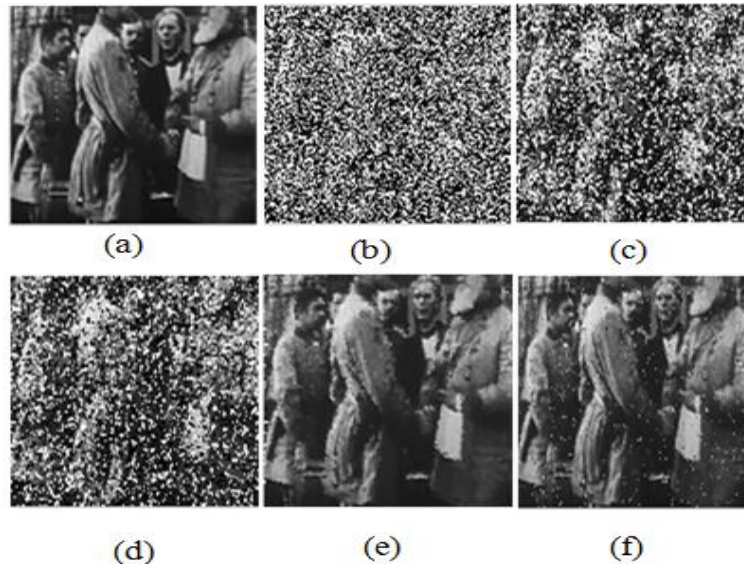


Fig.8. Results for 70% noise corrupted a selected first frame from silent film sequence. (a) Original frame, (b) Noisy frame, (c) WMF outputs, (d) SMF outputs, (e) DBMF outputs, and (f) Shows the outputs of UDBMF.

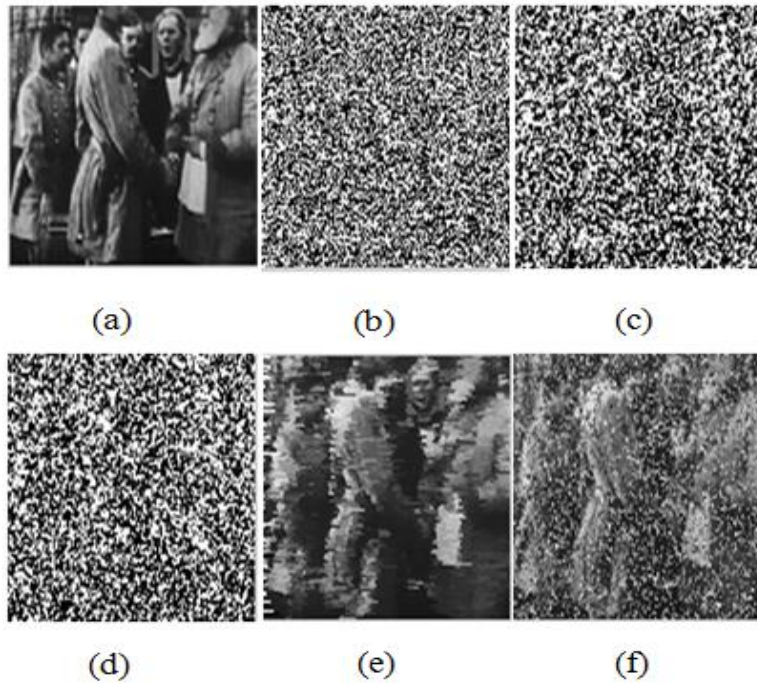
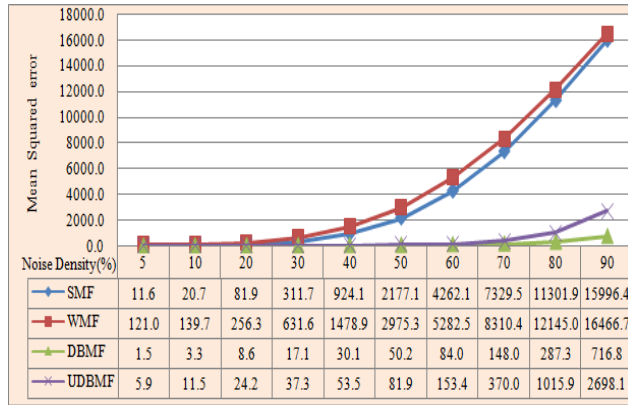
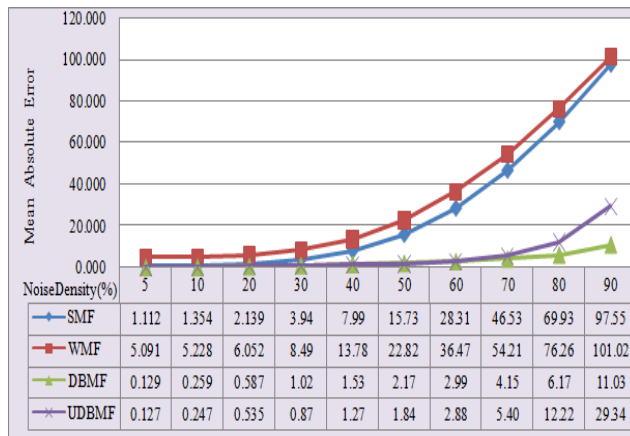


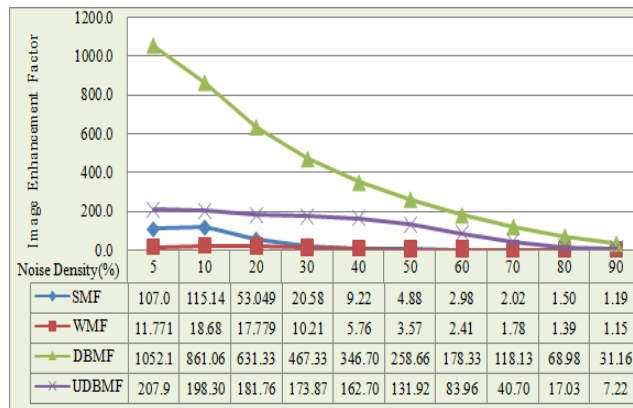
Fig.9. Results for 90% noise corrupted a selected first frame from silent film sequence. (a) Original frame, (b) Noisy frame, (c) WMF outputs, (d) SMF outputs, (e) DBMF outputs, and (f) Shows the outputs of UDBMF.



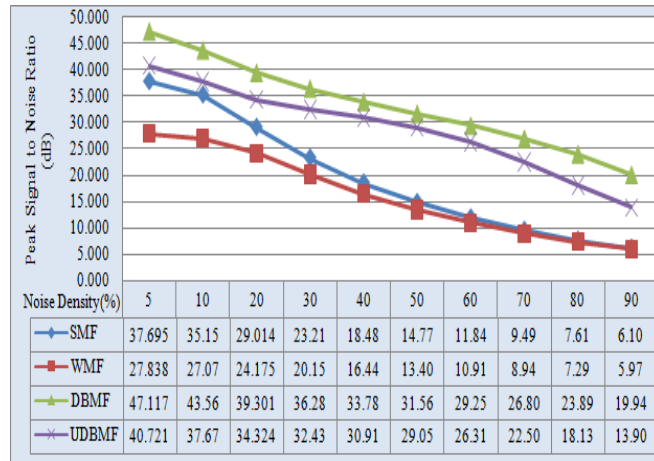
(a) MSE



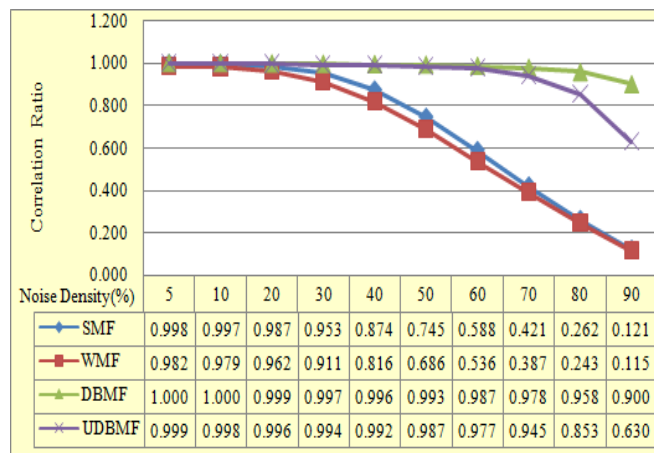
(b) MAE



(c) IEF



(d) PSNR



(e) Correlation ratio for old video sequence at different noise densities.

Fig.10. Comparison graphs and results

From Fig.10, it can be seen that (SMF, and WMF) filters didn't give better results when they are compared with (DBMF-UDBMF) filters at different noise densities from (5% to 90%).The results of DBMF and UDBMF give lower (MSE, MAE), and higher (PSNR, IEF, CORR). It can be indicated that the performance of the DBM filter is superior to the other filters for MSE, PSNR, IEF, CORR from (5% to 90%), and MAE from (70% to 90%). The UDBM filter is superior to the other filters at MAE values (5% to 60%).

7. CONCLUSION

In this work, filters have been used as a tool for removing low and high density salt and pepper noise with edge preservation in silent film. As a visual sense: For low noise density up to 30%, all filters give well visual impression in removing the salt and pepper noise. For noise densities above 40%, bad impressions are given by some existing filters such as SMF and WMF; while other filters as DBMF and UDBMF are able to suppress high density of impulse noise but they produce streaking effect for noise densities above 70%.

Related to comparable calculated parameters; DBMF and UDBMF give higher values for PSNR, IEF, and CORR. The lower values for MSE and MAE were satisfied when using DBMF and UDBMF. Both visual and quantitative results are demonstrated that the DBM, UDBM filters are effective for salt and pepper noise removal from gray video frames at high noise densities.

8. FUTURE SCOPE

Hybrid filtering approach as restoration techniques can be considered and applied in further transformed domain to incorporate with the proposed algorithm to improve the comparative study.

The comparative study can be further extended by including more noise types and more parameters like entropy and structure Similarity Index to validate the filtering performance.

References

- [1] P.Tamilselvam , M.V.Mahesh , G.Prabu, "Blotches and Impulses Removal in Colourscale Images Using Non-Linear Decision Based Algorithm," International Journal of Scientific and Research Publications, ISSN: 2250-3153, Volume 3, Issue 4, April 2013.
- [2] A.C. Bovik , Handbook of Image and Video Processing. Academic Press, 2000.

- [3] V. Pranava Jyothy, K. Padmavathi, "Removal of High Density Salt and Pepper Noise in Videos through MDBUTMF," International Journal of Recent Technology and Engineering (IJRTE) ISSN: 2277-3878, Volume-2, Issue-2, May 2013.
- [4] Mr. Vijay R. Tripathi, "Image Denoising Using Non Linear Filters," Int. J. of Computer and Communications ,Vol. 1, No. 1, March 2011.
- [5] Kaveri A.P and K.J.Amrutkar, "Median filtering Frameworks and their Application to Image Enhancement," International Journal of Application or Innovation in Engineering & Management (IJAEM), ISSN 2319 – 4847, Volume 3, Issue 3, March 2014.
- [6] Shenbagarajan Anantharajan¹, A. Siva Ganesh, V. Rajesh Kumar and C. Balasubramanian, "Image Restoration: Design of Non-linear Filter (LR)," ICTACT Journal on Image and Video Processing, Issue: 02, November 2012.
- [7] S. K. Satpathy, S. Panda, K. K. Nagwanshi, S. K. Nayak and C. Ardil, "Adaptive Non-linear Filtering Technique for Image Restoration," International Journal of Electrical and Computer Engineering 5:1 2010.
- [8] Vijayalakshmi. A, Titus.C and Lilly Beaulah.H, "Image Denoising for different noise models by various filters: A Brief Survey," International Journal of Emerging Trends & Technology in Computer Science (IJETTCS), ISSN: 2278-6856, Volume 3, Issue 6, November-December 2014.
- [9] Satyadhyam Chickerur, Aswatha Kumar, "A Biologically Inspired Filter for Image Restoration," International Journal of Recent Trends in Engineering, Vol 2, No. 2, Nov 2009.
- [10] Gajanand Gupta, "Algorithm for Image Processing Using Improved Median Filter and Comparison of Mean, Median and Improved Median Filter," International Journal of Soft Computing and Engineering (IJSCE) ISSN: 2231-2307, Volume-1, Issue-5, November 2011.
- [11] Mohammed Ghouse, M. Siddappa, " Adaptive Techniques Based High Impulsive Noise Detection of a Digital Image," Journal of Theoretical and Applied Information Technology, JATIT & LLS, ©2005 - 2011.
- [12] Rohit Verma , Jahid Ali, "A Comparative Study of Various Types of Image Noise and Efficient Noise Removal Techniques," International Journal of Advanced Research in Computer Science and Software Engineering , ISSN: 2277 128X ,3(10, pp. 617-622), October 2013.
- [13] Alasdair Mcandrew, Introduction to digital image processing with MATLAB, Course Technology a part of cengage learning, 2004.
- [14] Tom M'elange, Mike Nachtgeael, Etienne E. Kerre, "A Fuzzy Filter for the Removal of Gaussian Noise in Colour Image Sequences," ISSN:1474-1479, 2009.

- [15] C. Mythili, V. Kavitha, "Efficient Technique for Color Image Noise Reduction," 2011 IJJ: The Research Bulletin of Jordan ACM – ISWSA, ISSN: 2078-7952 (print); 2078-7960 (online), 2011.
- [16] Rafael C. Gonzalez and Richard E. Woods, Digital image processing, 2nd edition, Upper Saddle River, NJ: Prentice-Hall, 2002.
- [17] K.Suja, M.Nithya, "Detection of Random-Valued Impulse Noise In a Digital Image Using Optimal Direction Method," International Journal of VLSI and Embedded Systems (IJVES), ISSN: 2249 – 6556, Vol 04, Issue 02; March - April 2013.
- [18] Govindaraj.V, Sengottaiyan.G, "Survey of Image Denoising using Different Filters," International Journal of Science, Engineering and Technology Research (IJSETR) Volume 2, Issue 2, February 2013.
- [19] Speckle noise [Online]. Available: [http://en.wikipedia.org/wiki/ Speckle noise](http://en.wikipedia.org/wiki/Speckle_noise).
- [20] K. Somasundaram and P. Kalavathi, "Medical Image Denoising using Non-Linear Spatial Mean Filters for Edge Detection," National Conference on Signal and Image Processing (NCSIP-2012), pp.149-153,2012.
- [21] Kostadin Dabov, Alessandro Foi, Vladimir Katkovnik, and Karen Egiazarian, "Image denoising with block-matching and 3D filtering," Image Processing: Algorithms and Systems, SPIE ,Electronic Imaging ,Vol.6064 ,2006.
- [22] Inderpreet Singh, Nirvair Neeru, "Performance Comparison of Various Image Denoising Filters Under Spatial Domain," International Journal of Computer Applications (0975 – 8887) Volume 96-No.19, June 2014.
- [23] Charu Khare, Kapil Kumar Nagwanshi, "Image Restoration Technique with Non Linear Filters," International Journal of Engineering Trends and Technology (IJETT), and ISSN: 2231-5381, May to June Issue 2011.
- [24] Priyanka Kamboj and Versha Rani, "A Brief Study Of Various Noise Model and Filtering Techniques," Journal of Global Research in Computer Science, ISSN: 2229- 371X ,Volume 4, No. 4,pp.166-171, April 2013.
- [25] Anna Saro Vijendran and Bobby Lukose , "Image Restoration Using Particle Filters By Improving The Scale Of Texture With MRF," International Journal of Image Processing (IJIP) , Volume (6): Issue (5) : 2012.
- [26] Nieminen, A., P. Heinonen, and Y. Neuvo, "A new class of detail-preserving filters for image processing ," IEEE Trans. Pattern Anal. Mach. Intell, Volume 9, pp.74-90,1987.
- [27] Madhu S. Nair, K. Revathy, and Rao Tatavarti, "Removal of Salt-and Pepper noise in images: A New Decision-Based Algorithm," (Proceedings of the International Multi-Conference of Engineers and Computer Scientists 2008 Vol-I, IMECS, Hong Kong, 19-21 March 2008.

- [28] S. Balasubramanian, S. Kalishwaran, R. Muthuraj, D. Ebenezer, V. Jayaraj, "An Efficient Non-linear Cascade Filtering Algorithm for Removal of High Density Salt and Pepper Noise in Image and Video sequence," International Conference on Control, Automation, Communication and Energy Conservation -2009, 4th-6th June 2009.
- [29] S. Esakkirajan, T. Veerakumar, Adabala N. Subramanyam, and C. H. PremChand, "Removal of High Density Salt and Pepper Noise Through Modified Decision Based Unsymmetric Trimmed Median Filter," IEEE Signal Processing Letters, VOL. 18, NO. 5, MAY 2011.
- [30] A. Miranda Neto, A. Correa Victorino, I. Fantoni, D. E. Zampieri, J. V. Ferreira and D. A. Lima, "Image Processing Using Pearson's Correlation Coefficient: Applications on Autonomous Robotics," 13th International Conference on Mobile Robots and Competitions (Robotica), Lisbon: Portugal (2013).

إزالة الضوضاء ذات الكثافة العالية في الأفلام الصامتة المعرضة للخطر باستخدام المرشحات اللاخطية

إن فقد وتشويه الأفلام الطويلة في عصر الأفلام الصامتة تشكل قلقاً بالغاً في توثيق وحفظ السجل الثقافي لكثير من الأمم. لذلك كان التوجه الأول لمكتبة الكونجرس أن يدعم مشاريع بحوث أرشيفية تستعيد الأفلام الأمريكية التي أنتجت أثناء القرون التاسعة عشرة والعشرون. تعتبر إزالة الضوضاء من الإجراءات الهامة عند استعادة الفيديو التالف بحيث يمكن استرداد الفيديو الأصلي.

يهدف هذا العمل لتقديم نظرة عامة لبعض الخوارزميات التي يمكن أن تستخدم لاستعادة الفيديو التالف. هذه الخوارزميات هي المرشح المتوسط غير المضعف والمرشح المستند على المتوسط والمرشح المتوسط ذو الوزن والمرشح المتوسط العادي.

تم عمل مقارنة بين أداء كل المرشحات عند مستويات مختلفة من الضوضاء استناداً على بعض البارامترات المحسوبة مثل: خطأ المربع المتوسط، الخطأ

المُطلق المتوسط، معامل تحسين الصورة أكبر نسبة بين الإشارة إلى الشوشرة ونسبة الارتباط .
تُشير نتائج المحاكاة إلى أن مرشح المتوسط غير المضعف والمرشح المستند على المتوسط يعطيا أداءً متفوقاً مقارنةً بالمرشحات اللاخطية الأخرى عند مستويات للضوضاء في حدود تسعون بالمائة. كما أمكن الاحتفاظ بالتفاصيل الضرورية في الفيلم.

Statistical Analysis of Alzheimer 's disease Images

Mohamed M. Dessouky¹, Mohamed A. Elrashidy¹, Taha E. Taha², and Hatem M. Abdelkader³

¹ Dept. of Computer Science and Eng., Faculty of Elect., Eng., Menoufia University, EGYPT

² Department of Electronic and Electrical Communications, Faculty of Electronic Engineering, Menoufia University, EGYPT

³ Faculty of computers and information, Menoufia University, EGYPT.

(Received: 05-August-2015 – Accepted: 20- September-2015)

Abstract

Alzheimer's disease is the most common type of dementia which has no cure nor imaging test for it. Diagnosis of the Alzheimer's disease (AD) still a challenge and difficult. An early diagnosis for Alzheimer's disease is very important to delay the progression of it. This paper extract and analyze various important statistical features of MRI brain medical images to provide better analysis to discriminate among the different types of tissue and diagnose of AD. These statistical features had been used for detection of the abnormalities among different demented and non-demented MRI AD images. Also, it investigates and builds up an efficient Computer Aided Diagnosis (CAD) system for AD to assist the medical doctors to easily diagnose the disease. Statistical, structural, and textural features had been calculated for different images and classified using the SVM classifier. In addition, this paper proposes an algorithm to improve the performance of the CAD system. The performance of the CAD system based on statistical analysis and the proposed algorithm had been measured using different metric parameters. The obtained results indicate that the accuracy improved from 49% without using the proposed algorithm to 100% using the proposed algorithm.

1. Introduction

Alzheimer's disease is a degenerative brain disease and the most common cause of dementia. The most common initial symptom is a gradually

worsening ability to remember new information, planning or solving problems, completing familiar tasks at home or work, Confusion with time or place, and problems with words in speaking or writing. Alzheimer's disease is a progressive disease, which means that it gets worse over time [1, 2]. There is no cure, specific blood or imaging test for Alzheimer's disease. However, some drugs are available which may help slow the progression of Alzheimer's symptoms for a limited time. Diagnosis of the Alzheimer's disease (AD) still a challenge and difficult, especially in the early stages. The early detection will be key to prevent, slow and stop Alzheimer's disease. The last 10 years have seen a tremendous growth in research on early detection [3].

There are different previous algorithms had been proposed for early diagnosis of the AD. In [3], the Fisher discriminant ratio (FDR) and nonnegative matrix factorization (NMF) for feature selection and extraction of the most relevant features then support vector machines (SVM) classifier had been used. In [4], it presents a CAD system for early diagnosis of AD which consists of three stages: voxel selection using Mann–Whitney–Wilcoxon U-Test, feature extraction using Factor Analysis, and Linear SVM classifier had been used. In [5] an early diagnosis CAD system based on voxel selection using association rule (AR) had been presented. Then feature extraction step is defined using principal component analysis (PCA) and partial least squares (PLS) techniques and classification is performed using SVM.

Statistical analysis method is one of the important methods for feature extraction in digital images. There are different previous algorithms that depends on extracting statistical, textural, and structural features from digital images in different application [6 – 11].

This paper examine the statistical analysis of individual frames of the 3D MRI for AD based on extracting a texture and analytical features of the images database from OASIS data set [12, 13]. The rest of this paper is organized as follows: Section 2 discusses the statistical methods of feature extraction. Section 3 discussed the proposed algorithm and SVM classifier. Section 4 introduces the performance evaluation metric parameters. Section 5 presents the database, experimental results and analysis. Result discussion given in section 6 and finally the conclusion and references.

2. Statistical Feature Extraction

Feature extraction is a special form of dimensionally reduction. Feature extraction is a general term for methods for construction combination of the variables but still describes the data sufficiently accurately which may be useful for image classification. Medical images of different categories can be distinguished via their homogeneousness or feature characteristics. There are different types of features that can be extracted from the images, which are divided into statistical, structural and textural features.

2.1 Statistical Features

Statistical features are defined as the distribution of the gray level in the pixels of an image. The gray scale is a black (0) and white (255) image at any given focus of pixel. That means an image is composed of an array of pixels of varying intensity across the image, the intensity corresponding to the level of grayness from black to white at any point in the image. Statistical features is classified into first-order, second-order and high order statistics. Here, the first-order statistics will be used which describe the distribution of pixel intensities in the image through commonly used and basic metrics. Different first order statistical features had been extracted such as pixel count, Energy, Entropy, Mean Absolute Deviation (MAD), Root mean square (RMS), Standard Deviation, Skewness, Kurtosis, Variance, and Uniformity. The detailed definition and mathematical formulations of these features are given in [15-16].

2.2 Shape, Geometric and Structural Features

These features describes the shape and size of the Region of Interest (ROI). There are different features in the shape and geometric features but only the compactness1 had been measured in this work. The compactness1 definition and mathematical expression equation are given in [15 – 16].

2.3 Textural Features

The previous statistical features provide information related to the gray-level distribution of the image; but they do not provide any information about the relative position of the different gray levels over the image.

Textural features describes patterns or the spatial distribution of voxel intensities, which were calculated from respectively gray level co-occurrence (GLCM) and gray level run-length (GLRLM) texture matrices. Determining texture matrix representations requires the pixel intensity values which were therefore resampled into equally spaced bins. This discretization step not only reduces image noise, but also normalizes intensities across all patients, allowing for a direct comparison of all calculated textural features between patients [15-16].

a) Gray-Level Co-Occurrence Matrix (GLCM) based features

A GLCM is defined as $P(i, j; \delta, \alpha)$, a matrix with size $(N_g \times N_g)$ describing the second-order joint probability function of an image, where the $(i, j)^{th}$ element represents the number of times the combination of intensity levels i and j occur in two pixels in the image, that are separated by a distance of δ pixels in direction α , and N_g is the number of discrete gray level intensities. There are different Gray-Level Co-Occurrence matrix based features in the textural features had been extracted and measured in this work such as Autocorrelation, Cluster Prominence, Cluster Shade, Cluster Tendency, Dissimilarity, Homogeneity2, and Inverse Different Moment Normalized (IDMN). The definition of these features and mathematical equations are presented in details in [15 – 16].

b) Gray-Level Run-Length matrix (GLRL) based features

Run length metrics quantify gray level runs in an image. A gray level run is defined as the length in number of pixels, of consecutive pixels that have the same gray level value. In a gray level run length matrix $p(i, j | \theta)$, the (i, j) th element describes the number of times (j) a gray level (i) appears consecutively in the direction specified by θ , and N_g is the number of discrete gray level intensities. There are different Gray-Level Run-Length matrix based features in the textural features had been extracted and measured in this work such as Short Run Emphasis (SRE), Long Run Emphasis (LRE), Gray Level Non-Uniformity (GLN), Run Length Non-Uniformity (RLN), Run Percentage (RP), Low Gray Level Run Emphasis (LGLRE), High Gray Level Run Emphasis (HGLRE), Short Run Low Gray Level Emphasis (SRLGLE), Short Run High Gray Level Emphasis (SRHGLE) Long Run Low Gray Level Emphasis (LRLGLE) and Long Run High Gray Level Emphasis (LRHGLE). The definitions and mathematical formulations for all these features are given in details in [15 – 16].

3. The proposed Feature Extraction Algorithm

The proposed Algorithm steps illustrated in Fig.1 are summarized as following:

- 1- Preprocessing and Normalization for the input images.
- 2- 2D image to 1D vector array conversion.
- 3- Proposed feature Reduction and Extraction method.
- 4- Cross-validation
- 5- Feature matching or Classification process using SVM.

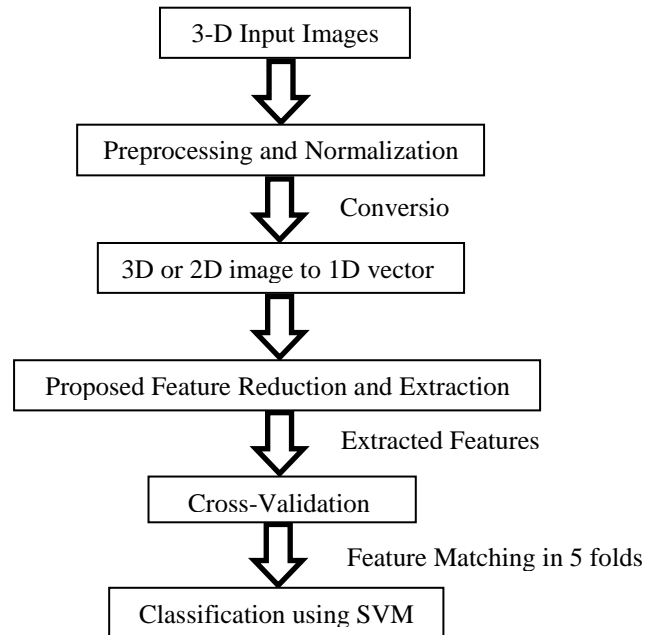


Fig. 1 The proposed Alzheimer's disease algorithm.

3.1 Preprocessing and Normalization

The MRI images must be first preprocessed and normalized by using Statistical Parametric Maps (SPM) [17] and Voxel based morphometric (VBM) [18]. VBM is preferable for large-scale neuro-morphologic change. VBM of MRI data has spatially normalizing all the images to the same space, then extracting the gray matter from the normalized images, smoothing, and finally performing a statistical analysis to find the

differences among the groups [19]. The dimensionality of the images before preprocessing was (176 X 208 X 176 = 6443008) pixels and after preprocessing and normalization steps, the dimensions of the images reduced to (121 X 145 X 121 =2122945) pixels size.

3.2 Image to vector Conversion

The 3D images converted to 2D images by taking individual frames from it then converted to 1D vector array using the mathematical reshape function [20] before applying the proposed feature reduction and extraction steps.

3.3 Proposed Feature Reduction and Extraction

Now, number of features for each image of the 15 selected images are equal to 2122945 pixels after the images had been converted from 3D to 1D and the intensity level of each pixel had been used to differentiate among the pixels. When 2D images had been used, which means that using the (x-y) plane from the 3D images. The number of pixels was 17545 pixels per image. This is very large dimensionality for each image for 2D (17545 pixels) which need very large memory size and more processing time. The proposed feature reduction method had been used to minimize this large dimensionality. This method based on removing the pixels which have the same intensity level value in all images and keeping the other features. After this step, the number of pixels at each 2D images reduced to 8236 pixels per image.

Number of pixels in each image is still very high. Feature extraction method reduces this dimensionality by extracting the most significant features and neglecting unnecessary features to increase the classifier performance. The proposed feature extraction algorithm is summarized in the following steps:

Step1: Divide the subjects into two classes, the first class includes the images of demented (patient or positive) subjects and the other contains the images of nondemented (Normal or negative) subjects.

Step2: Maximize class seperability, by calculating the mean of each class that μ_1 is the mean of first class and μ_2 is the mean of the second class.

$$\mu_1 = \frac{1}{n} * \sum_{i=1}^n x_i \quad (1)$$

Where, (n) is number of images in first class and x_i represents each image in the first class. μ_1 is repeated for each feature in the first class.

$$\mu_2 = \frac{1}{m} * \sum_{j=1}^m x_j \quad (2)$$

Where (m) is number of images in second class and x_j represents each image in the second class. μ_2 is repeated for each feature in the first class.

Step 3: Calculate standard deviation (σ_1) for the first class and (σ_2) for the second class.

$$\sigma_1 = \sqrt{\frac{\sum_{i=1}^n (x_i - \mu_1)^2}{n-1}} \quad (3)$$

Where, σ_1, x_i, n and μ_1 for the first class

$$\sigma_2 = \sqrt{\frac{\sum_{j=1}^m (y_j - \mu_2)^2}{m-1}} \quad (4)$$

Where, σ_2, x_j, m and μ_2 for the second class

Step 4: Maximize the difference between the means of the two classes by making absolute difference between the means of each feature of the two classes and divide the result by the multiplication of the standard deviation of the each feature of the two classes.

$$w = \frac{|\mu_1 - \mu_2|}{\sigma_1 * \sigma_2} \quad (5)$$

So, w is the maximum difference between the two classes, μ_1 and μ_2 are the means and σ_1 and σ_2 are the standard deviation of first and second class respectively.

Step 5: w is calculated in percent for each feature to understand how much information each feature has.

$$w_{percent} = 100 * \frac{w}{\sum_{i=1}^N w_i} \quad (6)$$

$i=1, 2, \dots, N$ features

Where, w_{percent} is calculated for each feature in all images, and w_i is the summation of all features. Then, w is sorted in descending to sort the features that have high information in the first. Selecting the higher ordered features with higher information will give higher classifier performance with smaller number of features.

3.4 Cross Validation

The cross validation step is very important to validate the performance of a learning algorithm. Cross validation is used to rate the performance of the classifier by splitting the full dataset into a training set and a testing set. The classifier is trained using the training set, and then trained model is tested by the test set. K-fold cross-validation is one of the most common method which works by dividing the dataset into K equal size subsets. For each validation, K-1 folds are trained and the remaining fold is used for testing. The procedure will loop K times. At each iteration, a different subset will be chosen as the new testing set. This ensures all the samples will be including in the testing set one time at least. If K equal to the size of the training set, so at each validation run, just one sample will be left out, hence it is called the leave-one-out cross-validation (loocv) [21, 22].

In the proposed algorithm, the database is about 15 samples and a cross-validation is done using 5-fold by randomly choosing, then training with 4 folds and test with the last one. This loop will be repeated 5 times. The results is shown in result section.

3.5 Classification using Support Vector Machine (SVM)

Support Vector Machine is used as a classifier and it has gained in popularity in recent years because of its superior performance in practical applications, mostly in the field of bioinformatics. A two-class support vector machine (SVM) classifier aims to do a hyperplane which maximizes the distance between the closest points on either side of the boundary, this distance called the margin. These points are known as the support vectors, and their role in the construction of a maximum-margin hyperplane. For more details see [23].

4. Performance Evaluation Metric Parameters

This section presents the metric parameters which will be used for measuring the performance of the classifier. To test the results the true positive, true negative, false positive and false negative which they are defined as [24, 25]:

- **True Positive (T_P):** positive (patient) samples correctly classified as positive (patient).
- **False Positive (F_P):** negative (normal) samples incorrectly classified as positive (patient).
- **True Negative (T_N):** negative (normal) samples correctly classified as negative (normal).
- **False Negative (F_N):** positive (patient) samples incorrectly classified as negative (normal).

The metric parameters that will be used to measure the performance of the proposed algorithm are [24, 25]:

- 1- **The Sensitivity (SEN):** which is also named as (Recall) or True Positive Rate (TPR) defined as:

$$SEN = \frac{T_P}{T_P + F_N} \quad (7)$$

- 2- **The Specificity (SPE):** which is also known as (True Negative Rate (TNR)) is defined as:

$$SPE = \frac{T_N}{T_N + F_P} \quad (8)$$

- 3- **The Accuracy (ACC):** which is defined as:

$$ACC = \frac{T_N + T_P}{T_P + T_N + F_P + F_N} \quad (9)$$

- 4- **Matthews correlation coefficient (MCC):** Which is calculate by:

$$MCC = \frac{(T_P * T_N) - (F_P * F_N)}{\sqrt{(T_P + F_P) * (T_P + F_N) * (T_N + F_P) * (T_N + F_N)}} \quad (10)$$

5. Statistical Feature Extraction Results

Various statistical, structural, and textural features had been examined for different 15 Alzheimer's MRI samples (5 for Normal subjects, 5 for very mild subjects, and 5 for mild subjects).

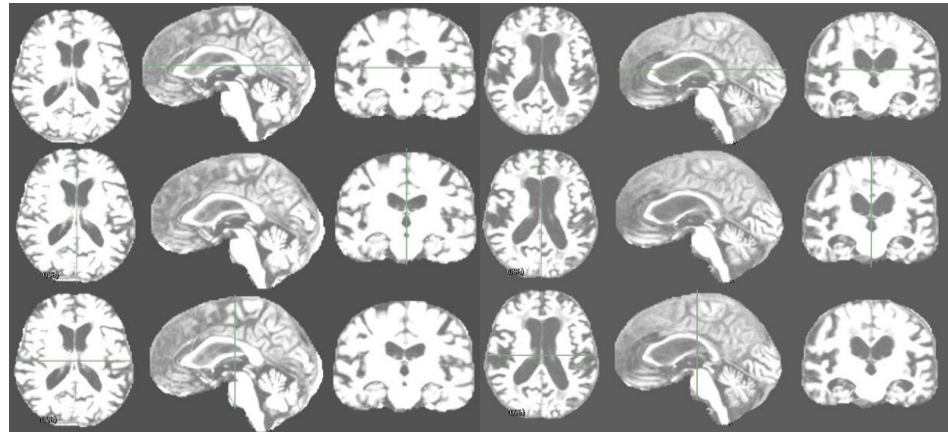
5.1 Materials and Database

The dataset that has been used for this study is the Open Access Series of Imaging Studies (OASIS) database [12, 13]. OASIS database used to determine the sequence of events that happened in the progression of AD. The database consists of a cross-sectional collection of 416 subjects aged between 33 to 96 years. The subjects include normal subjects that has no disease (no dementia) with Clinical Dementia Rating (CDR) of 0, subjects have been diagnosed with very mild AD (CDR=0.5), subjects are diagnosed with mild AD (CDR=1) and subjects with moderate AD (CDR=2).

The subjects include both men and women. More women than men have Alzheimer's disease and other dementias. Almost two-thirds of Alzheimer's are women. Based on estimates from ADAMS, among people age 71 and older, 16% of women have Alzheimer's disease and other dementias compared with 11% of men. The reason why more women than men have Alzheimer's disease is the fact that women live longer than men on average, and older age is the greatest risk factor for Alzheimer's. It is also found that there is no significant difference between men and women in the proportion who develop Alzheimer's or other dementias at any given age [1].

In this study, T1-weighted MR volumes of 5 normal subjects for 5 AD patients diagnosed with "very mild AD" and 5 AD patients diagnosed with "mild AD" are examined. All subjects are 3D MRI scans and represented in a three planes (X-Y, Y-Z, and X-Z planes) as shown in Fig. 2 which illustrates two subjects, the first one is normal subject as shown in Fig.2 (a). The second subject is for AD patients diagnosed with "mild AD" is depicted in Fig.2 (b). Each subject is represented by 3 planes or views. The first plane is represented as a line in the middle in the second and third plane, the second plane is represented as a line in the middle in the first and third plane, and the third plane is represented as a line in the middle in the second and third plane.

The subjects were randomly chosen to cover an old ages, with different ranges of MMSE. The female subjects is more than the male because of that the female is more susceptible to AD than males because the females are older age as denoted before. Table I summarizes important clinical and demographic information for each group.



(a) Non-demented (normal) subject (b) Demented (patient) subject

Fig. 2: The three planes of non-demented and demented images [10, 11].

TABLE I. Summary of subject demographics and dementia status

Group	Normal	AD (Very Mild)	AD (Mild)
No of subjects	5	5	5
Age	83-89	81-84	83-88
Clinical Dementia Rating (CDR)	0	0.5	1
Mini-Mental State Examination (MMSE)	28-30	26-27	21-28
Female/Male ratio	3/2	2/3	4/1

There are some characteristics of the 3D images as compared to 2D images presented as following [14]:

a) Amounts of data:

As compared with 2D images, 3D images represent massive amounts of data. A single X-ray CT image, for example, may be 512×512×512 bytes, while images from tissue sample microscopy may be as large as 3000×2000×500 bytes. This has huge effects on all aspects of the image processing system.

b) Properties of image geometry

Several properties arise in 3D images that did not exist in 2D images. Typical examples include the existence of knots, links, and holes. The topological characteristics of figures are extremely complex. The design

and evaluation of related algorithms like axis (surface) thinning, edge tracing, etc., becomes more difficult.

c) Diversity of density values

The physical meaning of density values is not limited to image subjects and their recordings, but will vary greatly according to the space they are contained in and the measurement (imaging) technologies used, even when the same subject is being treated. The characteristics and content of detected edges, outlines, high density areas, etc., will be very different.

5.2 Statistical features extraction for different planes of AD images

A comparison study had been presented to differentiate among normal, very mild AD, and mild AD. The statistical features are voxel count, energy, entropy, mean deviation, root mean square, standard deviation, skewness, kurtosis, variance, and uniformity. The structural feature is compactness¹. The textural features are auto-correlation, cluster prominence, cluster shade, cluster tendency, dissimilarity, homogeneity², IDMN, SRE, LRE, GLN, RLN, RP, LGLRE, HGLRE, SRLGLE, SRHGLE, LRLGLE, and LRHGLE. In this section, three different stages of AD had been examined using the previous statistical features. These stages are:

- a) Stage 1: No Impairment (normal subject):*** This stage means that the person does not suffer any memory problems. An interview with a medical professional does not show any evidence of symptoms of dementia.
- b) Stage 2: Very mild cognitive decline:*** This stage may be earliest signs of Alzheimer's disease. The person may feel as if he or she is having memory lapses, forgetting familiar words or the location of everyday objects. But no symptoms of dementia can be detected during a medical examination or by friends, family or co-workers.
- c) Stage 3: Mild cognitive decline:*** This is an early-stage Alzheimer's can be diagnosed in some, but not all, individuals with these symptoms. Friends, family or co-workers begin to notice difficulties. During a detailed medical interview, doctors may be able to detect problems in memory or concentration.

The statistical features had been measured for 3 images, each image represents one stage. The first one for the stage 1, the second image for stage 2, and the third image for stage 3.

Table II summarize the obtained results of the statistical features associated with the X-Y plane of the three images. The first column represents the statistical features for an image in stage 1 (normal), the second column shows the obtained results for an image in stage 2 (very mild AD). Also, the third column gives the results for the third stage (mild AD) image.

Table II. The statistical features for the X-Y plane of the three images in the three stages

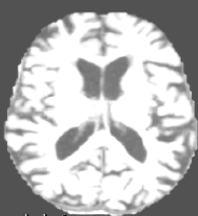
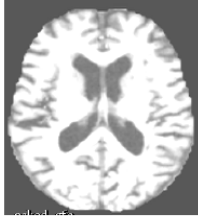
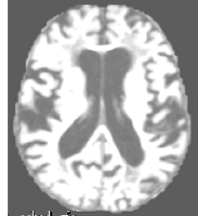
<i>Stage</i> <i>features</i>	<i>Stage 1</i> <i>Normal image</i>	<i>Stage 2</i> <i>Very Mild AD</i>	<i>Stage 3</i> <i>Mild AD</i>
<i>X-Y</i> <i>Plane</i>			
<i>Pixel Count</i>	18499	18742	18564
<i>Energy</i>	17420669043	18725791485	15889204627
<i>Entropy</i>	69676.23	71734.9	70030.08
<i>Mean Deviation</i>	364.91	352.87	399.24
<i>Root mean square</i>	970.42	999.57	925.16
<i>Standard Deviation</i>	422.01	410.9	452.72
<i>Skewness</i>	-0.12	-0.31	0.17
<i>Kurtosis</i>	-1.22	-1.06	-1.26
<i>Variance</i>	178096.58	168842.87	204956.54
<i>Uniformity</i>	272709	295568	308276
<i>Compactness 1</i>	9.29	9.31	9.3
<i>Auto-correlation</i>	4767759033.54	5528963513.54	4419420592.92
<i>Cluster Prominence</i>	1.03e+17	1.25e+17	1.01e+17
<i>Cluster Shade</i>	4.27e+13	5.09e+13	4.06e+13
<i>Cluster Tendency</i>	18777303760	21772844218.4	17454124968.5
<i>Dissimilarity</i>	624751.46	620013.77	655053.69
<i>Homogeneity 2</i>	78.55	76.4	79.9
<i>IDMN (Inverse</i> <i>Difference Moment)</i>	5628.69	5690	5647.62
<i>SRE</i>	0.304	0.3041	0.3039
<i>LRE</i>	1.05	1.08	1.09
<i>GLN</i>	4.25	4.52	4.55
<i>RLN</i>	5254.53	5325.23	5249.68
<i>RP</i>	0.292	0.292	0.291
<i>LGLRE</i>	3.25e-05	3.05e-05	3.33e-05
<i>HGLRE</i>	260828.21	297312.58	247112.51
<i>SRLGLE</i>	2.84e-05	2.75e-05	2.06e-05
<i>SRHGLE</i>	259388.14	296018.04	246317.74
<i>LRGLE</i>	0.0009	0.0008	0.0023
<i>LRHGLE</i>	333478.01	345511.46	294586.73

Table III gives the obtained statistical features for the X-Z plane of the three different stages (normal stage, very mild AD stage and mild AD stage respectively).

Table III. The statistical features for the X-Z plane of the three images in the three stages

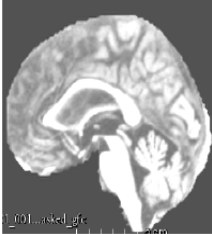

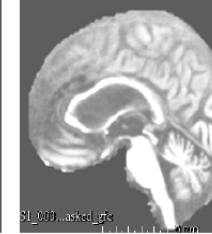
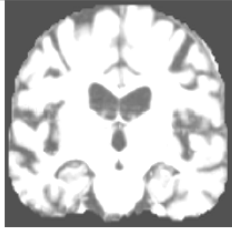
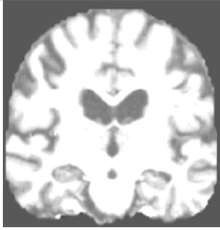
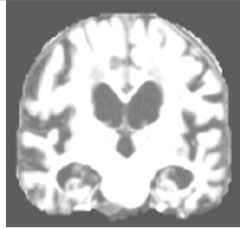
Stage features	Stage 1 Normal image	Stage 2 Very Mild AD	Stage 3 Mild AD
X-Z Plane			
Pixel Count	16656	16435	16415
Energy	8752863721	9061132322	9900535633
Entropy	64888.4	66430.36	62694.37
Mean Deviation	252.92	218.01	266.96
Root mean square	724.92	742.52	776.62
Standard Deviation	324.06	282.42	331.62
Skewness	0.84	0.93	0.67
Kurtosis	0.454	0.96	-0.06
Variance	105013.754	79762.9	109971.54
Uniformity	296934	329571	266421
Compactness 1	8.943	8.91	8.91
Auto-correlation	2566834737.15	1931502138.62	2193503743.85
Cluster Prominence	3.98e+16	2.27e+16	3.103e+16
Cluster Shade	1.884e+13	1.23e+13	1.545e+13
Cluster Tendency	10118127383.1	7566447191.7	8640481294.9
Dissimilarity	480067.92	446495.15	483583.08
Homogeneity 2	83.17	78.94	81.21
IDMN (Inverse Difference Moment)	5053.85	4991.46	4985.385
SRE	0.3031	0.303	0.303
LRE	2.92	3.08	3.11
GLN	5.04	5.59	4.63
RLN	4644.91	4548.23	4593.27
RP	0.288	0.286	0.29
LGLRE	3.44e-05	3.58e-05	3.61e-05
HGLRE	160713.4	122824.8	139816.39
SRLGLE	3.16e-05	1.32e-05	1.51e-05
SRHGLE	159365.85	121726.85	138881.26
LRLGLE	0.0015	0.0077	0.025
LRHGLE	539404.85	445467.04	450100.555

Table IV presents the statistical features for the Y-Z plan. A three images had been used. Each image used for one stage of normal, very mild AD and mild AD. Each image is represented in one column.

Table IV. The statistical features for the Y-Z plan of the three images in the three stages

Stage features	Stage 1 Normal image	Stage 2 Very Mild AD	Stage 3 Mild AD
Y-Z Plane			
<i>Pixel Count</i>	14030	13953	14048
<i>Energy</i>	14446103350	14381583696	15632037434
<i>Entropy</i>	48376.72	48579.4	45927.71
<i>Mean Deviation</i>	354.48	333.06	414.19
<i>Root mean square</i>	1014.72	1015.24	1054.87
<i>Standard Deviation</i>	410.33	387.39	472.51
<i>Skewness</i>	-0.36	-0.31	-0.12
<i>Kurtosis</i>	-1.11	-0.9	-1.25
<i>Variance</i>	168369.6	150068.04	223268.26
<i>Uniformity</i>	174132	175923	151506
<i>Compactness 1</i>	8.46	8.44	8.46
<i>Auto-correlation</i>	3888580907.92	3563074796.15	4316321743.46
<i>Cluster Prominence</i>	8.4e+16	6.98e+16	1.13e+17
<i>Cluster Shade</i>	3.51e+13	3.06e+13	4.29e+13
<i>Cluster Tendency</i>	15393371294.4	14097959365.6	17157369335.2
<i>Dissimilarity</i>	460648.69	452500.54	519766.23
<i>Homogeneity 2</i>	58.97	57.64	58.3
<i>IDMN (Inverse Difference Moment)</i>	4262	4237.38	4266
<i>SRE</i>	0.304	0.3039	0.3041
<i>LRE</i>	0.63	0.61	0.6
<i>GLN</i>	3.56	3.62	3.12
<i>RLN</i>	3999.23	3971.4	4025.92
<i>RP</i>	0.293	0.293	0.295
<i>LGLRE</i>	4.02e-05	3.98e-05	3.98e-05
<i>HGLRE</i>	277917.94	256991.78	311989.9
<i>SRLGLE</i>	2.63e-05	2.21e-05	2.7e-05
<i>SRHGLE</i>	276551.55	255617.15	310590.86
<i>LRLGLE</i>	0.0005	0.00054	0.0007
<i>LRHGLE</i>	302098.35	288970.12	335845.49

6. Experimental Results

In this section, a three different experiments had been presented. The first, the statistical features had been fed out to the SVM. The second experiment, applying the extracted statistical features to the proposed algorithm before the SVM. The last experiment, apply the proposed algorithm on (X-Y) plane for intensity level of the pixels before SVM.

6.1 Metric parameters evaluation results for the Statistical features

Classification for the statistical features is examined using SVM classifier to calculate the metric parameters. These statistical features had been used as the input to the classifier as shown in Fig.3.

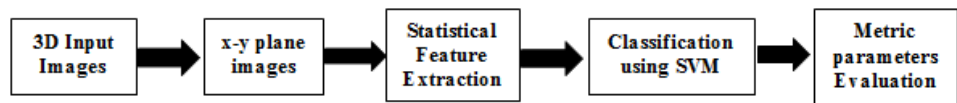


Fig. 3 classifying statistical features from one plane

The features of the X-Y plane had been used for 15 images to classify these images to normal or patient. X-Y plane had been chosen because the values of the features have some difference among classes than the other planes. Figure 4 and Table V give the obtained values of metric parameters of the classifier for the statistical features.

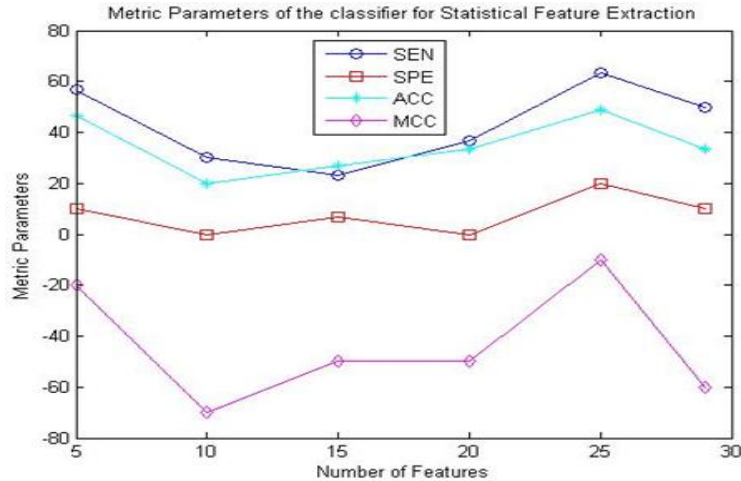


Fig. 4 The metric parameters of the classifier using the statistical features

The features of the X-Y plane had been used for 15 images to classify these images to normal or patient. X-Y plane had been chosen because the values of the features have some difference among classes than the other planes. Figure 4 and Table V give the obtained values of metric parameters of the classifier for the statistical features.

Table V. The metric parameters of the classifier using the statistical features

No. of Features \ Metric Parameters	5	10	15	20	25	29
Sensitivity (SEN)	56.7 %	30 %	23.3 %	36.7 %	63.3 %	50 %
Specificity (SPE)	10 %	0 %	6.7 %	0 %	20 %	10 %
Accuracy (ACC)	46.7 %	20 %	26.7 %	33.3 %	48.7 %	33.3 %
Matthews's correlation coefficient (MCC)	-20 %	-0 %	-50 %	-50 %	-10 %	-60 %

The obtained results depicted in Fig. 4 conclude that the accuracy (ACC) has a maximum value about 49%.

6.2 Metric parameters evaluation results for the proposed algorithm using the statistical features

The proposed Algorithm had been applied as a preprocessing step before classification for these features as illustrated in Fig.5.

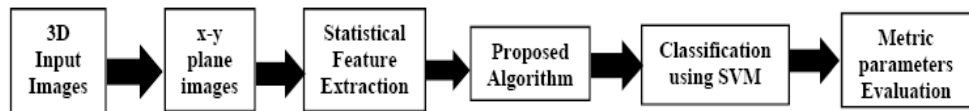


Fig. 5 statistical feature extraction using the proposed algorithm

The proposed algorithm is applied to the statistical features. A 15 images had been used to classify each one into normal or patient classes using the SVM classifier. Figure 6 and Table VI present the calculated values of

metric parameters of the classifier for the statistical features and the proposed algorithm.

Table VI. The metric parameters of the classifier using the statistical features and proposed Algorithm

No. of Features \ Metric Parameters	5	10	15	20	25	29
Sensitivity (SEN)	70 %	73.3 %	40 %	20 %	60 %	60 %
Specificity (SPE)	10 %	30 %	10 %	10 %	10 %	10 %
Accuracy (ACC)	60 %	60 %	26.7 %	26.7 %	40 %	40 %
Matthews's correlation coefficient (MCC)	0 %	10 %	-50 %	-50 %	-30 %	-30 %

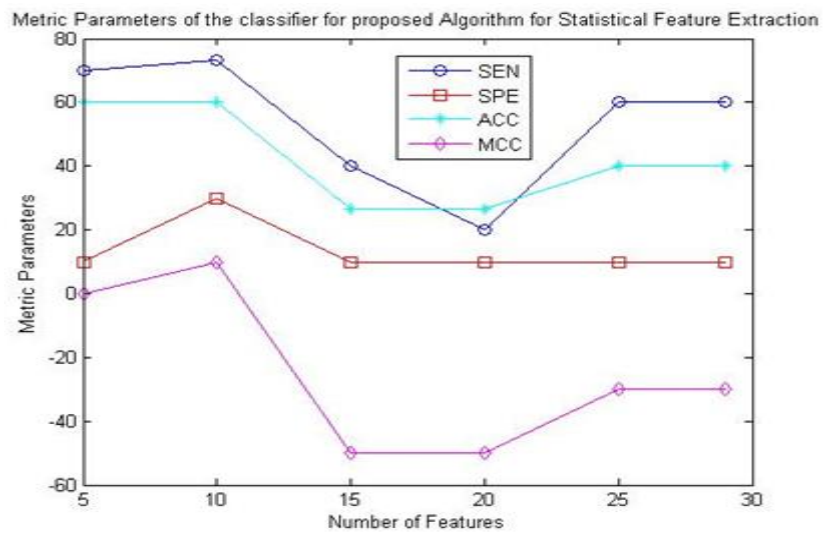


Fig.6 The metric parameters of the classifier using the statistical features and proposed Algorithm

6.3 Metric parameters evaluation results for the proposed algorithm using intensity (gray) level of pixels

The proposed Algorithm had been applied to the 2D images by using the intensity (gray) level. Each image dimensionality was 121X145 pixels (17545 pixels). Next, the proposed feature reduction step had been applied which reduces the number of pixels to 8236 pixels. Then, the proposed feature extraction step had been applied to sort the features. Next, cross validation is applied to divide the 15 images into 5 folds. Finally, the loop of five times had been applied to train the SVM with 4 folds and test with the fifth. Figure 7 and Table VII illustrate the measured values of metric parameters of the classifier using the proposed algorithm for 2D images using intensity (gray) level of the pixels.

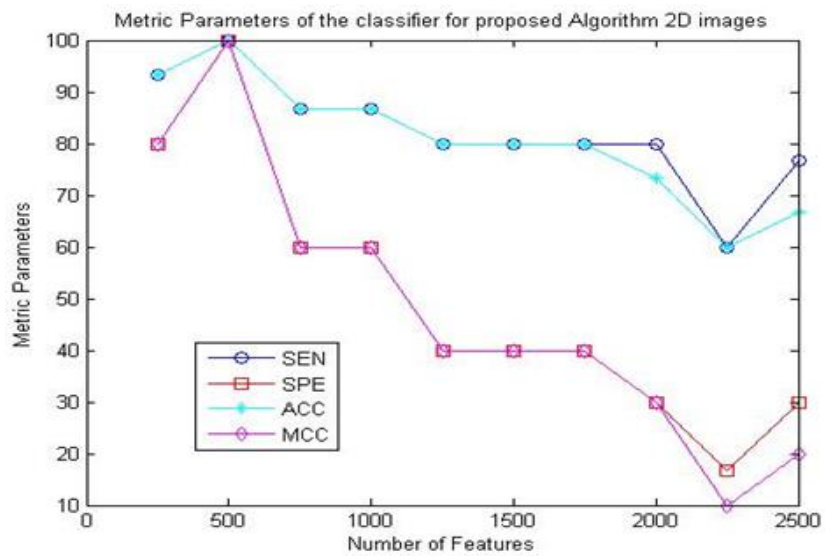


Fig. 7 The metric parameters of the classifier using the proposed Algorithm on 2D intensity (gray) level of pixels

The obtained results presented in Table VII and illustrated in Fig.7 indicate that the values of the accuracy (ACC) improved to 100% using the proposed algorithm for the intensity (gray) level of the pixels using number of extracted features equal to 500 features. A comparison study had been done among previous works and the proposed algorithm given in this paper. This comparison study had been presented in Table VIII.

Table VII. The metric parameters of the classifier using the proposed Algorithm on 2D intensity (gray) level of pixels

No. of Features \ Metric Parameters	250	500	750	1000	1250	1500	1750	2000	2250	2500
Sensitivity (SEN)	93.3 %	100 %	86.7 %	86.7 %	80 %	80 %	80 %	80 %	60 %	76.7 %
Specificity (SPE)	80 %	100 %	60 %	60 %	40 %	40 %	40 %	30 %	16.7 %	30 %
Accuracy (ACC)	93.3 %	100 %	86.7 %	86.7 %	80 %	80 %	80 %	73.4 %	60 %	66.7 %
Matthews's correlation coefficient (MCC)	80 %	100 %	60 %	60 %	40 %	40 %	40 %	30 %	10 %	20 %

Table VIII. Comparison study among previous work and proposed algorithm.

Metric Parameters \ Algorithm	ACC	SEN	SPE	MCC	No. of Features
Ref. [3]	91.4 %	90.6 %	92.3 %	---	---
Ref. [4]	93.7 %	95.1 %	92.7 %	---	3000
Proposed Algorithm	100 %	100 %	100 %	100 %	500

7. Result discussion

The obtained results given in tables II, III and IV, present the different extracted features from normal, very mild and mild MRI images. The features had been extracted from the images planes (X-Y, X-Z, and Y-Z). The number of pixels used for calculation was very high this leads to large values for each feature as indicated in these tables. Studying the obtained results for the three different types of the statistical, structural and textural features indicate that the values of these different extracted features for normal, very mild and mild stages may help the medical doctors to diagnose the Alzheimer's disease. The SVM classifier had been used to classify the images into two classes (normal and patient) and the evaluated accuracy value is about 49%. The proposed algorithm had been applied to the statistical features then performing the classification. In this case, the results of the accuracy value improved to 60%. The proposed algorithm

had been applied to the 2D images with only intensity level of the images and the measured value of the accuracy improved to 100% using number of extracted features equal to 500 features. A comparison study had been done among previous works and the proposed algorithm. The obtained results given in Table VIII indicates that, in [3] the accuracy value is about 92% while in [4] the value of the accuracy is about 94% using 3000 features. The accuracy value using the proposed algorithm improved to 100%.

8. Conclusion

The statistical analysis of MRI images of AD had been presented in this paper. Different important statistical, structural and textural features that had been extracted from different AD MRI images (normal, very mild AD and mild AD). The 3D images had been analyzed in three planes and the features had been extracted from each plane. These extracted features may help to diagnosis the Alzheimer's disease. The classification of these extracted features had been done using SVM. The proposed algorithm applied to these extracted features before classification. The proposed algorithm had been applied to the 2D images for the intensity level. The calculated metric parameters values were 100% with number of extracted features equal to 500 features. The trends of this paper for the Alzheimer's disease is to build up a Computer Aided Diagnosis (CAD) system to assist the medical doctors to easily diagnosis AD without the need to ask about the symptoms, do physical examinations, check neurological functions, or ask about blood tests and urine samples

References

- [1] Alzheimer's Association. 2015 Alzheimer's disease Facts and Figures. Alzheimer's & Dementia 2015.
- [2] A. Wimo and M. Prince, "World Alzheimer Report 2010: The global economic impact of dementia," 2010.
- [3] P. Padilla, M. López, J. Górriz, J. Ramírez, D. Salas-González, I. Álvarez, and The Alzheimer's Disease Neuroimaging Initiative, "NMF-SVM Based CAD Tool Applied to Functional Brain Images for the Diagnosis of Alzheimer's Disease", IEEE TRANSACTIONS ON MEDICAL IMAGING, VOL. 31, NO. 2, 2012, pp. 207-216.

- [4] F.J. Martinez-Murcia , J.M. Gorriz , J. Ramirez , C.G. Puntonet , D. Salas-Gonzalez or the Alzheimer’s Disease Neuroimaging Initiative, “Computer Aided Diagnosis tool for Alzheimer’s Disease based on Mann–Whitney–Wilcoxon U-Test”, *Expert Systems with Applications* 39 (2012) 9676–9685.
- [5] R. Chaves, J. Ramirez a, J.M. Gorriz, C.G. Puntonet , Alzheimer’s Disease Neuroimaging Initiative, “Association rule-based feature selection method for Alzheimer’s disease diagnosis”, *Expert Systems with Applications* , 2012.
- [6] M. Sharma, R. Dubey², Sujata, and S. Gupta, “Feature Extraction of Mammograms”, *International Journal of Advanced Computer Research*, Vol. 2, No. 3, Issue 5, 2012, pp. 201 – 209.
- [7] P. Telagarapu, and S. Poonguzhali, “Analysis of Contourlet Texture Feature Extraction to Classify the Benign and Malignant Tumors from Breast Ultrasound Images”, *International Journal of Engineering and Technology*, Vol 6 No 1, 2014, pp. 239 – 305.
- [8] S. Karthikeyan, and N. Rengarajan, “Analysis of Gray Levels for Retinal Image Classification”, *Australian Journal of Basic and Applied Sciences*, Vol. 7, No.13, 2013, pp. 58-65.
- [9] N. Zulpe1 and V. Pawar, “GLCM Textural Features for Brain Tumor Classification”, *IJCSI International Journal of Computer Science Issues*, Vol. 9, Issue 3, No 3, 2012, pp. 354 – 359.
- [10] [10] A. Simpson, R. Do, E. Parada, M. Miga, and W. Jarnagin, “Texture Feature Analysis for Prediction of Postoperative Liver Failure Prior to Surgery”, *SPIE Medical Imaging conference*, 2014.
- [11] S. Manikandan, V. Rajamani, and N. Murugan, “Analysis of Ultra Sound Kidney Image Features for Image Retrieval by Gray Level Co-Occurrence Matrices”, *Lecture Notes on Software Engineering*, Vol. 1, No. 1, 2013, pp. 94 – 97.
- [12] OASIS Database: <http://www.oasis-brains.org/>
- [13] D. Marcus, T. Wang, J. Parker, J. Csernansky, J. Morris and R. Buckner, “Open access series of imaging studies (OASIS): cross-sectional MRI data in young, middle aged, nondemented, and demented older adults,” *Journal of Cognitive Neuroscience*, vol. 19, no. 9, pp. 1498–1507, 2007.
- [14] J. Toriwaki, H. Yoshida, “Fundamentals of Three-Dimensional Digital Image Processing”, Springer-Verlag London Limited, 2009.
- [15] HeterogeneityCAD module with 3D slicer:
<http://wiki.slicer.org/slicerWiki/index.php/Documentation/Nightly/Modules/HeterogeneityCAD>
- [16] Hugo J. Aerts, Emmanuel R. Velazquez, and Ralph T. Leijenaar, “Decoding tumor phenotype by noninvasive imaging using a quantitative radiomics approach”, *Nature Communications*, *Nature Communications* 5: Article number: 4006; 2014.

- [17] SPM8. Retrieved from <http://www.fil.ion.ucl.ac.uk/spm/>
- [18] VBM8. Retrieved from <http://dbm.neuro.uni-jena.de/vbm/>
- [19] John Ashburner and Karl J. Friston, "Voxel-Based Morphometry—The Methods", *NeuroImage* 11, 805–821, 2000.
- [20] MATLAB Reshape Function. Retrieved from <http://www.mathworks.com/help/matlab/ref/reshape.html>
- [21] Chia-Yueh C. CHU, "Pattern recognition and machine learning for magnetic resonance images with kernel methods", thesis submitted for the degree of Doctor of Philosophy, University College London, 2009.
- [22] Payam Refaeilzadeh, Lei Tang and Huan Liu. "Cross Validation. In *Encyclopedia of Database Systems*", Springer, 2009.
- [23] C. BURGESS, "A Tutorial on Support Vector Machines for Pattern Recognition", *Data Mining and Knowledge Discovery*, 2, 121–167 (1998).
- [24] U. Okeh and C. Okoro, "Evaluating Measures of Indicators of Diagnostic Test Performance: Fundamental Meanings and Formulas", *Journal of Biometrics Biostatistics*, vol. 3, Issue 1, 2012.
- [25] M. Bekkar, H. Djema, and T. Alitouche, "Evaluation Measures for Models Assessment over Imbalanced Data Sets", *Journal of Information Engineering and Applications*, Vol.3, No.10, pp. 27 – 38, 2013
- =====

ملخص البحث

التحليل الإحصائي لصور مرض الزهايمر

يعتبر مرض الزهايمر من أشهر أنواع الخرف التي لا يوجد لها علاج ولا يوجد لها طريقة ثابتة لإختراره وإكتشافه باستخدام الصور او بأي طريقة اخرى. يعتبر أكبر التحديات الموجودة في مرض الزهايمر هي صعوبة تشخيصه وخاصة في المراحل الأولية من المرض حيث يساعد اكتشافه في مراحله الأولى على تأخير ظهور أعراضه عن طريق تعاطي العقاقير المناسبة للمريض. يعمل هذا البحث على استخلاص وتحليل الخصائص الإحصائية المهمة والمميزة لصور الرنين المغناطيسي الطبية الخاصة بالمخ وذلك بإستخلاصها من صور لاشخاص في

مراحل مختلفة من المرض (عادي، خفيف جدا وخفيف) وذلك لإعطاء تحليل افضل للتفرقة بين الأنواع المختلفة من الأنسجة ولتشخيص مرض الزهايمر. وهذه الخصائص المستخرجة تم استخدامها للكشف على الاختلافات بين الحالات المريضة والسليمة عن طريق تحليل الصور ثلاثية الابعاد في ثلاث مستويات ومحاور وتم استخلاص هذه الميزات من كل مستوى. ويعتمد هذا البحث على بناء نظام تشخيصي كفاء لمرض الزهايمر لمساعدة الأطباء على سرعة وسهولة تشخيص المرض.

في هذا البحث، تم استخلاص العديد من الخصائص المميزة وتم حسابها مثل الخصائص الإحصائية والهيكلية والتكوينية للعديد من الصور والحالات المختلفة وتم تصنيف الحالات باستخدام SVM الذي يعتبر من أشهر وأهم المصنفات. بالإضافة الى ذلك، تقترح هذه الورقة العلمية اسلوب جديد لتحسين أداء النظام التشخيصي. حيث تم قياس أداء وجودة النظام المقترح القائم على استخلاص الخصائص المختلفة للصور باستخدام حساب مجموعة معاملات قياس مختلفة منها دقة أداء المصنف. وتشير النتائج التي تم الحصول عليها أن الدقة تحسنت من 49 % دون استخدام الطريقة المقترحة إلى 100 % باستخدام الطريقة المقترحة. إتجاهات هذه الورقة العلمية لمرض الزهايمر هو بناء نظام تشخيصي بمساعدة الحاسوب لمساعدة الأطباء على سهولة تشخيص مرض الزهايمر دون الحاجة لسؤال المريض عن الأعراض، والقيام الفحوصات الطبية، والتحقق من الوظائف العصبية، أو عمل اختبارات وتحاليل الدم و فحص عينات البول.

Advanced Relay Station for LTE-A Downlink Physical Layer

Mohamed G. El-Mashed and S. El-Rabaie

Department of Electronics and Electrical Communications, Faculty of Elect., Eng.,
Menoufia University, Menouf 32952, Egypt.

(Received: 14-September-2015 – Accepted: 01-October-2015)

Abstract

Relay Station (RS) enhance the performance of cellular system at cell edge. It also extends the transmission to areas outside the coverage. This paper studies the transmission through direct and relay link between Base Station (BS) and User Equipment (UE). This paper also proposes RS based Orthogonal Space-Time Block Codes (OSTBCs) for fourth generation cellular system (i.e. LTE-A). The received signals at UEs for different transmission scenarios are mathematically derived and analyzed. We compare the performance of LTE-A Downlink Physical Layer in the case of direct link, relay link and relay link based OSTBCs. The SER performance for LTE-A with three transmission scenarios is calculated for a certain range of SNRs. Results show that the transmission link that uses RS based OSTBCs gives better performance than direct link and relay link.

1. Introduction

The requirements of IMT-Advanced systems are high data rate, extended coverage areas, efficient spectrum and low latency [1-4]. A 3GPP started its LTE-A standardization to achieve these requirements. The performance at the cell edge is becoming necessary in cellular systems that employ higher bandwidths and use higher carrier frequencies at the same transmit power. One solution to increase coverage and reduce the SER values at UEs is using RS to transmit data between the BS and UE through multi hop communication [5-11]. RS also increases the data rate, reliability and link quality [12-14]. Cooperative diversity capitalizes on transmissions

from antennas at different nodes in order to provide spatial diversity by using an Orthogonal Space-Time Block Codes (OSTBCs). An OSTBC can provide full diversity order and high performance at very low decoding complexity [15-17]. The columns vectors in the coding matrix of an OSTBC are orthogonal. It improves the performance of a wireless network by overcoming the problems of attenuation and fading effects due to transmission over wireless channels. It has been employed in dual-hop relaying system as in [20].

So, we propose the RS based OSTBCs for the LTE-A downlink physical layer. We use an OSTBC with rate-3/4 for 4 transmit antennas. We illustrate mathematically different transmission scenarios for LTE-A. The received signals expressions have been derived under various scenarios of transmission links. The scenarios are direct link, relay link and proposed relay link based OSTBCs. The performance of system is evaluated by calculating the SER values for a certain range of SNRs. This paper is organized into four sections. Section 2, gives a brief review of the LTE-A downlink physical layer. The transmission scenarios for LTE-A downlink physical layer and proposed scheme are illustrated in Section 3. The results are given in Section 4. Finally, concluding remarks are given in Section 5.

2. LTE-A Downlink Physical Layer

The BS is responsible for scheduling the transmission between different UEs and RSs to maintain a reliable radio link between each UE and the BS by dynamically adapting the transmission parameters [13]. First, the user data at transmitter as shown in Fig. 1(a), is generated depending on the previous Acknowledgement (ACK) signal. If the previous user receives negative ACK, the stored data is retransmitted using a Hybrid Automatic Repeat request (HARQ) scheme. Based on UEs ACK feedback, a scheduling algorithm allocates RBs to UEs and sets an appropriate coding rate depending on the channel state as in Fig. 1(a). Then, a Cyclic Redundancy Check (CRC) is added to the data. The data of each user is independently encoded using a turbo encoder with Quadrature Permutation Polynomial (QPP) based interleaving [14-15]. Each block of coded bits is then interleaved and rate matched with a target rate

depending on the received Channel Quality Indicator (CQI) user feedback [16].

Second, the data modulation maps the encoded data to complex modulation symbols. Depending on the CQI, a modulation scheme is selected for the corresponding RB [17-18]. After modulation step, the data are mapped to four transmit antennas. This antenna mapping depends on the Rank Indicator (RI) feedback and provides different multi-antenna schemes. After that, the optimum pre-coding matrix is selected depending on the Pre-coding Control Information (PCI) that is fed back from the UE to the BS and then applied to the OFDM transmitted signal [13]. Finally, the symbols to be transmitted on each antenna are mapped to the resource elements. The downlink reference and synchronization symbols are also inserted into the OFDM time-frequency grid [20].

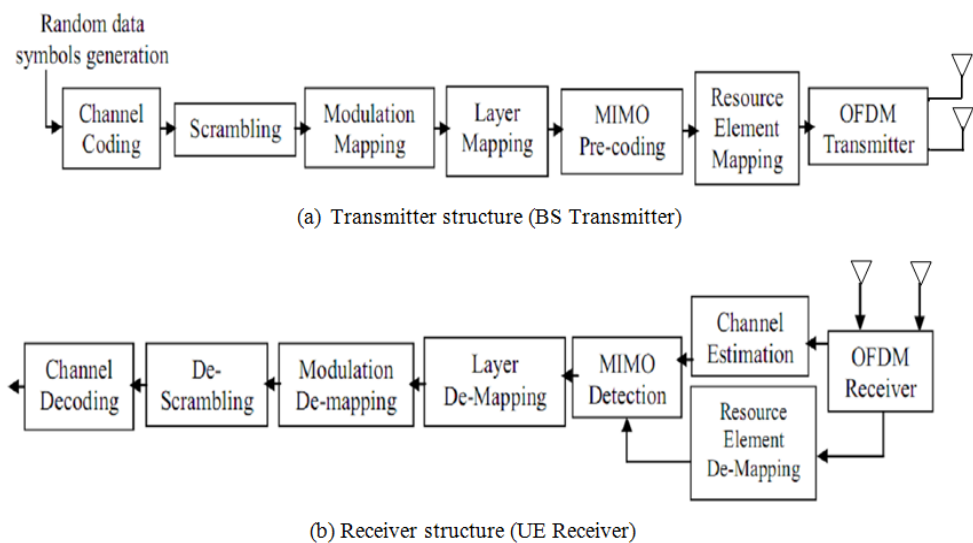


Fig. 1: LTE-A downlink physical layer structure

At receiver, UEs receive the signal through their multiple antennas as shown in Fig 1(b). Each UE processes OFDM signals from the different receive antennas. Cyclic prefix is removed from the received OFDM symbol in the time domain, and then an N-FFT is applied to convert OFDM symbols into the frequency domain through the process of OFDM demodulation. In MIMO-OFDM systems, Channel State Information (CSI) is necessary at the UE receiver to detect the received signal and to

perform diversity combining [13]. The estimation of the channel is performed using the Minimum Mean Squared Error (MMSE) technique [22]. After that, the complex transmitted symbols are de-mapped into the corresponding code words through the process of layer de-mapping. Finally, the UE makes the inverse process of scrambling and channel coding, which are descrambling and channel decoding as in Fig. 1(b). The received SER and the channel capacity are evaluated for a certain range of SNRs.

3. The Transmission Scenarios for LTE-A Downlink Physical Layer

(a) Transmission through Direct Link (BS to UE):

Each BS transmits N data symbols to the UE as shown in Fig. 2(a). Let $x(n)=[x_1(n), x_2(n), \dots, x_K(n)]$ be the data symbols transmitted by BS during the n^{th} symbol period, P_{BS} is the transmitted power by BS, and $S_k(t)$ is the OFDM transmitted waveform.

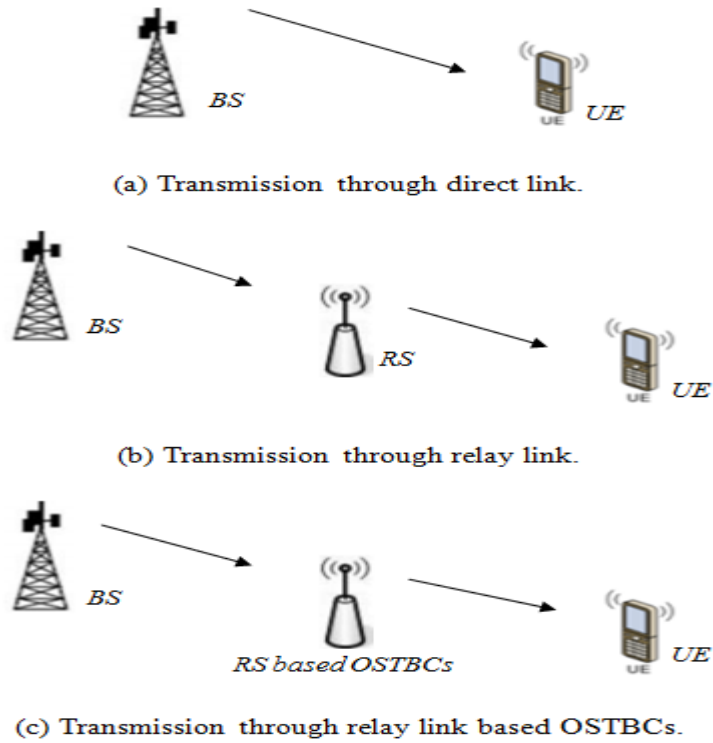


Fig. 2 Transmission scenarios for LTE-A

The received signal at the UE through direct link in the presence of Additive White Gaussian Noise (AWGN) can be expressed as:

$$y_d(t) = \sum_{n=1}^N \sum_{k=1}^K h_{km} (\sqrt{P_{BS}}) x_k(n) S_k(t - nT - \tau_k) + n(t) \quad (1)$$

Where, T is symbol period, $n_I(t)$ is the AWGN, h_{km} is the complex channel co-efficient from BS to UE and τ_k is the transmission delay. The MMSE is performed to obtain the estimated data symbols.

(b) Transmission through Relay Link:

The system is mathematically analyzed with two phases:

First, Transmission from BS to RS: Each BS broadcasts the N data symbols to the RS as shown in Fig. 2(b). The received signal at RS during the n^{th} symbol period is given by:

$$y_1(t) = \gamma \sum_{n=1}^N \sum_{k=1}^K h_{kl} (\sqrt{P_{BS}}) x_k(n) S_k(t - nT - \tau_{kl}) + \gamma n_1(t) \quad (2)$$

where T is symbol period, $n_1(t)$ is the AWGN, h_{kl} is the complex channel co-efficient from BS to RS and τ_{kl} is the transmission delay. For AF, amplification is performed at each RS to forward the received signals at the UEs. The amplification factor is given by [25]:

$$\gamma \leq \sqrt{\frac{P_{BS}}{h_{kl} P_{BS} + n(t)}} \quad (3)$$

Where, P_{BS} is the Power transmitted by BS.

Second, Transmission from RS to UE: RS forward the detected data to the UE as shown in Fig. 2(b). The received signal at UE during the n^{th} symbol period is given by:

$$y_2(t) = \sum_{n=1}^N \sum_{k=1}^K \sum_{l=1}^L g_{lm} (\sqrt{P_{BS_k}}) \hat{x}(n) S_k(t - nT - \tau_l) + n_2(t) \quad (4)$$

Where, T is symbol period, $n_2(t)$ is the AWGN, g_{lm} is the complex channel co-efficient from RS to UE and τ_l is the transmission delay. The estimated received symbols are obtained using the MMSE technique.

(c) Proposed Transmission through Relay Link Based OSTBCs:

The proposed RS based OSTBC that used in LTE-A is shown in Fig. 2(c). We assume that the BS and RS with multiple antennas employ an OSTBCs transmission. Fig. 2(c) shows the system consists of one BS, one UE and one RS. The channel coefficient between the BS and the RS is denoted as H . Also, G is denoted as the channel coefficient between the

RS and the UE. We use four antennas for the BS, RS, and UE. We choose S_o to be the rate-3/4 OSTBC for 4 transmit antennas, which is given by [18-19]:

$$S_o = \begin{bmatrix} s_1 & s_2 & s_3 & 0 \\ -s_2^* & s_1^* & 0 & s_3 \\ s_3^* & 0 & -s_1^* & s_2 \\ 0 & s_3^* & -s_2^* & -s_1 \end{bmatrix} \quad (5)$$

Let the OSTBC S_o is transmitted from the BS. Then, The received signal matrix, $Y_{RS} \in C^{4 \times 1}$ at relay RS can be written as:

$$Y_{RS} = \sqrt{P_{BS}} \begin{bmatrix} h_{11} & h_{12} & h_{13} & h_{14} \\ h_{21} & h_{22} & h_{23} & h_{24} \\ h_{31} & h_{32} & h_{33} & h_{34} \\ h_{41} & h_{42} & h_{43} & h_{44} \end{bmatrix} \begin{bmatrix} s_1 & s_2 & s_3 & 0 \\ -s_2^* & s_1^* & 0 & s_3 \\ s_3^* & 0 & -s_1^* & s_2 \\ 0 & s_3^* & -s_2^* & -s_1 \end{bmatrix} + \begin{bmatrix} n_1 \\ n_2 \\ n_3 \\ n_4 \end{bmatrix} \quad (6)$$

Using CSI [21-22], the received signal is given by:

$$\hat{Y}_{RS} = \sqrt{P_{BS}} [\hat{h}_m s_1 \quad \hat{h}_m s_2 \quad \hat{h}_m s_3]^T + [\hat{n}_1^m \quad \hat{n}_2^m \quad \hat{n}_3^m]^T = \sqrt{P_{BS}} H_1 s + \hat{n}_1 \quad (7)$$

Where, $H_1 = \hat{h}_m = \sqrt{\sum_{i=1}^4 |h_{im}|^2}$, $s = [s_1 \quad s_2 \quad s_3]^T$ and

$$\hat{n}_1 = [\hat{n}_1^m \quad \hat{n}_1^m \quad \hat{n}_1^m]^T \quad ; (m = 1, 2, 3, 4)$$

Then in the next time slot, the RS transmit signal as follows:

$$X_{RS} = \sqrt{\frac{4P_{BS}P_{RS}}{L\gamma}} (A_1 s + B_1 \bar{s} + A_2 s + B_2 \bar{s} + A_3 s + B_3 \bar{s} + A_4 s + B_4 \bar{s}) H_1 \quad (8)$$

$$+ \sqrt{\frac{4P_{BS}P_{RS}}{L\gamma}} (A_1 \hat{n}_1 + B_1 \bar{\hat{n}}_1 + A_2 \hat{n}_2 + B_2 \bar{\hat{n}}_2 + A_3 \hat{n}_3 + B_3 \bar{\hat{n}}_3 + A_4 \hat{n}_4 + B_4 \bar{\hat{n}}_4)$$

Where, the matrices A_i and B_i are given by [23-25]:

$$A_1 = \begin{bmatrix} 1 & 0 & 0 \\ 0 & 0 & 0 \\ 0 & 0 & 0 \\ 0 & 0 & 0 \end{bmatrix}, A_2 = \begin{bmatrix} 0 & 1 & 0 \\ 0 & 0 & 0 \\ 0 & 0 & 0 \\ 0 & 0 & 0 \end{bmatrix}, A_3 = \begin{bmatrix} 0 & 0 & 1 \\ 0 & 0 & 0 \\ 0 & 0 & 0 \\ 0 & 0 & 0 \end{bmatrix}, A_4 = \begin{bmatrix} 0 & 0 & 0 \\ 0 & 0 & 1 \\ 0 & 1 & 0 \\ -1 & 0 & 0 \end{bmatrix} \quad (9)$$

$$B_1 = \begin{bmatrix} 0 & 0 & 0 \\ 0 & -1 & 0 \\ 0 & 0 & 1 \\ 0 & 0 & 0 \end{bmatrix}, B_2 = \begin{bmatrix} 0 & 0 & 0 \\ 1 & 0 & 0 \\ 0 & 0 & 0 \\ 0 & 0 & 1 \end{bmatrix}, B_3 = \begin{bmatrix} 0 & 0 & 0 \\ 0 & 0 & 0 \\ -1 & 0 & 0 \\ 0 & -1 & 0 \end{bmatrix}, B_4 = \begin{bmatrix} 0 & 0 & 0 \\ 0 & 0 & 0 \\ 0 & 0 & 0 \\ 0 & 0 & 0 \end{bmatrix} \quad (10)$$

Let

$$S_1 = (A_1 s + B_1 \bar{s} + A_2 s + B_2 \bar{s} + B_3 \bar{s} + A_4 s + B_4 \bar{s})$$

and

$$w_1 = (A_1 \hat{n}_1 + B_1 \bar{\hat{n}}_1 + A_2 \hat{n}_1 + B_2 \bar{\hat{n}}_1 + A_3 \hat{n}_3 + B_3 \bar{\hat{n}}_3 + A_4 \hat{n}_4 + B_4 \bar{\hat{n}}_4).$$

Then,

$$X_{RS} = \sqrt{\frac{4P_{BS}P_{RS}}{L\gamma}} (H_1 S_1 + w_1) \quad (11)$$

The total received signal matrix at UE is given by:

$$Y_{UE} = \left[\sum_{i,j=1}^4 G_{ij} X_{RS_j} + N_j \right] \quad (12)$$

4. Results

The simulation parameters for LTE-A downlink physical layer are listed in Table 1. The SER of UE at cell edge is high as it receives signals through direct link as shown in Fig. 3. The UE which receives signals from relay link gives low SER and better performance than UE that receive through direct link. The best performance and low SER are obtained when UE receive its signals from relay based OSTBCs. We compare the SER performance of the direct link, relay link and relay link based OSTBCs. We simulate different transmission scenarios to illustrate

the effect of using an OSTBC in RS. Fig. 3 shows the detected SER vs. SNRs for UE at different transmission scenarios.

The SER values for different transmission scenarios at different SNRs are listed in Table 2. At SNR=20dB, the proposed relay scheme in LTE-A gives SER equal 1.3×10^{-2} which is low compared to 5×10^{-2} and 3×10^{-2} for direct link and relay link, respectively. Thus it can be stated that by deploying OSTBCs into the LTE-A based RS system, better performance can be obtained.

The diversity gains for the proposed RS based OSTBCs at a $SER = 10^{-1}$, $SER = 10^{-2}$ and $SER = 10^{-3}$ are shown in Table 3. The proposed system that use OSTBCs in RS give high diversity gains compared to the other system. The diversity gain for proposed scheme is 5 dB at $SER = 10^{-1}$, which is high compared to relay link as shown in Table 3. The SER values for relay link based OSTBCs are low when we employ OSTBCs in RS in the communication path between BS and UE. Finally, the proposed relay selection scheme which employs OSTBCs improves the performance of LTE-A system.

Table 1: LTE-A Downlink Physical Layer Parameters [1]

Number of BS	1
Channel Bandwidth /1RB	20 MHz/180KHz
Frame / Subframe Duration	10ms / 1ms
Sub-carrier Spacing	15 KHz
Carrier Frequency	2 GHz
Cellular layout	Hexagonal grid, 1 cell, 3 sectors /cell
BS height	32m
Modulation	QPSK
Cyclic prefix	Normal
FFT size	2048
Channel Type	WINNER channel (B2)
Number of UE	1
UE height	1.5m
UE Receiver Type	Minimum Mean Square Error (MMSE)
Number of RS	1
RS height	25m
Type of relay	Amplify-and-Forward (AF)

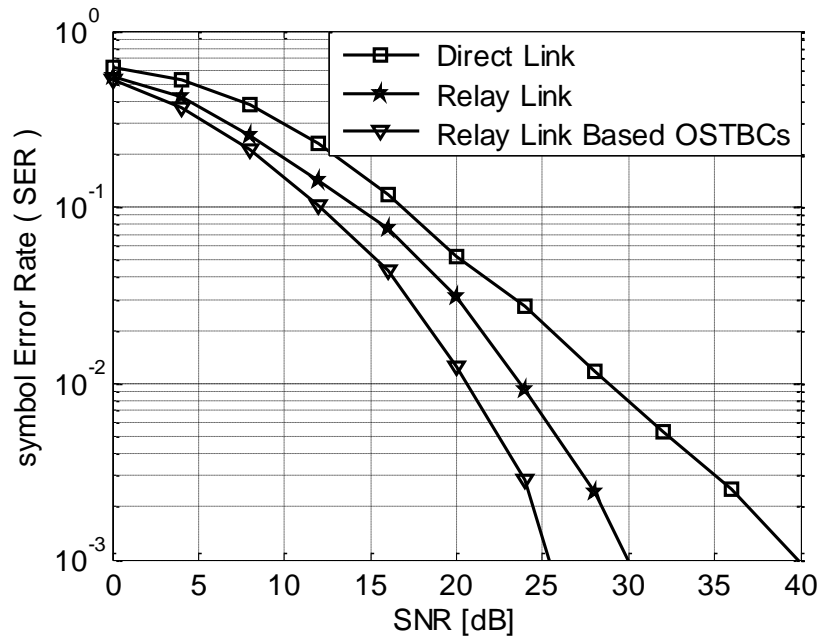


Fig. 3 Comparison of the SER performance for different transmission scenarios

Table 2: The SER values for different transmission scenarios at different SNRs

SNRs \ Scenario	5dB	10dB	15dB	20dB	25dB
Direct Link	5×10^{-1}	3×10^{-1}	1.5×10^{-1}	5×10^{-2}	2.2×10^{-2}
Relay Link	4×10^{-1}	2×10^{-1}	9×10^{-2}	3×10^{-2}	7×10^{-3}
Relay Link Based OSTBC	3×10^{-1}	1.5×10^{-1}	5×10^{-2}	1.3×10^{-2}	1.5×10^{-3}

Table 3: Diversity gains for the relay link and proposed relay link based OSTBCs at different SER

	SER = 10^{-1}	SER = 10^{-2}	SER = 10^{-3}
Relay Link	3 dB	5 dB	10 dB
Relay Link Based OSTBC	5 dB	8 dB	14 dB

5. Conclusion

In this paper, RS based OSTBCs for fourth generation cellular system (i.e. LTE-A) has been proposed. The received signals at UEs for different transmission scenarios have been mathematically derived and analyzed. The performance of LTE-A Downlink Physical Layer in the case of direct link, relay link and relay link based OSTBCs is compared. The SER performance for LTE-A with three transmission scenarios is calculated for a certain range of SNRs. Results show that the transmission link that uses RS based OSTBCs gives better performance than direct link and relay link.

References

- [1] Dahlman E, Parkvall S and Skold J, "4G: LTE/LTE-Advanced for Mobile Broadband," Academic Press, 2011.
- [2] Holma H and Toskala A, "LTE Advanced: 3GPP Solution for IMT-Advanced," John Wiley & Sons, 2012.
- [3] Holma H and Toskala A, "LTE for UMTS: Evolution to LTE-Advanced," John Wiley & Sons, 2011.
- [4] Ghosh A, Ratasuk R, Mondal B, Mangalvedhe N and Thomas T, "LTE-advanced: Next-Generation Wireless Broadband Technology," IEEE Wireless Communications, vol. 17, no. 3, pp. 10-22, 2010.
- [5] Ko K and Woo C, "Outage Probability and Channel Capacity for the Nth Best Relay Selection AF Relaying over INID Rayleigh Fading Channels," International Journal of Communication Systems, vol. 25, no. 11, pp. 1496–1504, 2010.
- [6] Tao X, Xu X and Cui Q, "An Overview of Cooperative Communications," IEEE Communications, vol. 50, no. 6, pp. 65-71, Jun 2012.
- [7] Bulakci O, Bou Saleh A, Redana S, Raaf B and Hamalainen J, "Resource Sharing in LTE-Advanced Relay Networks: Uplink System Performance Analysis," J. Wiley Emerg, Telecommun. Technol. Special Issue on LTE / LTE-Advanced, vol. 24, no. 1, pp. 32–48, 2013.
- [8] Lei L, Zhong Z, Lin C and Shen X, "Operator Controlled Device-to-Device Communications in LTE-Advanced Networks," IEEE Wireless Communications, vol. 19, no. 3, pp. 96–104, 2012.
- [9] Yang Y and Aissa S, "Information-Guided transmission in Decode-and-Forward Relaying Systems: Spatial Exploitation and Throughput Enhancement," IEE Trans. Wireless Communications, vol. 10, no. 7, pp. 2341–2351, 2011.
- [10] Sugiura S, Chen S, Haas H, Grant PM and Hanzo L, "Coherent Versus Non-Coherent Decode-and-Forward Relaying Aided Cooperative Space-Time Shift Keying," IEEE Trans. Communications, vol. 59, no. 6, pp. 1707–1719, 2011.

- [11] Di Renzo M, Haas H and Grant PM, "Spatial Modulation for Multiple-Antenna Wireless Systems: A Survey," *IEEE Trans. Communications Magazine*, vol. 49, no. 12, pp. 182–191, 2011.
- [12] 3GPP TS 36.201, "Long Term Evolution (LTE) Physical Layer," General Description. March 2009, Release 8, V8.3.0.
- [13] Yang Yang, Honglin Hu, Jing Xu and Guoqiang Mao, "Relay Technologies for WiMAX and LTE- Advanced Mobile Systems," *IEEE Communications Magazine*, October 2009.
- [14] Tommaso Beniero, Simone Redana, Jyri Hamalainen and Bernhard Raaf, "Effect of Relaying on Coverage in 3GPP LTE-Advanced," *IEEE 69th Vehicular Technology Conference, VTC Spring 2009, Barcelona*.
- [15] Nabar R, Bolcskei H and Kneubuhler F, "Fading Relay Channels: Performance Limits and Space-Time Signal Design," *IEEE Journal Selected Areas Communications*, vol. 22, no. 6, pp. 1099–1109, 2004.
- [16] Jing Y and Hassibi B, "Distributed Space-Time Coding in Wireless Relay Networks," *IEEE Wireless Comm.*, vol. 5, no. 12, pp. 3524–3536, 2006.
- [17] Susinder Rajan G and Sundar Rajan B, "A Non-Orthogonal Distributed Space-Time Coded Protocol, Part-I: Signal Model and Design Criteria," *Proceedings in IEEE Information Theory Workshop, IEEE, Punta del Este, Uruguay*, pp. 385–389, October 2006.
- [18] Laneman J and Wornell G, "Distributed Space-Time-Coded Protocols for Exploiting Cooperative Diversity in Wireless Networks," *IEEE Trans. Information Theory*, vol. 49, no. 10, pp. 2415–2425, 2003.
- [19] [19] Kiran T and Rajan B, "Distributed Space-Time Codes with Reduced Decoding Complexity," *IEEE International Symposium on Information Theory*, pp. 542–546, 2006.
- [20] Kai Yang, JieYang and Liyu Cai, "Dual-hop MIMO Relaying with OSTBC over Doubly Correlated Nakagami-m Fading Channels," *EURASIP Journal on Wireless Communications and Networking*, vol. 2012, 2012.
- [21] Oggier F and Hassibi B, "Code Design for Multihop Wireless Relay Networks," *EURASIP Journal on Advances in Signal Processing*, vol. 2008, no. 68, 2008.
- [22] Sreeram K, Birenjith S and Kumar P, "Dmt of Multihop Networks: End Points and Computational Tools," *IEEE Trans. Information Theory*, vol. 58, no. 2, pp. 804–819, 2012.
- [23] Cristina La Palombara, Velio Tralli, Barbara M. Masini and Andrea Conti, "Relay-Assisted Diversity Communications," *IEEE Trans. VEHICULAR TECHNOLOGY*, vol. 62, no. 1, pp. 415-421, JANUARY 2013.
- [24] Guangping Li, Steven D. Blostein and Jiuchao Feng, "Performance Analysis of OSTBC Transmission in Multiuser Multiantenna Relay Networks," *IEEE Trans. VEHICULAR TECHNOLOGY*, vol. 62, no. 1, pp. 421-427, JANUARY 2013.
- [25] Rahul Vaze1 and Robert W Heath Jr, "Cascaded Orthogonal Space-Time Block Codes for Wireless Multi-Hop Relay Networks," *EURASIP Journal on Wireless Communications and Networking*, vol. 2013, no. 113, 2013.

Memristor Overview up to 2015

Sherif F. Nafea¹, Ahmed A.S. Dessouki² and S. El-Rabaie³

¹Dept of Elect Eng., Fac. of Eng., Ismailia, Suez Canal Univ., Egypt.

²Dept. of Elect Eng., Fac. of Eng., Port Said, Port Said Univ., Egypt.

³Dept. of Electronics and Electrical Communications, Faculty of Electronic Engineering, Menoufia University, Menouf, Egypt.

(Received: 11-October-2015 – Accepted: 05-November-2015)

Abstract

Until 1971, the known three fundamental electrical elements were resistor, inductor, and capacitor. In 1971, Professor Leon Chua proposed theoretically a fourth fundamental electric element, and he called it "Memristor." Memristor is a two-terminal element whose resistance depends on the magnitude, direction, and duration of the applied voltage. This element is realized later by HP labs in 2008, which opened a wide area of research on the memristor and its possible applications. This paper gives an overview of the device properties, fabrication, modeling approaches of the memristor and some possible future improvements. The paper also surveys the digital and analog applications of memristors, and possible future improvements in some applications.

1. Introduction

Memristor is a passive two terminal electrical component which functions as a fundamental non-linear circuit element relating charge and magnetic flux linkage. The Memristor is considered to be a promising device in many applications, analog and digital, especially in memory chips, logic circuits, and neural networks.

In 1971, Prof. Leon Chua [1] reasoned from symmetry as shown in Fig.1 that there should be a fourth fundamental element, which he called a memristor (short for memory-resistor).

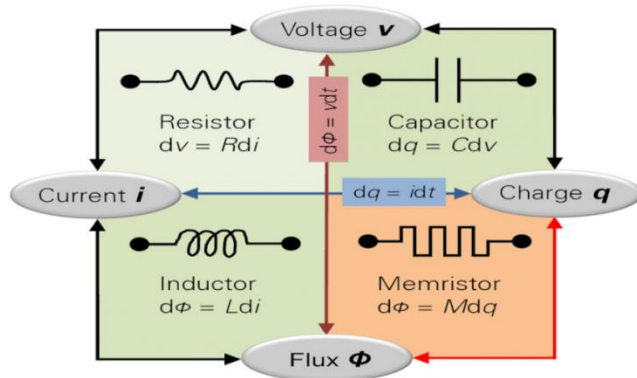


Fig.1 Fundamental Circuit Variable Relationships[2]

In 2008, members of an HP Lab published [3] that they successfully realized a nanoscale electronic component, whose measured physical properties can be explained by the memristor theory. The HP memristor is a solid-state device formed of a nanometer scale TiO₂ thin film, containing a doped and an undoped region sandwiched between two Platinum electrodes as shown in Fig.2.

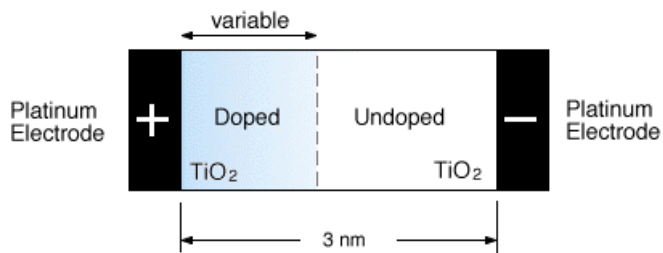


Fig.2 Titanium Dioxide Memristor

Since 2008, many applications have been proposed for the memristor. In the field of memory chips, memristors can be used in Resistive Random Access Memory (RRAM) cell structures, and Memristor-based Content Addressable Memories (MCAMs) using a combination of memristor and MOS devices. In neural networks, the memristor can be used effectively to reduce the area and complicity of neuromorphic circuits benefiting from the ability of memristor to “memorize” the current pass in it and its direction. In the field of logic circuits, a new type of memristor-based IMPLY logic circuits were implemented. The memristor based logic has a unique ability that it can be fabricated with memory cells on the same chip. Memristors are used also in the design of crossbar-arrays which are

used in the switching blocks of the Field Programmable Gate Arrays (FPGAs).

The paper is organized as follows: Section 2 discusses briefly the device properties of memristors. Section 3 covers different methods of memristors' fabrication and some possible future improvements. Section 4 surveys the main methods of modelling, and emulating memristors. Memristor based memory circuits are discussed in section 5 with possible future improvements. Section 6, discusses using memristors in neuromorphic applications. Memristor based logic and FPGA are discussed in section 7. Analogue applications are briefly discussed in section 8. Finally, the conclusion is presented in section 9.

2. Device Properties

As mentioned, memristor relates charge (q) and magnetic flux (φ). The q - φ relation is nonlinear, thus the memristor's parameter that relates q and φ is not a constant. The memristor is said to be charge-controlled with a memristance ' $M(q)$ ' equals:

$$M(q) = d\varphi/dq \quad (1)$$

Similarly, the memristor is said to be flux-controlled with a memductance ' $W(\varphi)$ ' equals:

$$W(\varphi) = dq/d\varphi \quad (2)$$

From (1) and (2), it can be derived that:

$$v = M(q) . i \quad (3)$$

$$i = W(\varphi) . v \quad (4)$$

2.1 Current-Voltage (I-V) Characteristic

Fig.3 shows the difference between the current-voltage characteristic of the four basic components. As shown in the figure, the memristor has a hysteresis (I-V) characteristic. It should be noted that the I-V characteristic of the memristor cannot be achieved using any combination of the other

three basic components, therefore the memristor is considered a basic component. A theoretical approach to the various classes of memristive devices as nonlinear dynamical systems is given in [4].

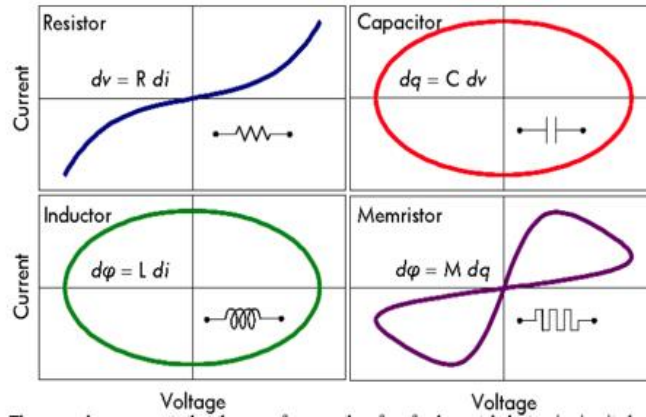


Fig.3 Current-voltage characteristics for the resistor, capacitor, inductor and memristor [5].

3. Fabrication

The implementation of memristors can be categorized into two main categories; the first category is Molecular and Ionic Thin Film memristors, and the second is spin-based memristors [6].

3.1 Molecular and Ionic Thin Film memristors

This type of memristors mainly depends on thin film atomic lattices of different materials that shows hysteresis under the application of charge.

3.1.1 Titanium Dioxide Memristor

As mentioned, the titanium dioxide memristor was proposed by members of an HP Lab. The device is composed of a thin (50 nm) titanium dioxide film between two 5 nm thick electrodes, one is titanium, and the other is platinum. The titanium dioxide film consists of two layers, one of which has a slight depletion of oxygen atoms (undoped). The other is the doped

layer with oxygen vacancies which act as charge carriers. The doped layer has a much lower resistance than the undoped layer.

The influence of the temperature on TiO₂ memristor properties was studied in [7, 8]. [7] found that the increasing of ambient and working temperatures of TiO₂ memristor has a bad influence on its properties and characteristics. Thus he recommended using a cooling device to keep its performance. [8] explored the Dynamic Thermal Management (DTM) profiling in CMOS/memristor memory architectures, and recommended that DTM mechanisms are needed to improve CMOS/memristor reliability and lifetime. [9] discussed the *radiation effects* on TiO₂-based memristors including the implications on the nanometre scaled TiO₂ memristor devices and how that affects the energy deposition from the various radiation sources.

3.1.2 Polymeric Memristor

Polymeric memristors explore dynamic doping of polymer and inorganic dielectric-type material to achieve a hysteresis current-voltage characteristics. Usually, a single passive layer between an electrode and an active thin film try to enlarge the extraction of ions from the electrode. In 2008, the polymeric memristor was developed by Erokhin and Fontana [10]. Then in 2012, organic ion-based memristors were used in designing neural synaptic memory circuits [11].

3.1.3 Ferroelectric Memristor

The ferroelectric memristor[12] uses a thin ferroelectric barrier sandwiched between two metallic electrodes. Switching the polarization of the ferroelectric material by applying a positive or negative voltage across the junction which leads to a two order of magnitude resistances (R_{OFF} , and R_{ON}), where: $R_{OFF} \gg R_{ON}$. The polarization does not switch abruptly, thus when the voltage is cycled; the ferroelectric domain configuration evolves, allowing a fine tuning of the resistance value.

A new type of ferroelectric tunnel junction memristors is demonstrated in [13]. The ferroelectric tunnel memristors exhibit a non-volatile resistive switching with a resistance ratio of up to 105 % at room temperature.

3.1.4 Other types of molecular Memristors:

[14] proposed fabricating memristive devices with ZnO thin film using electro-hydrodynamic printing. The advantage of this technique is its simplicity and its low cost. McDonald[15] discussed the fabrication of Al/Cu_xO/Cu memristive devices created by depositing Al top electrodes atop a Cu_xO film grown using plasma oxidation to grow the oxide on a Cu wafer. A rewriteable non-volatile physically flexible memristor device with a low-power operation is demonstrated in [16]. The device demonstrates an on/off ratio greater than 10000: 1, is non-volatile for over 1.2×10^6 s, requires less than 10V, and is still operational after being physically flexed more than 4000 times.

A low cost type of memristors using anodization is proposed in [17] . Jorhan Rainier[18] proposed improving the performance of the memristor devices by adding an additional anneal step before the top electrode deposition. Bipolar memristor crossbar structures, suitable for high scalability, were proposed by Janice H. Nickel et al., and have been fabricated in a fully compatible Back-End-of-Line materials and processes[19].

3.2 Spintronic Memristors

Chen et al. [20] described three different possible designs of spin-transfer torque based magnetic memristors. A promising structure is the domain-wall spintronic memristor, in which the device resistance occurs when the spin of electrons in one section of the device points in a different direction from those in another section, creating a boundary between the two sections called a “domain wall”. Electrons flowing into the device have a certain spin, which alters the device’s magnetization state. Changing the magnetization of the device moves the domain wall and changes its resistance.

3.3 Future Work in Fabrication

Sung Hyun [21] studied the behaviour of digital memristor devices through a filament formation picture, however, it is still based on indirect observation, and the filament has not been directly observed in the nanoscale devices. Conducting cross-sectional TEM studies would provide direct information about the nature of the Ag filaments and

explain the resistance switching mechanism in the nanoscale amorphous silicon devices.

Cory Merkel [7] studied the effect of temperature on thin-film memristors. Only one of the temperature dependencies in thin-film memristors, ion mobility, was considered. An extension of this work could consider the effects of temperature in crossbar nanowires as well as CMOS components. The temperature dependence of ion diffusion and electron transport, as well as the effect of heat generation in the crossbar layer can also be considered in future models.

A future work of using a new electrolyte that does not contain the fluoride for growing the TiO₂ nanotubes were proposed in [17], and proposed also trying different anodization times to bring a better understanding for how thick of an oxide it takes to create the best memristor and produce more data for characterizing the thickness of oxide grown. Tungsten oxide memristive devices were proposed for neuromorphic applications in [22]. A possible future work in this field is to conduct in-depth material study of WOX films, quantitative study of resistive switching in WOX memristors, and relating calcium ion dynamics with oxygen vacancy dynamics.

4. Modelling and Emulating Memristors

As is the case of any new technology, it is important to learn how the memristor behaves to external stimulus in terms of voltage and current. Memristor models need to be made available for the design engineers to use the memristor as a circuit element during design exploration. There are a lot of proposed models of memristors depending on the needed compromise between simplicity and accuracy and on the type of application. In this section, we try to cover the main models of memristors.

4.1 Linear Ion Drift Model

The model discussed here is based on the HP memristor shown in Fig.4. In Linear Ion Drift model, a uniform electric field across the device is

assumed; thus, there is a linear relationship between drift–diffusion velocity and the net electric field.

$$\frac{dw(t)}{dt} = \mu_V \frac{R_{ON}}{D} i(t) \quad (5)$$

where D is the total TiO_2 length, $w(t)$ is a state variable defining the length of the doped TiO_2 , R_{ON} is the equivalent resistance of the memristor when the whole device is doped, μ_V is the average ion mobility.

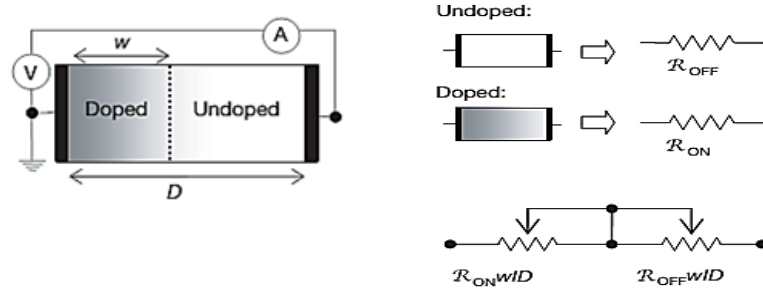


Fig. 4 The coupled variable-resistor model for a memristor [3].

According to the linear ion drift; the memristor can be modelled as a coupled variable-resistor model as shown in Fig.4, yielding the following I-V relationship[3]:

$$v(t) = \left(R_{ON} \frac{w(t)}{D} + R_{OFF} \left(1 - \frac{w(t)}{D} \right) \right) i(t) \quad (6)$$

Where, R_{OFF} is the equivalent resistance of the memristor when the whole device is undoped.

Solving equations (5) and (6) the memristance of the device, for $R_{OFF} \gg R_{ON}$, simplifies to:

$$M(q) = R_{OFF} \left(1 - \frac{\mu_V R_{ON}}{D^2} q(t) \right) \quad (7)$$

The coupled equations of motion for the charged dopants and the electrons in this device take the normal form for a current-controlled (or charge-controlled) memristor as in (3), (5).

4.2 Nonlinear Ion Drift Model

The nanometre dimensions of memristor causes a high electric field with only applying a few volts. Thus, the electric field can easily exceed 10^6V/cm , and it is reasonable to expect a high nonlinearity in the ionic

drift-diffusion. The linear drift assumption also suffers from a problem in incorporating boundary effects.

A few attempts have been carried out so far to consider this nonlinearity in the state equation[3],[23], [24]. Each paper proposed using a different ‘window function $F(w/D)$ ’ multiplied by the right-hand side of the state equation (Eq.5). Thus, the state equation can be modified to be as follows:

$$\frac{dw(t)}{dt} = \mu_V \frac{R_{ON}}{D} i(t) F\left(\frac{w}{D}\right) \quad (8)$$

Qualitatively, the boundary between the doped and undoped regions moves with speed v_d in the bulk of the memristor, but that speed is strongly suppressed when it approached either edge, $w \sim 0$ or $w \sim D$. Thus, the window function should satisfy $F(0)=F(1)=0$ to ensure no drift at the boundaries.

4.2.1 Window function

The choice of the suitable nonlinear drift model depends on the proper choice of the window function. Many papers proposed different window functions that attempt to achieve a good agreement with the nonlinear behaviour and less simulation problems. For example, Joglekar et al.[25] proposed the following window function:

$$f(w) = 1 - (2(w/D) - 1)^{2p} \quad (9)$$

where p is a control parameter that defines the curvature of the window function. This model is simple and it can achieve the boundary condition, but on the other hand once the state variable $w(t)$ reaches one of the boundaries the rate of change of the state variable " $dw(t)/dt$ " is zero and the state variable $w(t)$ is trapped at this boundary. Biolek [26] proposed another window function that can overcome this problem as follows:

$$f(w) = 1 - ((w/D) - u(i))^{2p} \quad (10)$$

Where, $u(-i)$ is the unity function as a function of the direction of the current. Both window functions do not have a scale factor and therefore the maximum value of the window function cannot be changed to a value lower or greater than one. Refer to [27] for more details on window functions. In 2015, a newly proposed window function modified the Joglekar window for a better accuracy to be as follows [28] :

$$f(w) = j \left(1 - \left[\left(\frac{w}{D} - 0.5 \right) + 0.75 \right]^{\tanh(P)} \right) \quad (11)$$

4.3 Simmons Tunnel Barrier Model

This model [29] assumes nonlinear and asymmetric switching behaviour due to an exponential dependence of the movement of the ionized dopants. In this model, rather than two resistors in series as in the linear drift model, there is a resistor in series with an electron tunnel barrier. In this model, the state variable 'x' is the Simmons tunnel barrier width. Fig.5 shows the schematic of the device cross section, and an example switching I-V curve. This model gives high accuracy in modelling practical memristors; however, the current-voltage relationship is complicated and Ambiguous.

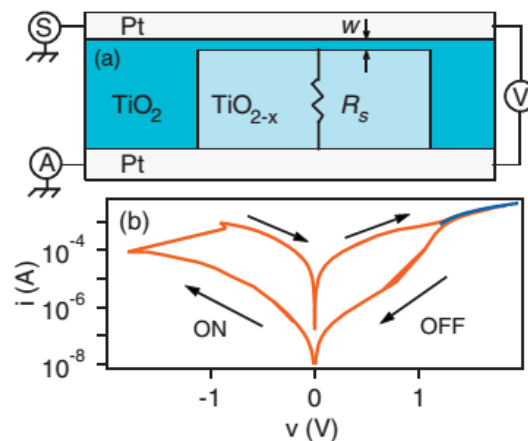


Fig. 5: Device schematic and characterization protocol. (a) Schematic of the device cross section (b) Example switching i - v curve for the device. [29]

4.4 ThrEshold Adaptive Memristor (TEAM) Model

The TEAM model[27] is a general memristor model assumes that the memristor has a current threshold and polynomial dependence between the memristor current and the internal state drift derivative. The current-voltage relationship can be in a linear or exponential manner. It is possible to fit the TEAM model to the Simmons tunnel barrier model or to any different memristor model and gain a more efficient computational time. The model is reasonably accurate and computationally efficient.

4.5 SPICE Macro-modeling

Basically, there are three different ways to model the electrical characteristics of the memristors; SPICE macro-models, hardware description language (HDL) and C programming. Regardless of common convergence problems in SPICE modelling, it is a more appropriate way to describe a real device operation.

In 2009, Biolek proposed memristor SPICE model with nonlinear dopant drift as shown in Fig.6 [26].

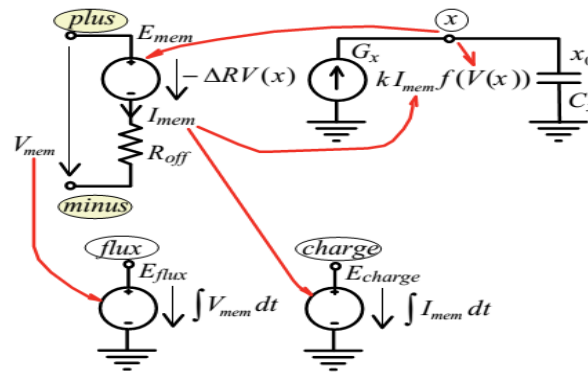


Fig. 6 Structure of the SPICE model proposed in [26]

Another way to realize memristor SPICE model is by connecting an appropriate nonlinear resistor, inductor, or capacitor with an M-R mutator, and an M-L mutator, or an M-C mutator, respectively[30]. These mutators are nonlinear circuit elements that may be described by a SPICE macro-model as shown in Fig.7.

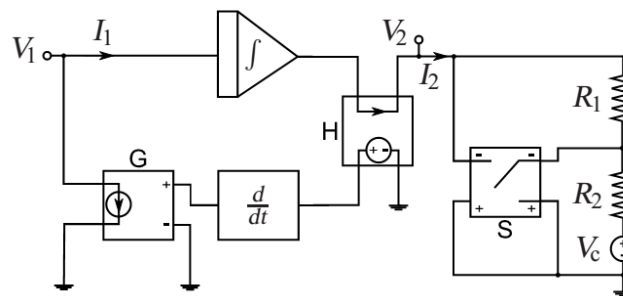


Fig.7 A SPICE macro-model using mutators [30].

In 2010, Rák and Cserey proposed a nonlinear SPICE macromodel [31]. The model achieved a quantitatively similar behaviour to the measurements of the memristor physical implementation. Compact memristor models using LTSpice based on the fundamental constitutive relationships between charge and flux of is introduced in [32]. Also, the model proposed by HP Labs is modelled in LTSpice [33].

4.6 Memristor Emulation

The fabrication technology of memristor devices is still not available for most of the researchers. Thus, it would be helpful if we can use an emulator circuit using existing devices to study the main characteristics of memristor devices and applications. In 2010, Mutlu and Karakulak proposed an emulator circuit to the TiO_2 memristor with linear dopant drift using analogue multiplier [34]. Fig.8 shows the proposed emulator circuit.

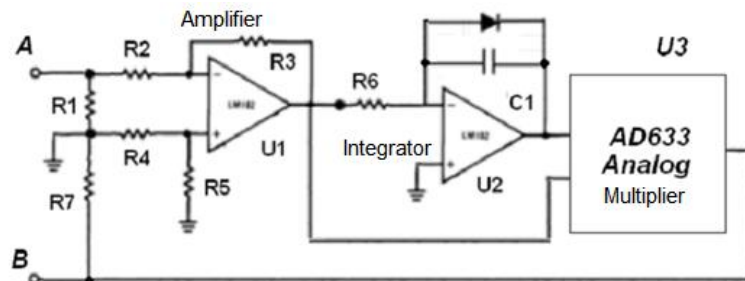


Fig. 8 Memristor Mutlu Emulator circuit [34]

Another emulator circuit is proposed in [35]. This emulator is designed to be easily expandable. In [36], an emulator circuit that can describe the memristor's current-voltage relationship using a voltage-controlled resistor is implemented, where its resistance can be programmed by the stored voltage at the state variable capacitor. Lin Teng constituted a significant finding that it should be possible to physically implement a memristor emulator circuits capable of generating complex chaotic behaviour without the need for resource-intensive FPGAs or microcontrollers to model high-order nonlinearity[37]. In 2015, a memristor emulator that embraces most of features of a real memristor is proposed [38]. The small variation range of memristance and the nonfloating operation that limit conventional memristor emulators are improved significantly in this emulator.

4.7 Development in Memristor Modeling:

In 2010, A. G. Radwan derived mathematical models of the HP Memristor for DC and periodic signal inputs [39]. Unlike the previous works that focused only on the sinusoidal input waveform, this model derived the rules for any periodic signals in terms of voltage and current. An\ physic-based SPICE model was proposed by Pickett [40]. Pickett's model is considered to be the HP memristor's standard model, and other models are compared to it. A compact memristor model consists of a set of analytical equations and can be implemented by Verilog-A language was introduced in [41]. In 2011, Batas and Fiedler introduced a behavioural model of a memristive solid state device [42].

In order to gain more vision of the physical mechanisms of analogue memristors, a model based on the finite element method was demonstrated in [43]. Shahar Kvatinsky proposed a Verilog-A implementation for the linear, nonlinear, and TEAM memristor models, and their relevant window functions, which is suitable for SPICE-based CAD tools such as CADENCE[44].

In 2012, Fernando García presented a memristor model characterization framework which supports automated generation of sub circuit files [45]. The proposed environment allows the designer to choose and parameterize the memristor model that best suits for a given application. M. Condon discussed the simulation of memristors when they are subject to high-frequency forcing functions[46]. Also a novel asymptotic-numeric simulation method is applied in this model. An accurate analytical models for the performance and the energy dissipation of a 1-transistor 1-memristor (1T1R) resistive random access memory (RRAM) cell structures is presented in [47]. The model was verified using HSPICE simulations. A class of models that generate a broad universe of elements using fractional calculus were introduced in [48]. Several combinations of values are tested, and the corresponding dynamical behaviour is analysed. In 2013, Shiping Wen proposed a new fuzzy model of memristor-based Lorenz circuit to simulate and synchronize with the memristor-based Chua's circuit [49].

A good overview of Physics-based memristor models was presented by Stanley Williams [50], through which a simpler, analytical approximations that can match the measured behaviour of the memristors over many orders of magnitude in time and a wide range of

applied voltage was proposed. Yang Liu proposed that we can utilize approaches such as profiling, trace based simulation and statistical models for evaluation to obtain more accurate results [51].

Despite having many linear, and nonlinear memristor models, accurate physic based memristor models with acceptable complexity is still needed. Existed accurate models such as Pickett's memristor model are very complicated and cause many convergence issues in SPICE simulators, beside the difficulty of representing these models using Verilog-A which makes these models lack the connection to some important CAD tools.

5. Memristors Memories

Among emerging nanotechnologies, memristors are very promising candidates to build storage structures because of high capacity, short switching time and low power consumption. However, the benefit we can obtain from these storage structures is still limited by the low endurance, and the required mature technology of memristors.

5.1 Resistive Random-Access Memory

The memristor has the potential to be a non-volatile memory element, since it holds its resistive value, even after it is unplugged from a power source. Resistive random-access memory (RRAM) that depends on memristor-CMOS technology could be the future of non-volatile memories. Cong Xu et al.[52] conducted a study on the memristor based RRAM array design and focus on the choices of different peripherals to achieve the best trade-off between performance, energy, and area. Sung Hyun Jo[21] proposed fabricating RRAM using Amorphous Silicon, and studied the crossbar arrays based on Amorphous Silicon RRAM. Muhammad Shakeel et al.[53] described using CMOS interface circuits in 350nm 3.3V/5.0V TSMC process for memristor crossbar arrays for memristor based RRAMs.

5.2 Memristor-based Content Addressable Memory

Kamran provided a new approach of designing and modelling Memristor-based Content Addressable Memories (MCAMs) using a combination of memristor and MOS devices [54]. Chen reported applying the memristor delayed switching effect to the design of the M-CAM cell [55]. The delayed switching effect is used to control the changing time of the memristor's state, which can enhance the performance, decrease the searching time and save energy. Yang Liu proposed a configurable memristor-based CAM/TCAM design [51]. Liu's configuration can use memristors as both memory latches and logic gates.

5.3 Sneak Path Problem

One of the most important issues that face memristor-based memories is the sneak path problem. This problem arises from the fact that the memristor device has "no gate". Thus undesired paths of current form a resistance in parallel with the main path resistance.

A new non-destructive read-out technique is reported in [56]. Yenpo Ho developed a set of properties and design equations for memristor based memories targeting key electrical memristor device characteristics relevant to memory operations [57]. M. Affan investigated the read operation of memristor-based memories, analysed the sneak paths problem, and studied the effect of the aspect ratio of the memory array on the sneak paths[58]. New approach to solve the sneak path problem in crossbars arrays is provided in [59].

5.4 Future Work in Memristor based Memory Circuits

Cory E. Merkel discussed the sneak paths in the crossbar circuits by considering $1 \times N$ and $M \times 1$ crossbar circuits [7]. Future work can explore the use of general $M \times N$ crossbar circuits with different sneak path mitigation techniques. Another future work is to try to improve sensor accuracy using high-speed clocks for temperature sensing resistive random access memory (TS-RRAM) block timer circuits. Another extension of this work could be exploring a higher-level dynamic thermal management (DTM) triggering and DTM response mechanisms.

Yang Liu proposed utilizing approaches such as profiling, trace-based simulation and statistical models for evaluation to obtain more accurate memristor based memories results [51]. Furthermore, he proposed that we could evaluate insert/delete operations to discover a threshold update rate, which decides whether an application can benefit from hybrid storage structures or not. Another possible future research direction is to explore other interfaces and management aspects such as virtualization.

The evaluation of system-level impacts of a persistent main memory architectures is analysed in [60]. An extension to this work, using persistent main memory instead of separating the memory hierarchy in volatile main memory and persistent storage is proposed. The benefit of orthogonal persistence is to improve programming productivity from simpler semantics, avoiding ad-hoc arrangements for data translation and long-term data storage, and providing protection mechanisms over the whole environment.

6. Memristors Neuromorphic Applications

The field of memristor-based neuromorphic applications is a very promising field, and gains a wide research interest. Using memristors as a synapses in neuromorphic circuits can potentially offer both high connectivity, and high density required for efficient computing.

In 2010, a memristive magnetic tunnel junction is used as a complete synapse-neuron [61]. A nanoscale silicon-based memristor device was experimentally demonstrated in [62], and used in a hybrid system composed of CMOS neurons and memristor synapses to support important synaptic functions such as spike timing dependent plasticity(STDP). Nathan McDonald analysed some promising and practical non-quasi-static linear and non-linear memristor device models for neuromorphic circuit design and computing architecture simulation [63].

In 2011, Djaafar Chabi described a neural learning method to implement Boolean functions in memristor Neural Logic Blocks(NLB) [64]. A denser and more robust Associative Memories (AM) designs using memristor networks is provided in [65]. The technique is based on weighing the trade-offs within the fitness function.

In 2012, Ting Chang explored the material properties, device characteristics, synaptic plasticity implementations, and CMOS integration of tungsten oxide (WOX) nanoscale memristors, and advancing this technology for neuromorphic applications[22]. Such devices offer simple fabrication, low-power, high-density, scalability, connectivity, and CMOS-compatibility, making them ideal candidates for neuromorphic applications. Michael Soltiz proved that the scalability and efficiency of hardware-based neuromorphic systems can be improved drastically by adding complexity to neural logic block (NLB) designs [66]. An overview on mimicking synaptic plasticity in memristive neuromorphic systems is discussed in [67, 68] .

Synapse implementations, however, have proven difficult, due to a lack of inherently plastic circuit elements. This leads to the need of overly complex circuits to mimic any kind of plasticity. Memristors turn out to be very powerful for mimicking synaptic plasticity. Ebong and Mazumder analysed using two basic learning rules: winner-take-all (WTA) and STDP [69]. He also gives a design example implementing WTA combined with STDP in a position detector. CMOS and a memristor MOS technology (MMOST) design simulation results are compared on the bases of power, area, and noise handling capabilities. A neuromorphic approach in which STDP can be combined with memristors in order to withstand noise in circuits is provided in [70]. The analogue approach to STDP implementation with memristors shows a superior to a digital-only approach.

A. Wu and Z. Zeng introduced a general class of memristor-based recurrent *neural networks with time-varying delays* [71]. Exponential convergence of the networks is studied by using local invariant sets. Shiping Wen investigated the exponential stability problem about the memristor-based recurrent neural networks[72]. He provides the criteria for memristor-based neural networks with time-varying delays. These stability conditions can also be used for memristor-based neural networks with constant time delays or without time delays. Z. Guo addressed the global exponential dissipativity of memristor-based recurrent neural networks with time-varying delays by constructing proper Lyapunov functional and using M-matrix theory and LaSalle invariant principle [73]. the problem of global exponential synchronization of a class of memristor-based recurrent neural networks with time-varying delays based on the fuzzy theory and Lyapunov method is discussed in [74, 75] . Theoretical results on the global exponential periodicity and stability of a class of

memristor-based recurrent neural networks with multiple delays is analysed in [76]. By using the inequality techniques and a useful Lyapunov functional, some new testable algebraic criteria are obtained for ensuring the existence and global exponential stability of periodic solution of the system.

Guodong Zhang analysed general memristor-based recurrent neural networks with time-varying delays (DRNNs)[77]. The dynamic analysis in the paper employs results from the theory of differential equations with discontinuous right-hand side as introduced by Filippov. Ling Chen proposed a synapse memristor model with forgetting effect that can describe the basic memory ability of memristor and able to capture the new finding forgetting behaviour in memristor [55]. Z. Cai and L. Huang formulated and investigate a class of memristor-based Bidirectional Associative Memory (BAM) neural networks with time-varying delays under the framework of Filippov solutions [78].

In 2015, a unipolar organic memristor device with multiple thresholds that offers advantages for on-chip supervised learning is proposed[79]. Additionally, the new organic devices proved highly resilient to parasitics and sneak paths.

6.1 Future work in Memristors Neuromorphic Applications

Michael Soltiz proposed a future work of improving the NLB(neural logic block) designs and applying them to new application domains [66]. Conducting further modification of the MRII algorithm or development of another hardware-friendly learning algorithm can enhance memristor-based neuromorphic applications[80].

In [70], Idongesit Eong claimed that the hardware used for the reinforcement learning problem can be a starting point to realizing this adaptive-critic design. The steps involved would be to: (1) Modify architecture for multiple algorithms, e.g., greedy exploration, not just the greedy algorithm espoused in Chapter V; (2)Circuit redesign of the proposed hardware to account for bidirectional neurons; (3)Since combining with CMOS and possibly the microprocessor, multiplexing methods for specified bus widths of the processor should be investigated. These aforementioned steps will be intermediaries to achieving hardware for algorithms that require higher level abstraction like the optimal control problem.

7. Memristors Logic / FPGA Applications

An important advantage of memristors is that it can be used in designing a combined memory and logic functions on the same chip. The memristors can be used efficiently in crossbar arrays for both memory and logic functioning.

Memristor-based crossbar arrays can be used to compute logic functions based on the placement of the switches on the wire junctions and based on their state. Current crossbar-based logic designs have inherent disadvantages to conventional CMOS design in terms of performance (wire delay is dominant in crossbar designs), density (large unused areas) and power dissipation (most of the unused switches in junctions are inactive and hence consume leakage power.)

7.1 Logic Circuits

Memristors can be used to perform *implied* logic operations. It is important to note that the logic circuits realized by memristor differ than the Boolean logic realized by CMOS technology. The realization of implied logic is explained in [81]. T. Raja and S. Mourad provided a tutorial on how to use memristor crossbars for logic design and is a consolidation of various recent publications [82]. Hybrid reconfigurable logic circuits is fabricated by integrating memristor-based crossbars onto a foundry-built CMOS platform using nano-imprint lithography [83].

7.2 Field Programmable Gate Arrays

A novel FPGA architecture with memristor-based reconfiguration (mrFPGA) was introduced in [84]. The proposed architecture is based on a CMOS-compatible memristor fabrication process. The programmable interconnects of mrFPGA use only memristors and metal wires. Thus, the interconnections can be fabricated over logic blocks, resulting in significant reduction of overall area and interconnect delay. D. Strukov and A. Mishchenko also introduced novel FPGA circuits based on hybrid CMOS/resistive switching device (memristor) technology to achieve different logic architectures [85].

8. Memristors Analogue Applications

Memristors can be used to implement programmable analogue circuits, Amplifiers, and oscillators. Sangho Shin showed that memristors can be used to implement programmable analogue circuits, leveraging memristor's fine-resolution programmable resistance without causing perturbations due to parasitic components [86]. The resistance programming can be achieved by controlling the input pulse width and its frequency. A Pulse-coded programmable resistor using memristor is shown in Fig.9.

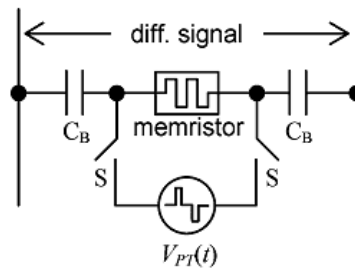


Fig. 9 Pulse-coded programmable resistor using a memristor [86]

T. Wey and W. Jemison used an automatic gain control (AGC) topology with a variable gain amplifier utilizing a (TiO₂) memristor [87]. Makot O. Itoh derived several memristor-based nonlinear oscillators from Chua's oscillators [88]. Vanessa Botta presented an stability analysis of one memristor oscillator with a mathematical model given by a four-dimensional five-parameter cubic system of ordinary differential equations [89]. M. Affan Zidan presented a memristor-based oscillator without using any capacitors or inductors [90]. The introduced reactance-less oscillator enables an area efficient implementation for low frequency oscillators. The circuit is shown in Fig.10.

The nonlinear dynamics of three memristor based phase shift oscillators are reported in[91] . It is considered that they will be a plausible solution for the realization of parametric oscillation as an autonomous linear time variant system. A.G. Mosad presented an improved memristor-based relaxation oscillator which offers higher frequency and wider tuning range than the existing reactance-less oscillators [92].

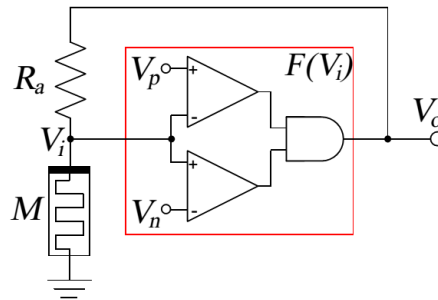


Fig.10 Memristor based reactance-less oscillator[90]

9. Conclusion

Recently, memristors have gained a wide research interest and found many applications. In this paper, an overview of memristor's basic operation, fabrication and modelling are presented. Also a survey on the various applications of memristors, which include non-volatile memories, neuromorphic computer architectures, logic circuits, and analogue applications is provided. This survey aims to give the reader a general overview of the device operation, main models, and recent research achievements in the field of memristor technology. Beside the overview, a future prospective is given for many possible improvements in memristors' modelling and applications, which can be useful for the upcoming researches and helps in finding new ideas in the memristor field.

References

- [1] L. Chua, "Memristor-the missing circuit element," *Circuit Theory, IEEE Transactions on*, vol. 18, pp. 507-519, 1971.
- [2] J. J. Yang. (5/2014). Available: <http://www.ieeeahn.org/wiki/index.php/Memristor>
- [3] D. B. Strukov, G. S. Snider, D. R. Stewart, and R. S. Williams, "The missing memristor found," *Nature*, vol. 453, pp. 80-83, 2008.
- [4] F. Corinto, P. P. Civalleri, and L. O. Chua, "A theoretical approach to memristor devices," 2015.
- [5] C. Mellor. (3/2014). Available: http://www.theregister.co.uk/Print/2011/12/27/memristors_and_mouuttet/

- [6] (2/2014). Available: <http://en.wikipedia.org/wiki/Memristor>
- [7] C. E. Merkel and D. Kudithipudi, "Towards thermal profiling in CMOS/memristor hybrid RRAM architectures," in *VLSI Design (VLSID), 2012 25th International Conference on*, 2012, pp. 167-172.
- [8] V. Mladenov and S. Kirilov, "Analysis of temperature influence on titanium-dioxide memristor characteristics at pulse mode," 2013.
- [9] E. Delonno, M. D. Looper, J. V. Osborn, H. J. Barnaby, and W. M. Tong, "Radiation effects studies on thin film TiO₂ memristor devices," in *Aerospace Conference, 2013 IEEE*, 2013, pp. 1-8.
- [10] V. Erokhin and M. P. Fontana, "Electrochemically controlled polymeric device: a memristor (and more) found two years ago," *arXiv preprint arXiv:0807.0333*, 2008.
- [11] M. P. Crupi, L.; Tozer, S, "Modelling Neural Plasticity with Memristors," *IEEE Canadian Review*, 2012.
- [12] A. Chanthbouala, V. Garcia, R. O. Cherifi, K. Bouzheouane, S. Fusil, X. Moya, *et al.*, "A ferroelectric memristor," *Nature materials*, vol. 11, pp. 860-864, 2012.
- [13] D. Kim, H. Lu, S. Ryu, C.-W. Bark, C.-B. Eom, E. Tsymbal, *et al.*, "Ferroelectric tunnel memristor," *Nano letters*, vol. 12, pp. 5697-5702, 2012.
- [14] K. H. Choi, M. Mustafa, K. Rahman, B. K. Jeong, and Y. H. Doh, "Cost-effective fabrication of memristive devices with ZnO thin film using printed electronics technologies," *Applied Physics A*, vol. 106, pp. 165-170, 2012.
- [15] N. R. McDonald, "Al/Cu_xO/Cu Memristive Devices: Fabrication, Characterization, and Modeling," DTIC Document 2012.
- [16] N. Gergel-Hackett, B. Hamadani, B. Dunlap, J. Suehle, C. Richter, C. Hacker, *et al.*, "A flexible solution-processed memristor," *Electron Device Letters, IEEE*, vol. 30, pp. 706-708, 2009.
- [17] K. Miller, "Fabrication and modeling of thin-film anodic titania memristors," Iowa State University, 2010.
- [18] J. R. Ordosgoitti, "Development of a Non-Volatile Memristor Device Based on a Manganese-Doped Titanium Oxide Material," The University of Toledo, 2010.
- [19] J. H. Nickel, J.-P. Strachan, M. D. Pickett, C. Tom Schamp, J. Joshua Yang, J. A. Graham, *et al.*, "Memristor structures for high scalability: Non-linear and symmetric devices utilizing fabrication friendly materials and processes," *Microelectronic Engineering*, 2012.
- [20] X. Wang, Y. Chen, H. Xi, H. Li, and D. Dimitrov, "Spintronic memristor through spin-torque-induced magnetization motion," *Electron Device Letters, IEEE*, vol. 30, pp. 294-297, 2009.

- [21] S. H. Jo, "Nanoscale memristive devices for memory and logic applications," The University of Michigan, 2010.
- [22] T. Chang, "Tungsten Oxide Memristive Devices for Neuromorphic Applications," The University of Michigan, 2012.
- [23] S. Benderli and T. Wey, "On SPICE macromodelling of TiO₂ memristors," *Electronics Letters*, vol. 45, pp. 377-379, 2009.
- [24] T. Prodromakis, B. P. Peh, C. Papavassiliou, and C. Toumazou, "A versatile memristor model with nonlinear dopant kinetics," *Electron Devices, IEEE Transactions on*, vol. 58, pp. 3099-3105, 2011.
- [25] Y. N. Joglekar and S. J. Wolf, "The elusive memristor: properties of basic electrical circuits," *European Journal of Physics*, vol. 30, p. 661, 2009.
- [26] Z. Biolek, D. Biolek, and V. Biolkova, "SPICE model of memristor with nonlinear dopant drift," *Radioengineering*, vol. 18, pp. 210-214, 2009.
- [27] S. Kvatinsky, E. G. Friedman, A. Kolodny, and U. C. Weiser, "Team: threshold adaptive memristor model," 2013.
- [28] J. Chowdhury, J. Das, and N. Rout, "Implementing trigonometric nonlinearity in linear ion-drift memristor model," in *Industrial Instrumentation and Control (ICIC), 2015 International Conference on*, 2015, pp. 1150-1153.
- [29] M. D. Pickett, D. B. Strukov, J. L. Borghetti, J. J. Yang, G. S. Snider, D. R. Stewart, *et al.*, "Switching dynamics in titanium dioxide memristive devices," *Journal of Applied Physics*, vol. 106, pp. 074508-074508-6, 2009.
- [30] O. Kavehei, A. Iqbal, Y. Kim, K. Eshraghian, S. Al-Sarawi, and D. Abbott, "The fourth element: characteristics, modelling and electromagnetic theory of the memristor," *Proceedings of the Royal Society A: Mathematical, Physical and Engineering Science*, vol. 466, pp. 2175-2202, 2010.
- [31] Á. Rák and G. Csereny, "Macromodeling of the memristor in SPICE," *Computer-aided design of integrated circuits and systems, IEEE Transactions on*, vol. 29, pp. 632-636, 2010.
- [32] A. Kumar, "Memristor: The 4th Circuit Element," *International Journal of Advanced Computer and Mathematical Sciences*, vol. 3, pp. 176-180, 2012.
- [33] M. U. Bandaru, "Modelling and the Study of the Memristor," University of Dayton, 2012.
- [34] R. Mutlu and E. Karakulak, "Emulator circuit of TiO₂ memristor with linear dopant drift made using analog multiplier," in *Electrical, Electronics and Computer Engineering (ELECO), 2010 National Conference on*, 2010, pp. 380-384.

- [35] H. Kim, M. P. Sah, C. Yang, S. Cho, and L. O. Chua, "Memristor emulator for memristor circuit applications," 2012.
- [36] S. Shin, J.-M. Choi, S. Cho, and K.-S. Min, "Small-area and compact CMOS emulator circuit for CMOS/nanoscale memristor co-design," *Nanoscale research letters*, vol. 8, pp. 1-7, 2013.
- [37] L. Teng, H. H. lu, X. Wang, and X. Wang, "Chaotic behavior in fractional-order memristor-based simplest chaotic circuit using fourth degree polynomial," *Nonlinear Dynamics*, pp. 1-11, 2014.
- [38] C. Yang, H. Choi, S. Park, M. P. Sah, H. Kim, and L. O. Chua, "A memristor emulator as a replacement of a real memristor," *Semiconductor Science and Technology*, vol. 30, p. 015007, 2015.
- [39] A. Radwan, M. A. Zidan, and K. Salama, "HP memristor mathematical model for periodic signals and DC," in *Circuits and Systems (MWSCAS), 2010 53rd IEEE International Midwest Symposium on*, 2010, pp. 861-864.
- [40] M. Pickett, "The Materials Science of Titanium Dioxide Memristors," 2010.
- [41] H. H. Li and M. Hu, "Compact model of memristors and its application in computing systems," in *Proceedings of the Conference on Design, Automation and Test in Europe*, 2010, pp. 673-678.
- [42] D. Batas and H. Fiedler, "A memristor SPICE implementation and a new approach for magnetic flux-controlled memristor modeling," *Nanotechnology, IEEE Transactions on*, vol. 10, pp. 250-255, 2011.
- [43] J. Greenlee, "Temporal and spatial modeling of analog memristors," 2011.
- [44] S. Kvatinsky, K. Talisveyberg, D. Fliter, E. G. Friedman, A. Kolodny, and U. C. Weiser, "Verilog-A for Memristor Models," CCIT Technical Report 2011.
- [45] F. Garcia-Redondo, M. Lopez-Vallejo, P. Ituero, and C. López Barrio, "A CAD framework for the characterization and use of memristor models," in *Synthesis, Modeling, Analysis and Simulation Methods and Applications to Circuit Design (SMACD), 2012 International Conference on*, 2012, pp. 25-28.
- [46] M. Condon, A. Deano, and A. Iserles, "Simulation of memristors in presence of high-frequency forcing function," *Electronics letters*, vol. 48, pp. 684-686, 2012.
- [47] M. Zangeneh and A. Joshi, "Performance and energy models for memristor-based 1T1R RRAM cell," in *Proceedings of the great lakes symposium on VLSI*, 2012, pp. 9-14.

- [48] J. Tenreiro Machado, "Fractional generalization of memristor and higher order elements," *Communications in Nonlinear Science and Numerical Simulation*, 2012.
- [49] S. Wen, Z. Zeng, and T. Huang, "Fuzzy modeling and synchronization of different memristor-based chaotic circuits," *Physics Letters A*, 2013.
- [50] R. S. Williams, M. D. Pickett, and J. P. Strachan, "Physics-based memristor models," in *Circuits and Systems (ISCAS), 2013 IEEE International Symposium on*, 2013, pp. 217-220.
- [51] Y. Liu, "Architecture for Memristor-based Storage Structures," Duke University, 2011.
- [52] C. Xu, X. Dong, N. P. Jouppi, and Y. Xie, "Design implications of memristor-based RRAM cross-point structures," in *Design, Automation & Test in Europe Conference & Exhibition (DATE), 2011*, 2011, pp. 1-6.
- [53] M. S. Qureshi, M. Pickett, F. Miao, and J. P. Strachan, "CMOS interface circuits for reading and writing memristor crossbar array," in *Circuits and systems (ISCAS), 2011 IEEE international symposium on*, 2011, pp. 2954-2957.
- [54] K. Eshraghian, K.-R. Cho, O. Kavehei, S.-K. Kang, D. Abbott, and S.-M. S. Kang, "Memristor MOS content addressable memory (MCAM): Hybrid architecture for future high performance search engines," *Very Large Scale Integration (VLSI) Systems, IEEE Transactions on*, vol. 19, pp. 1407-1417, 2011.
- [55] W. Chen, X. Yang, and F. Z. Wang, "Delayed Switching Applied to Memristor Content Addressable Memory Cell," in *Proceedings of the World Congress on Engineering*, 2013.
- [56] O. Kavehei, "Memristive Devices and Circuits for Computing, Memory, and Neuromorphic Applications," The University of Adelaide, Australia, 2011.
- [57] Y. Ho, G. M. Huang, and P. Li, "Dynamical properties and design analysis for nonvolatile memristor memories," *Circuits and Systems I: Regular Papers, IEEE Transactions on*, vol. 58, pp. 724-736, 2011.
- [58] M. A. Zidan, H. A. H. Fahmy, M. M. Hussain, and K. N. Salama, "Memristor-based memory: The sneak paths problem and solutions," *Microelectronics Journal*, 2012.
- [59] Y. Cassuto, S. Kvatinsky, and E. Yaakobi, "Sneak-Path Constraints in Memristor Crossbar Arrays," *IEEE International Symposium on Information Theory*, 2013.
- [60] T. PEREZ, "Evaluation Of System-Level Impacts Of A Persistent Main Memory Architecture," Pontifícia Universidade Católica do Rio Grande do Sul, 2012.
- [61] P. Krzysteczko, "Memristive tunnel junctions," 2010.

- [62] S. H. Jo, T. Chang, I. Ebong, B. B. Bhadviya, P. Mazumder, and W. Lu, "Nanoscale memristor device as synapse in neuromorphic systems," *Nano letters*, vol. 10, pp. 1297-1301, 2010.
- [63] N. R. McDonald, R. E. Pino, P. J. Rozwood, and B. T. Wysocki, "Analysis of dynamic linear and non-linear memristor device models for emerging neuromorphic computing hardware design," in *Neural Networks (IJCNN), The 2010 International Joint Conference on*, 2010, pp. 1-5.
- [64] D. Chabi, W. Zhao, D. Querlioz, and J.-O. Klein, "Robust neural logic block (NLB) based on memristor crossbar array," in *Nanoscale Architectures (NANOARCH), 2011 IEEE/ACM International Symposium on*, 2011, pp. 137-143.
- [65] A. Sinha, M. S. Kulkarni, and C. Teuscher, "Evolving nanoscale associative memories with memristors," in *Nanotechnology (IEEE-NANO), 2011 11th IEEE Conference on*, 2011, pp. 860-864.
- [66] M. Soltiz, "Hardware Neuromorphic Learning Systems Utilizing Memristive Devices," Rochester Institute of Technology, 2012.
- [67] S. Keemink, "Mimicking synaptic plasticity in memristive neuromorphic systems," *Life Sciences Graduate School, University of Utrecht, Utrecht, Netherlands*, 2012.
- [68] G. Zhang, Y. Shen, Q. Yin, and J. Sun, "Passivity analysis for memristor-based recurrent neural networks with discrete and distributed delays," *Neural Networks*, vol. 61, pp. 49-58, 2015.
- [69] I. E. Ebong and P. Mazumder, "CMOS and memristor-based neural network design for position detection," *Proceedings of the IEEE*, vol. 100, pp. 2050-2060, 2012.
- [70] I. E. Ebong, "Training Memristors for Reliable Computing," The University of Michigan, 2013.
- [71] A. Wu and Z. Zeng, "Dynamic behaviors of memristor-based recurrent neural networks with time-varying delays," *Neural Networks*, 2012.
- [72] S. Wen, Z. Zeng, and T. Huang, "Exponential stability analysis of memristor-based recurrent neural networks with time-varying delays," *Neurocomputing*, 2012.
- [73] Z. Guo, J. Wang, and Z. Yan, "Global exponential dissipativity and stabilization of memristor-based recurrent neural networks with time-varying delays," *Neural Networks*, vol. 48, pp. 158-172, 2013.
- [74] S. Wen, G. Bao, Z. Zeng, Y. Chen, and T. Huang, "Global exponential synchronization of memristor-based recurrent neural networks with time-varying delays," *Neural Networks*, vol. 48, pp. 195-203, 2013.
- [75] N. Li and J. Cao, "New synchronization criteria for memristor-based networks: Adaptive control and feedback control schemes," *Neural Networks*, vol. 61, pp. 1-9, 2015.

- [76] G. Zhang and Y. Shen, "Global exponential periodicity and stability of a class of memristor-based recurrent neural networks with multiple delays," *Information Sciences*, 2012.
- [77] G. Zhang, Y. Shen, and J. Sun, "Global exponential stability of a class of memristor-based recurrent neural networks with time-varying delays," *Neurocomputing*, vol. 97, pp. 149-154, 2012.
- [78] Z. Cai and L. Huang, "Functional differential inclusions and dynamic behaviors for memristor-based BAM neural networks with time-varying delays," *Communications in Nonlinear Science and Numerical Simulation*, vol. 19, pp. 1279-1300, 2014.
- [79] C. H. Bennett, D. Chabi, T. Cabaret, B. Joussetme, V. Derycke, D. Querlioz, *et al.*, "Supervised learning with organic memristor devices and prospects for neural crossbar arrays," in *Nanoscale Architectures (NANOARCH), 2015 IEEE/ACM International Symposium on*, 2015, pp. 181-186.
- [80] A. Rothenbuhler, "A Memristor-Based Neuromorphic Computing Application," Boise State University, 2013.
- [81] F. L. P. Lopes, "Processing with memristors," 2011.
- [82] T. Raja and S. Mourad, "Digital logic implementation in memristor-based crossbars," in *Communications, Circuits and Systems, 2009. ICCAS 2009. International Conference on*, 2009, pp. 939-943.
- [83] Q. Xia, W. Robinett, M. W. Cumbie, N. Banerjee, T. J. Cardinali, J. J. Yang, *et al.*, "Memristor- CMOS hybrid integrated circuits for reconfigurable logic," *Nano letters*, vol. 9, pp. 3640-3645, 2009.
- [84] J. Cong and B. Xiao, "mrFPGA: A novel FPGA architecture with memristor-based reconfiguration," in *Nanoscale Architectures (NANOARCH), 2011 IEEE/ACM International Symposium on*, 2011, pp. 1-8.
- [85] D. Strukov and A. Mishchenko, "Monolithically stackable hybrid FPGA," in *Design, Automation & Test in Europe Conference & Exhibition (DATE), 2010*, 2010, pp. 661-666.
- [86] S. Shin, K. Kim, and S.-M. Kang, "Memristor applications for programmable analog ICs," *Nanotechnology, IEEE Transactions on*, vol. 10, pp. 266-274, 2011.
- [87] T. Wey and W. Jemison, "An automatic gain control circuit with TiO₂ memristor variable gain amplifier," *Analog Integrated Circuits and Signal Processing*, vol. 73, pp. 663-672, 2012.
- [88] M. Itoh and L. O. Chua, "Memristor oscillators," *International Journal of Bifurcation and Chaos*, vol. 18, pp. 3183-3206, 2008.
- [89] V. Botta, "STABILITY ANALYSIS OF THE FOURTH-ORDER CUBIC MEMRISTOR OSCILLATOR."

- [90] M. A. Zidan, H. Omran, A. Radwan, and K. Salama, "Memristor-based reactance-less oscillator," *Electronics letters*, vol. 47, pp. 1220-1221, 2011.
- [91] A. Talukdar, A. G. Radwan, and K. N. Salama, "Non linear dynamics of memristor based 3rd order oscillatory system," *Microelectronics Journal*, vol. 43, pp. 169-175, 2012.
- [92] A. Mosad, M. Fouda, M. Khatib, K. Salama, and A. Radwan, "Improved memristor-based relaxation oscillator," *Microelectronics Journal*, 2013.

الممرستور نظرة عامة وحتى 2015م

شريف نافع – أحمد شعبان دسوقي – السيد محمود الربيعي

وحتى عام 1971م كان هناك ثلاثة عناصر كهربائية أساسية والمعروفة بالمقاوم، الملف، والمكثف. وفي عام 1971م اقترح البروفيسور ليون تشوا نظريا عنصر كهربائي رابع، أطلق عليه مسمى "الممرستور". وهو عنصر ذو طرفين تعتمد مقاومته على قيمة واتجاه وفترة الجهد المطبق وقد تم تصنيع هذا العنصر في وقت لاحق في مختبرات HP في عام 2008م، والتي فتحت مساحة واسعة من البحوث على ممرستور وتطبيقاتها الممكنة التناظرية والرقمية منها. ويلقي هذا البحث لمحة عامة عن خصائص الممرستور، تطبيقاته، آليات نمذجته وبعض التحسينات الممكنة في المستقبل.

An Electrical Model for Atom's Emission and Future Electronics

Ali A. Elabd, El-Sayed M. El-Rabaie, Abdel-Aziz T. Shalaby

Faculty of Engineering, Menoufia University, Menouf, EGYPT

(Received: 03-September-2015 – Accepted: 03-October-2015)

Abstract

In this paper, an electrical model – equivalent circuit – for atom's emission is presented and Hydrogen atom is taken as an example. Also, the line spectra of Iron and Sodium are used to verify the model. This may open a new area of research to build practical digital circuits such as INVERTER, NAND, NOR ...etc from some cascaded atoms.

1. Introduction

The development of electronics, to increase the processors speed and memories capacity, needs to minimize the transistors size. We dream to minimize the circuit size to the scale of the atom so the circuit elements can have ideal values in order to implement ultralow power devices.

The analogy between transportation of an electron in single electron circuits and inside a hydrogen atom is a chance to convert the atom to a capacitance system. Fig. 1 compares the energy and frequency of the emitted photons from tunnel junction and an atom.

The physics of single electronics is based on the coulomb blockade concept. This means, to transfer one electron throw a tunnel junction with a capacitance C , the electron must overcome the charging energy barrier E_c [1], Coulomb blockade energy, where:

$$E_c = \frac{e^2}{2C} \quad (1)$$

The electromagnetic radiation with frequency $f \sim E_c/h$ is generated as a photo-response of single-electron systems [2].

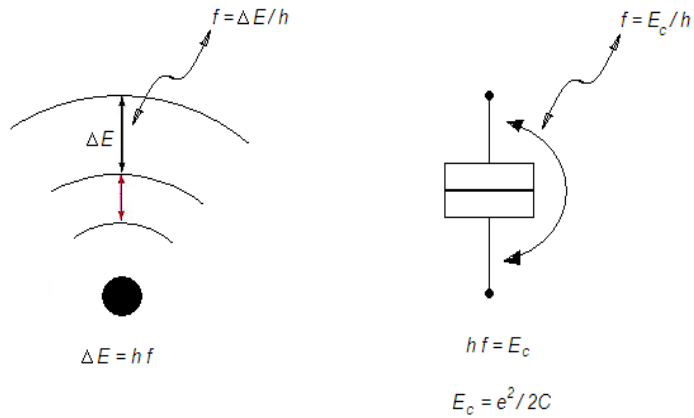


Fig. 1: Energy and frequency of the emitted photons from tunnel junction and an atom

2. MODELLING OF HYDROGEN ATOM

Hydrogen atom can be considered as a system of concentric conducting spheres, where the spheres represent maximum probability surfaces of finding the electron. The capacitance between two concentric spheres is:

$$C = 4\pi\epsilon_0 \left(\frac{1}{a} - \frac{1}{b} \right)^{-1} \quad (2)$$

Where, ϵ_0 is the permittivity of the vacuum and a, b are the radiuses of the inner and outer spheres respectively. Substitute equation (2) in (1) and solve for $1/\lambda$:

$$\frac{1}{\lambda} = \frac{e^2}{8\pi\epsilon_0 hc} \left(\frac{1}{a} - \frac{1}{b} \right) \quad (3)$$

Equation (3) is the same as Bohr's formula for Hydrogen emission before applying the quantization of angular momentum. The appearance of this formula as a result of the capacitance model is a nice consequence. In Fig. 2, ΔE – the energy difference between energy levels – is replaced by its equivalent E_c . The capacitance system of concentric spheres looks like capacitors connected in series. So, Hydrogen atom can be modelled by series of tunnel junctions as in Fig. 3.

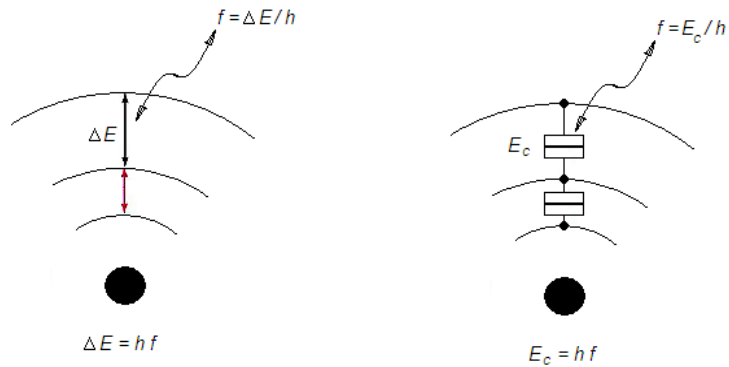


Fig. 2 ΔE is replaced by its equivalent E_c .

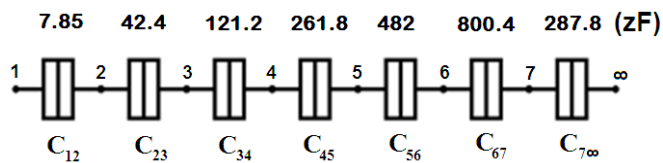


Fig. 3 Electrical model for Hydrogen emission.

The photo-response of the circuit shown in Fig. (3) is the same as the line spectrum of Hydrogen atom. When an electron tunnels through C_{12} , the generated photon has the frequency of the first term of Lyman series. And when it tunnels through C_{12} and C_{23} the generated photon has the frequency of the second term of Lyman series. Also the third term of Lyman series is generated when an electron tunnels through the C_{12} , C_{23} and C_{34} and so on. The first terms of Balmer and Paschen series are generated when an electron tunnels through C_{23} and C_{34} respectively. And the complete spectrum of Hydrogen is generated by the same manner.

The circuit emission of the first order tunneling events is simulated by MUSES [3, 4] and illustrated in Fig. (4). The tunneling resistance and the temperature are taken to be $1 \text{ M } \Omega$ and $6000 \text{ }^\circ\text{K}$ respectively. The first node connected to 10 mV voltage source and the infinity node connected to the ground. The energy of the generated electromagnetic radiation has a good agreement with the relative intensity of the Hydrogen line spectrum emission [5].

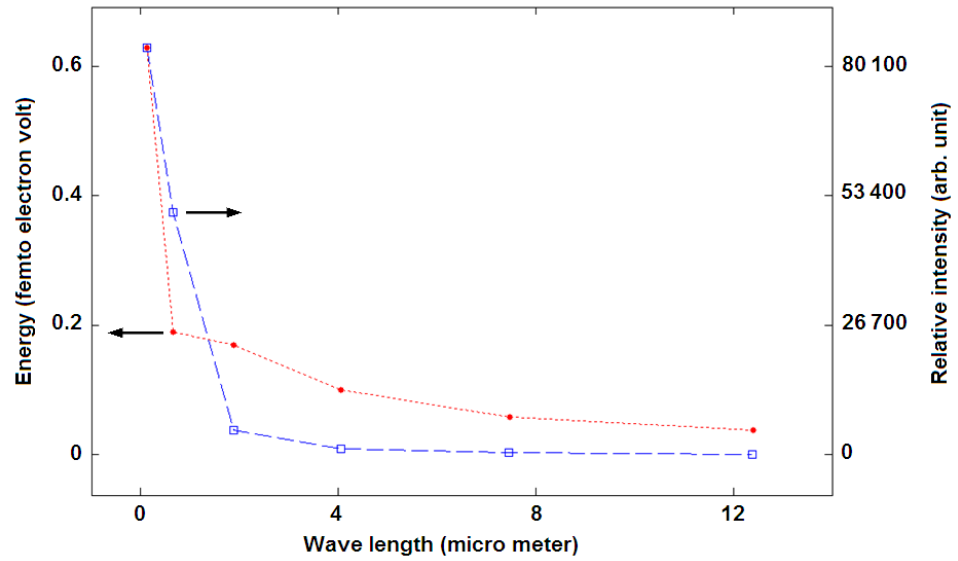


Fig. 4 Comparison between the relative intensity of the Hydrogen line spectrum emission – measured data – (Squares) [5], and the photo-response energy of the Hydrogen emission equivalent circuit simulated by MUSES (Dots).

3. PARTIAL MODELING OF HEAVY ATOMS

The relation between capacitors in Fig. (3) is:

$$\frac{1}{C_{ij}} = \frac{1}{C_{i,i+1}} + \frac{1}{C_{i+1,i+2}} + \dots + \frac{1}{C_{j-2,j-1}} + \frac{1}{C_{j-1,j}} \quad (4)$$

Also the wave lengths of the generated photons have the same relation because $\lambda \propto C$, then:

$$\frac{1}{\lambda_{ij}} = \frac{1}{\lambda_{i,i+1}} + \frac{1}{\lambda_{i+1,i+2}} + \dots + \frac{1}{\lambda_{j-2,j-1}} + \frac{1}{\lambda_{j-1,j}} \quad (5)$$

Fig. 5 illustrates the relation between the wavelengths of the hydrogen line spectrum that can be deduced directly from the role of summing capacitors in series.

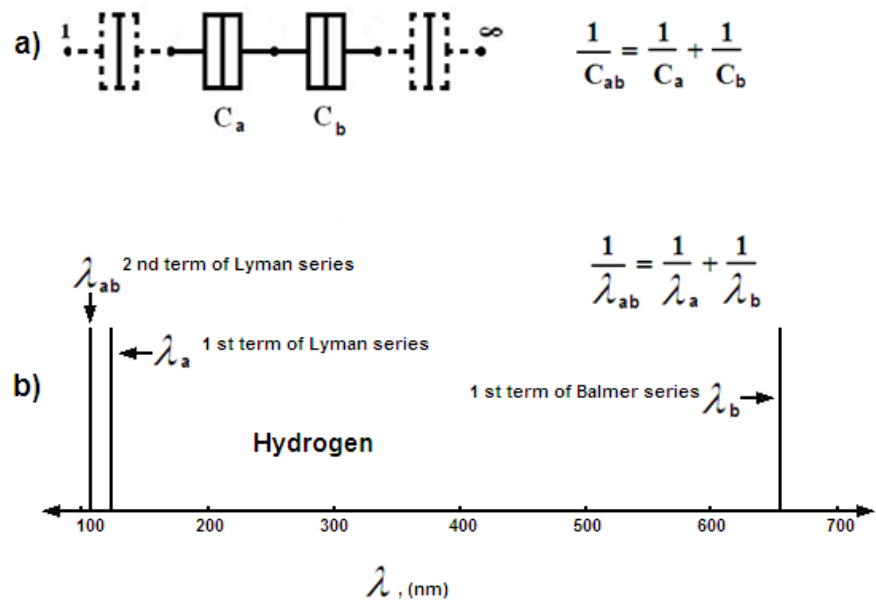


Fig. 5 The role of summing capacitors in series is also applied to the wave lengths of the line spectrum a) The role of summing capacitors in series, b) Example from the Hydrogen line spectrum.

Equation (5) may be used to validate the model for atoms which have more than one electron.

The line spectra of Sodium and Iron are shown in Fig. 6 and the arrows pointed to the wave lengths that verify equation (5).

For Sodium:
$$\frac{1}{\lambda_{S1}} = \frac{1}{\lambda_{S2}} + \frac{1}{\lambda_{S3}}$$

And for Iron:
$$\frac{1}{\lambda_{I1}} = \frac{1}{\lambda_{I2}} + \frac{1}{\lambda_{I3}}$$

Fig. 7 represents parts of the equivalent circuit of Sodium and Iron atoms.

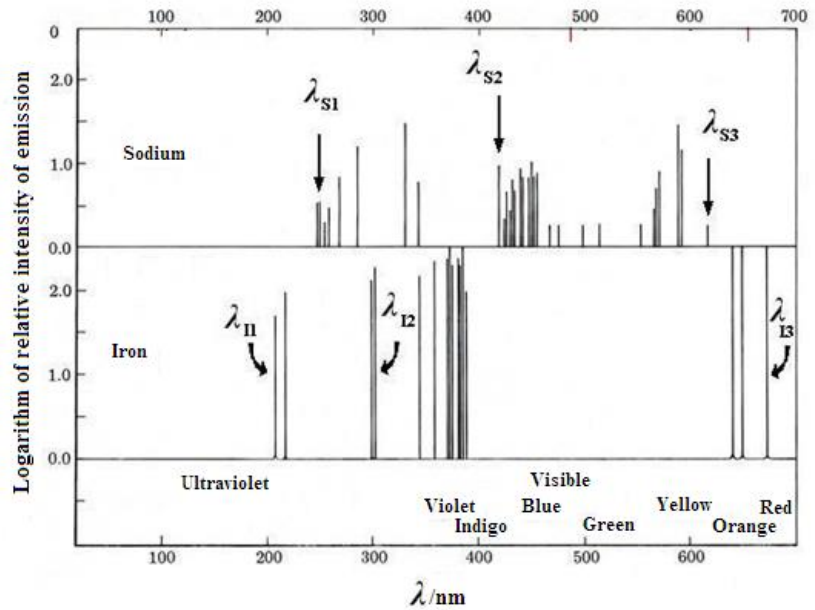


Fig. 6: Applying equation (5) on the spectra of Sodium and Iron(The spectrum without the arrows is from reference [6]).

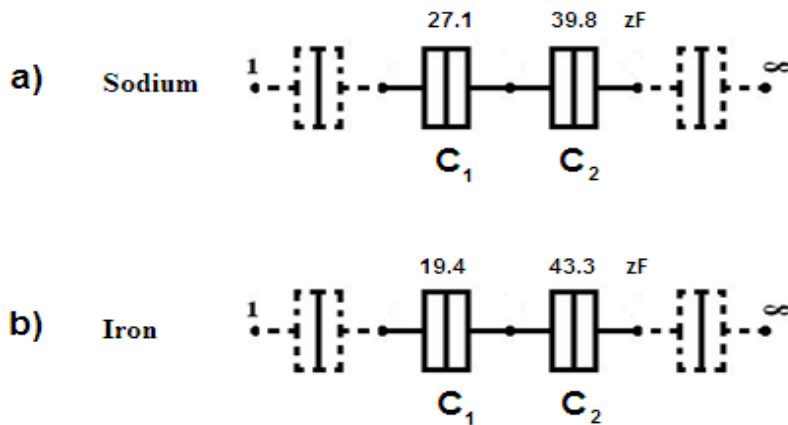


Fig. 7: Partial electrical models for a) Sodium and b) Iron atoms

4. CONCLUSION

From the electrical model of Hydrogen atom emission and the partial models of Sodium and Iron, the atom may work as an electric circuit. The

question now, if we can express an atom by an electric circuit, can we express a circuit by some atoms to implement basic digital circuits.

References

- [1] D. Berman, "The Aluminum Single Electron Transistor for Ultra Sensitive Electrometry of Semiconductor Quantum-Confined Systems", PhD Dissertation, Massachusetts Institute of Technology, 1998.
- [2] K. K. Likharev and I. A. Devyatov, "Photoresponse and Photosensitivity of Single-Electron Tunneling Systems", *Physica B*, vol. 194-196 (February 1994), pp. 1341-1342.
- [3] A. A. Elabd, A. T. Shalaby and E. M. El-Rabaie, "Monte Carlo Simulation of Single Electronics Based on Orthodox Theory", *International Journal of Nano Devices, Sensors and Systems (IJ-Nano)*, vol. 1, No. 2, pp. 65-76.
- [4] A. A. Elabd, E. M. Elrabaie and A. T. Shalaby, "Analysis of Rare Events Effect on Single Electronics Simulation Based on Orthodox Theory", *Journal of Computational Electronics*: vol. 14, Issue 2 (2015), pp. 604-610.
- [5] A. Kramida, Yu. Ralchenko, J. Reader and NIST ASD Team (2014). NIST Atomic Spectra Database (ver. 5.2), [Online]. Available: <http://physics.nist.gov/asd> [2015, May 21]. National Institute of Standards and Technology, Gaithersburg, MD.
- [6] J. W. Moore, W. G. Davies and R. W. Collins, "Chemistry", McGraw-Hill, 1978.

بيان بأسماء السادة المحكمين للبحوث المنشورة بعدد يناير-يوليو 2015

من [مجلة المنوفية لبحوث الهندسة الإلكترونية النصف سنوية]

حسب الترتيب الأبجدي

م	أسم المحكم	جهة العمل
1	أ.د/ أنور عبد الرحمن حجازي	كلية العلوم- شبين الكوم- جامعة المنوفية
2	أ.د / السيد محمود الربيعي	كلية الهندسة الإلكترونية بمنوف
3	د / أيمن السيد أحمد	كلية الهندسة الإلكترونية بمنوف
4	أ.د / سامي عبد المنعم الضليل	كلية الهندسة الإلكترونية بمنوف
5	أ.د / طه السيد طه	كلية الهندسة الإلكترونية بمنوف
6	أ.د/ عبدالهادي عمار	كلية الهندسة- جامعة الأزهر
7	أ.د /عبد الحلیم عبدالنبی ذکری	كلية الهندسة- جامعة عين شمس
8	أ.د / عاطف السيد أبو العزم	كلية الهندسة الإلكترونية بمنوف
9	أ.د/ فايز ونيس ذكي	كلية الهندسة- جامعة المنصورة
10	أ.د / محمد مبروك شرف	كلية الهندسة الإلكترونية بمنوف
11	أ.د / مظهر بسيوني طایل	كلية الهندسة - جامعة المنيا
12	أ.د / محمد أبو زهاد	كلية الهندسة - جامعة أسيوط
13	أ.د / محمد إبراهيم العدوى	كلية الهندسة - جامعة حلوان
14	أ.د /محمد فهيم الكردي	كلية الهندسة الإلكترونية بمنوف
15	أ.د / معوض إبراهيم معوض	كلية الهندسة الإلكترونية بمنوف
16	أ.د / ناجي وديع مسيحه	كلية الهندسة الإلكترونية بمنوف
17	أ.د / هشام فتحي على	كلية الهندسة - جامعة المنيا

مجلة المنوفية لبحوث الهندسة الإلكترونية

① يرسل الباحث بحثه باسم الأستاذ الدكتور / عميد الكلية ورئيس لجنة النشر العلمي من ثلاث نسخ .

② الصفحة الأولى تحتوي على :-

- أ. عنوان البحث .
- ب. المؤلفين ووظائفهم وأماكن عملهم .
- ج. الكلمات الرئيسية **keywords** بما لا يزيد على خمسة .
- د. ملخص البحث لا يزيد على ((300)) كلمة بدون معادلات أو أرقام مراجع .
- هـ. في أسفل الصفحة يكتب العنوان الكامل للمؤلفين وكذلك العنوان الإلكتروني أو الفاكس والتليفون إن وجد .
- و. يقدم البحث أثناء التحكيم بخط كبير ومناسب ويترك مسافة بين السطور .
- ي. يقدم البحث طبقاً للنماذج المعلنة (إرشادات للمؤلف) على موقع المجلة على شبكة الانترنت .

③ يكتب البحث على عمود واحد بنفس أسلوب كتاب دوريات عائلة المجلات الدولية (INT.J) ونفس نماذج الحروف المتبعة ويكون الحجم النهائي لكل إصدار هو (21سم * 28سم) .

④ تكتب بعد الملخص مقدمة البحث (INTRODUCTION) التي تحتوي على الهدف من البحث وكذلك إسهامات الباحثين الآخرين التي تم البناء عليه وكذا الإسهام الحقيقي للبحث .

⑤ في الخلاصة (CONCLUSION) يجب ذكر المميزات إن وجدت وكذلك القيود والتطبيقات .

⑥ المراجع تكتب في قسم منفصل في نهاية البحث بالأسلوب المتبع في (IEEE) ويشار في البحث بأرقامها داخل أقواس مثلاً [1] .

⑦ الأشكال والصور يجب أن تكون عند حد الضرورة ويجب أن تكون أصلية وليست منسوخة وأن تكون واضحة ومعبرة وتكون دائماً بالأبيض والأسود والكتابة على الرسم يجب أن تكون ذات حجم يناسب حجم الرسم .

⑧ يتم ترقيم الصفحات أسفلها بالقلم الرصاص .

⑨ يصاحب البحث قرص مدمج مكتوب على (WORD) .

مجلة المنوفية للبحوث الهندسية الإلكترونية

- ① بالنسبة لأعضاء هيئة التدريس والهيئة المعاونة بالكلية يكون رسم الاشتراك بالكلية (25 جنيهاً) سنوياً ويتم السداد شخصياً لمن يرغب في أن تصله نسخة من كل إصدار ويدفع رسوم نشر عن كل بحث عدد صفحاته (ثمانية صفحات) فأقل مبلغ (225 جنيهاً) ولكل صفحة زائدة عن ذلك رسم قدره (10 جنيهاً).
- ② يتم النشر للزملاء أعضاء هيئة التدريس من داخل الجامعة نظير رسم قدرة (275 جنيهاً) للبحث الذي لا يتعدى (ثمانية صفحات) ولكل صفحة زائدة عن ذلك رسم قدره (15 جنيهاً).
- ③ للباحثين من خارج جامعة المنوفية تنشر بحوثهم نظير رسم قدرة (300 جنيهاً) للبحث الذي لا يتعدى (ثمانية صفحات) ولكل صفحة زائدة عن ذلك رسم قدره (20 جنيهاً).
- ④ للباحثين من خارج جمهورية مصر العربية تنشر بحوثهم نظير رسم قدرة (100 دولار أو ما يعادلها) للبحث الذي لا يتعدى (ثمانية صفحات) ولكل صفحة زائدة عن ذلك رسم قدره (5 دولار أو ما يعادلها)..
- ⑤ رسم الاشتراك السنوي للأفراد داخل البلاد (50 جنيهاً) سنوياً.
- ⑥ رسم الاشتراك السنوي للهيئات داخل البلاد (300 جنيهاً) سنوياً.
- ⑦ رسم الاشتراك للأفراد خارج البلاد (50 دولار) سنوياً أو ما يعادلها.
- ⑧ رسم الاشتراك للهيئات خارج البلاد (300 دولار) سنوياً أو ما يعادلها.

وذلك عن العددين سنوياً ويعامل العدد الواحد بواقع النصف من القيمة

INFORMATION FOR AUTHORS

The Minufiya Journal of Electronic Engineering Research (MJEER) publishes only research papers. The journal does not publish essay or technical reporting types of paper. Prospective authors are encouraged to examine the journal itself for details of layout. Detailed instructions, which should be fully adhered at time of publication, are available upon request from the editor office. However submitted papers shall not be sent to referees before full adherence to the following requirements:

1. The submitted paper should not have been submitted earlier or at the same time to any other journal in Egypt or abroad.
2. Papers should be submitted in English in both of the following two form:
 - an original and three copies in A4 size
 - stored on a (CD) using WINWORD, Times New Roman, size 13
3. The margins in all pages except the first page are 3.5 cm from the top and the bottom, and 2.5 cm from the left and right. The first page should have margins 5 cm from the top. Text should be justified to the left and the right margins.
4. Only the abstract, the acknowledgments, the list of references, and the list of symbols are to be single line spaced. Other sections are to be 1.5 line spaced.
5. Paper title is to be typed centered in bold capital letters. Author(s) Name(s) should be typed in plain capital letters, centered, and placed 3 single spaces under the paper title. Footnote, size 10, giving the author(s) title(s) and affiliation(s) should be provided.
6. English abstract, maximum 200 words, should be provided immediately before the "Introduction" with the word ABSTRACT as heading flush left.
7. Figures and tables are to be totally integrated within the text. Captions should be located under the figure and on top of the table and clearly spaced within the main text. Lettering should be large enough to be readable after 80% reduction.
8. Reference should be cited in the text between square brackets and listed at the end of the paper with the word REFERENCES as heading flush left.
9. Headings are to be bold, flush left, with Arabic numerals. Major headings are all capital, subheading are initial capital, and only the first letter of each third level headings is capital.
10. Arabic summary within 10 lines is to be provided at the end of the paper preceded by Arabic translation of the paper title and abstract . For non-Arabic speaking authors a free of charge translation of the paper title and abstract can be provided by the editors.
11. For prospective authors a nonrefundable down payment of:
 - a) 225.0 LE for the regular paper of 8 pages and 10.0 LE for each extra page if they are faculty staff members,
 - b) 275.0 LE for the regular paper of 8 pages and 15.0 LE for each extra page if they are staff members in the university of Minufiya
 - c) 300.0 LE for the regular paper of 8 pages, and 20.0 LE for each extra page if they are members of other institution.
 - d) 100.0 USD for the regular paper of 8 pages, and 5.0 USD for each extra page if they are members of foreign institutions.

This amount is to be paid upon submission of the paper. In case of acceptance, the remaining fees should be settled with the treasurer before enrollment of the paper in the next possible issue. Publication fees cover cost of one copy of the journal, and 5 reprint.

Annual subscriptions : personal, 50.0 LE in Egypt and 50.0 USD abroad, institutional : 300.0 LE in Egypt and 300.0 USD abroad.

N.B. the ideas expressed in the papers are strictly those of the authors. The editors do not hold themselves responsible for the views expressed by the author.

Prof. Dr. El-Sayed M. El - Rabaie

مجلة المنوفية لبحوث الهندسة الإلكترونية

عنوان المراسلة:

جمهورية مصر العربية

محافظة المنوفية

منوف – رمز بريدي 32952

كلية الهندسة الإلكترونية

تليفون: 048 -3661334

فاكس: 048 -3660716

البريد الإلكتروني: Srabie1@yahoo.com

الحساب المصرفي:

البنك المركزي المصري – حساب الخزانة الموحدة – جامعة

المنوفية – كلية الهندسة الإلكترونية بمنوف – المجلة العلمية

للكلية – حساب رقم [9/450/80836/1]
